12-16-2013

# Fundamental Experimental Studies In Scaling, Blast Mitigation and Material Processing

Xing Zhao
*University of South Carolina - Columbia*

# Fundamental Experimental Studies in Scaling, Blast Mitigation and Material Processing

by

Xing Zhao

Bachelor of Science
Beijing University of Aeronautics and Astronautics, 2005

Master of Science
Beijing University of Aeronautics and Astronautics, 2008

---

Submitted in Partial Fulfillment of the Requirements

For the Degree of Doctor of Philosophy in

Mechanical Engineering

College of Engineering and Computing

University of South Carolina

2013

Accepted by:

Michael A. Sutton, Major Professor

Xiaomin Deng, Committee Member

Anthony Reynolds, Committee Member

Paul Ziehl, Committee Member

Fabio Matta, Committee Member

Lacy Ford, Vice Provost and Dean of Graduate Studies

# DEDICATION

*To my Family*

## ACKNOWLEDGEMENTS

I would like to take this opportunity to thank those individuals who have helped me and made this dissertation possible. First of all, I would like to express my appreciation to my advisor Dr. Michael Sutton for his guidance and support. I am lucky to work with such an outstanding and knowledgeable advisor.

I would like to thank Dr. Xiaomin Deng, Dr. Stephen McNeill and Dr. Anthony Reynolds for their valuable suggestions regarding the sand blast experiment and lab model of friction extrusion. I would like to show my appreciations to Dr. Yuh Chao, Dr. Fabio Matta and Dr. Paul Ziehl for serving as committee members during my PhD study. I would like to thank Vikrant Tiwari and Gary Shultis for sharing their experience in blast loading experiment. I also acknowledge Dr. William Fourney and Dr. Ulrich Leiste at University of Maryland for their help in the Dynamic Effects Laboratory.

I would like to thank all my friends for the good time during the past years.

I would express gratitude to my parents. Wherever I am, my heart is with them. I owe a lot to Xin Chen for her love and suggestion. All these together inspire me to complete this dissertation.

## ABSTRACT

In this work, two separate research efforts are discussed. They include experimental studies in (1) Scaling and Blast Mitigation and (2) Scaling in Friction Stir Extrusion. In both studies, the primary experimental measurement method is three-dimensional digital image correlation (3D-DIC), a non-contacting full-field measurement method that is applicable for both high-rate loading and quasi-static loading conditions.

**Scaling and Blast Mitigation Studies**

A series of properly scaled structures was subjected to buried blast loading conditions via detonation of a small explosive buried in saturated sand. Using high speed stereo-vision systems to record the deformations of selected regions on the upper surface of the structure, results clearly show that appropriate scaling of small specimens is adequate to compare responses from different size structures subjected to scaled levels of explosive loading, provided that the dominant physical processes remain similar in all cases.

Upon completion of the basic scaling studies, small scale models representing key vehicle structural elements, including (a) floorboards and bottom-mounted, downward V-shaped hulls in various configurations; (b) steel frames and steel structures with various frame connections and coatings, were subjected to buried blast loading. The results were used to compare various geometrical designs, with the primary metrics for the comparisons being vertical acceleration and the Head Injury Criterion. Results from these studies show that personnel on typical floorboard structures during blast loading will

incur unacceptable shock loading conditions, resulting in either serious or fatal injury. However, results also show that an appropriate design using frame-mounted passenger seating could reduce the potential for injury to an acceptable level.

**Scaling and Friction Stir Extrusion Studies**

With the goal of tracking particles in a highly viscous, transparent fluid under conditions that approximate a similar Reynold's Number as expected in friction stir processing of a metallic material, a complete experimental apparatus was developed. Since 3D-DIC is used to track the particles within the viscous fluid during the flow and extrusion processes, software was written to account for the effects of refraction at the air-glass and glass-fluid interfaces so that the recorded image positions could be accurately converted to 3D locations within the fluid. Next, a series of baseline (known marker positions on rigid targets within the fluid) and extrusion experiments were performed. Results obtained from baseline experiments where the true positions of markers are known confirm that the method is quite accurate. Finally, through sparse seeding of the fluid with neutrally buoyant spherical particles, a series of rotational flow and extrusion experiments were performed. Rotational flow experimental results were in excellent agreement with simulations, while the extrusion data is in good agreement with simulations in the latter part of the extrusion process.

# TABLE OF CONTENTS

# LIST OF TABLES

# LIST OF FIGURES

# LIST OF SYMBOLS

| | |
|---|---|
| $\mathbf{x}$ | Plate coordinate position vector |
| h | Plate thickness |
| $L_p$ | Plate in-plane dimension |
| $\sigma_0$ | Plate initial yield stress |
| $E_p$ | Plate Young's modulus |
| $\rho_p$ | Mass density of plate |
| $U$ | Explosion energy |
| d | Depth of buried explosive from sand surface |
| D | Stand-off distance from plate to sand surface |
| $\rho_s$ | Sand mass density |
| $L_f$ | Frame dimensions |
| $E_f$ | Frame Young's modulus |
| $\rho_f$ | Frame mass density |
| t | Time |
| $\mathbf{U}$ | Plate displacement vector |
| $\dot{\mathbf{U}}$ | Plate velocity vector |
| $\ddot{\mathbf{U}}$ | Plate acceleration vector |
| $\Delta$ | Permanent axial deflection of plate |
| $\boldsymbol{\varepsilon}$ | Strain |

$\dot{\varepsilon}$ Strain rate

H Height

P Impulse

E Potential energy

$(X_{w/cam1}, Y_{w/cam1}, Z_{w/cam1})$ World coordinate system / Camera 1 coordinate system

$(X_{cam2}, Y_{cam2}, Z_{cam2})$ Camera 2 coordinate system

$O_1$ / $O_2$ Focal points for cameras 1 and camera 2, respectively

f Perpendicular distance from pinhole to sensor plane

$(X_{s1}, Y_{s1})$ Sensor coordinate system of camera 1

$(X_{s2}, Y_{s2})$ Sensor coordinate system of camera 2

$I_{m1}$ / $I_{m2}$ Point on sensor plane of camera 1 / camera 2

$B_{s1}$ / $B_{s2}$ Intersection point on the air-glass interface

$B_{x1}$ / $B_{x2}$ Intersection point on the glass-fluid interface

Q General point of object in fluid

$Q^{'}$ Virtual point obtained without refraction effects

$(X_g, Y_g, Z_g)$ Grid coordinate system

$O_1'$ / $O_1''$ Projections of point $O_1$ onto both glass interfaces

$I_{m1}'$ / $I_{m1}''$ Projections of point $I_{m1}$ onto both interfaces

$O_2'$ / $O_2''$ Projections of point $O_2$ onto both glass interfaces

$I_{m2}'$ / $I_{m2}''$ Projections of point $I_{m2}$ onto both in interfaces

$\beta_1$ / $\beta_2$, $\delta_1$ / $\delta_2$, $\alpha_1$ / $\alpha_2$ Refraction angles

$(x_s^{o\text{-}G}, y_s^{o\text{-}G})$ Coordinates of imaged grid points on sensor plane

$(x_s^{mo\text{-}G}, y_s^{mo\text{-}G})$ Coordinates of grid points projected back by the model on the sensor

| | |
|---|---|
| $(x_s^o, y_s^o)$ | Coordinates of image points on sensor plane |
| $(x_s^{mo}, y_s^{mo})$ | Coordinates of image points optimized by model for reconstruction |
| a, b, d | Unit vector for planar interface of air and glass |
| $S_x^{cam1/2}$ | Horizontal scale factor of camera 1 and camera 2 (pixels/mm) |
| $S_y^{cam1/2}$ | Vertical scale factor of camera 1 and camera 2 ( pixels/mm) |
| $f_x^{cam1/2}$ | $f_x=f\,S_x^{cam1/2}$ of camera 1 and camera 2, f is lens focal length |
| $f_y^{cam1/2}$ | $f_y=f\,S_y^{cam1/2}$ of camera 1 and camera 2, f is lens focal length |
| $Skew^{cam1/2}$ | Skew factors for camera 1 and camera 2 |
| $k^{cam1/2}$ | Lens distortion factors for camera 1 and camera 2 |
| $\theta_x, \theta_y, \theta_z$ | Transformation (rotation) of camera 2 relative to camera 1 |
| $T_x, T_y, T_z$ | Transformation (translation) of camera 2 relative to camera 1 |
| $D_x^1, D_y^1, D_z^1$ | Translation of grid relative to world coordinate system for 1st image |
| $D_x^i, D_y^i, D_z^i$ | Translation of grid relative to world coordinate system for $i^{th}$ image |
| $\gamma_x^1, \gamma_x^1, \gamma_x^1$ | Rotation angles of grid relative to world coordinate system for 1st image |
| $\gamma_x^i, \gamma_x^i, \gamma_x^i$ | Rotation angles of grid relative to world coordinate system for $i^{th}$ image |

# List of Abbreviations

IED ..... Improvised Explosive Device

EFP ..... Explosively Formed Penetrator

DoD ..... Department of Defense

HIC ..... Head Injury Criterion

WSTC ..... Wayne State University Cerebral Concussion Tolerance

NHTSA ..... National Highway Traffic Safety Administration

PETN ..... Pentaerythritol Tetranitrate

DIC ..... Digital Image Correlation

2D-DIC ..... Two Dimensional Digital Image Correlation

3D-DIC ..... Three Dimensional Digital Image Correlation

DoB ..... Depth of Burial

MDoB ..... Middle Depth of Burial

DDoB ..... Deep Depth of Burial

SoD ..... Stand-off Distance

SSoD ..... Shallow Stand-off Distance

FT ..... Floorboard Thickness

TFT ..... Thick Floorboard Thickness

NH ..... No Hull

SH ..... Single Hull

FSH ..... Foam and Single Hull

DH ..... Double Hull

CH ..... Cantilever Hull

CCH ..... Cantilever Single Corrugated Hull

CH′ ..... Corrugated Hull

FSW ..... Friction Stir Welding

PIV ..... Particle Image Velocimetry

PTV ..... Particle Tracking Velocimetry

LSPIV ..... Large Scale Particle Image Velocimetry

LSPTV ..... Large Scale Particle Tracking Velocimetry

A/G ..... Air/Glass

G/F ..... Glass/Fluid

LED ..... Light-emitting Diode

# CHAPTER 1

# INTRODUCTION

## 1.1 OVERVIEW

In this work, two separate research efforts are discussed. They include experimental studies in (1) Scaling and Blast Mitigation and (2) Scaling in Friction Stir Extrusion. In both studies, the primary experimental measurement method is three-dimensional digital image correlation, a non-contacting full-field measurement method that uses either a high speed or a quasi-static stereo-vision imaging system to acquire images during the event. The Scaling and Blast Mitigation Studies present experimental results from a series of scaled structures that were subjected to buried blast loading conditions via detonation of a small explosive buried in saturated sand. It shows that appropriate scaling of small specimens is adequate to compare responses from different size structures subjected to scaled levels of explosive loading, provided that the dominant physical processes remain similar in all cases. The particle tracking study presents experimental results that clearly show that the effects of refraction at the air-glass and glass-fluid interfaces can be modeled and used to obtain accurate 3D positions of particles moving within a fluid. A complete experimental apparatus is developed with the goal of tracking particles in a highly viscous, transparent fluid under conditions that approximate a similar Reynold's Number as expected in friction stir processing of a metallic material. Finally, through sparse seeding of the fluid with neutrally buoyant spherical particles, a series of (a) rotational flow and (b) extrusion experiments were performed which were shown to be in

excellent and good agreement, respectively, with simulation predictions. Section 1.2 provides background in the digital image correlation method. Sections 1.3 and 1.4 report on the scaling and blast mitigation studies. Section 1.5 reports on the particle tracking study.

## 1.2 DIGITAL IMAGE CORRELATION METHOD

Digital image correlation is a computer-vision-based, non-contacting method to measure the surface deformation of a specimen subjected to general loading conditions. Using a single camera for imaging objects that deform in a given plane, 2D-DIC was first developed from the work of W.H. Peters and W.F. Ranson (Peters 1981) and required that the specimen be nominally flat, with minimal out-of-plane motion. These ideas were further developed and shown to be experimentally effective by Chu (Chu, 1985), Sutton (Sutton 1989) and Bruck & McNeill (Bruck , McNeil 1989). 2D-DIC using a single camera has proven to be an effective method of non-contact determination of displacement and strain measurements in a wide range of physics and engineering studies. The 2D-DIC method was extended to the measurement of the complete three-dimensional surface deformation on a non-planar specimen by employing stereovision concepts and multiple cameras (Luo 1993). Known as 3D-DIC, the method was improved (Helm 1996) and used to quantify the complex 3D deformations. The method was successfully extended to the study of high rate events such as blast loading of small structures with the goal of estimating the dynamic response and pressure conditions applied to the structure. Unfortunately, this method requires modifications to account for the effect of refraction when viewing objects through media having different indices of refraction. Although immersing stereo vision system could mitigate refraction problems,

it is not feasible in many applications. Few researchers (Ke 2009) have developed a dual calibration process to account for refraction effects in digital image correlation. However, this method has not been validated by experiments and has not been applied to measure flow fields.

## 1.3 EXPLOSIVE THREATS

In modern warfare, there has been "a dangerous shift from the familiar standard issue weapons, to the use of improvised explosive devices (IEDs)" (DOD 2010). An IED (Kempinski 2012) is a bomb that is fabricated in an improvised manner; incorporates destructive, lethal, noxious, pyrotechnic, or incendiary chemicals; and is designed to destroy or incapacitate personnel or vehicles. The term "improvised explosive device" comes from the British Army and its 1970s struggle with the Irish Republican Army although the same types of devices under different names were used in several wars prior to that one, including World War II and, extensively, the Vietnam War. IEDs may incorporate military or commercially sourced explosives, or, in many instances, both. They may also be made with homemade explosives. They may use shaped charges, especially explosively formed penetrators (EFPs), or blast or fragmentation warheads, depending on the intended target.

The wars in Iraq and Afghanistan highlighted the devastating effect that well-placed IEDs could have on all of the military's road vehicles and their crews. By 2007 it was reported that in Iraq more than half of all American fatalities are now being caused by powerful roadside bombs that blast fiery, lethal shrapnel into the cabins of armored vehicles. One commonly cited source, the Iraq Coalition Casualty Count, shows a steady increase in the number of IED fatalities, as seen in Figure 1.1 (http://www.defense-

update.com). Given the potential for catastrophic damage from those devices to a vehicle and its crew, the IED threat itself had an impact on tactics, techniques, and procedures for the military, both when soldiers were on foot and in vehicles. Vehicle speeds dropped precipitously as the IED threat became apparent because crews attempted to visually inspect roadways for indications of an emplaced IED. In addition, crews and vehicles were developed and dispatched with the specific purpose of performing route clearance of emplaced IEDs. The impacts of both of those changes on the operational tempo of troops confronting the IED threat are significant.

Due to the ever changing tactics of warfare, there is a rapidly evolving need for better protection against improvised explosive device (IED) attacks. To reduce damages and injuries, the DOD spends millions dollars in improving the design of military vehicles although the budget is recently cut to $11 million. However, IEDs remain potentially fatal threats, especially in conflicts areas nowadays.

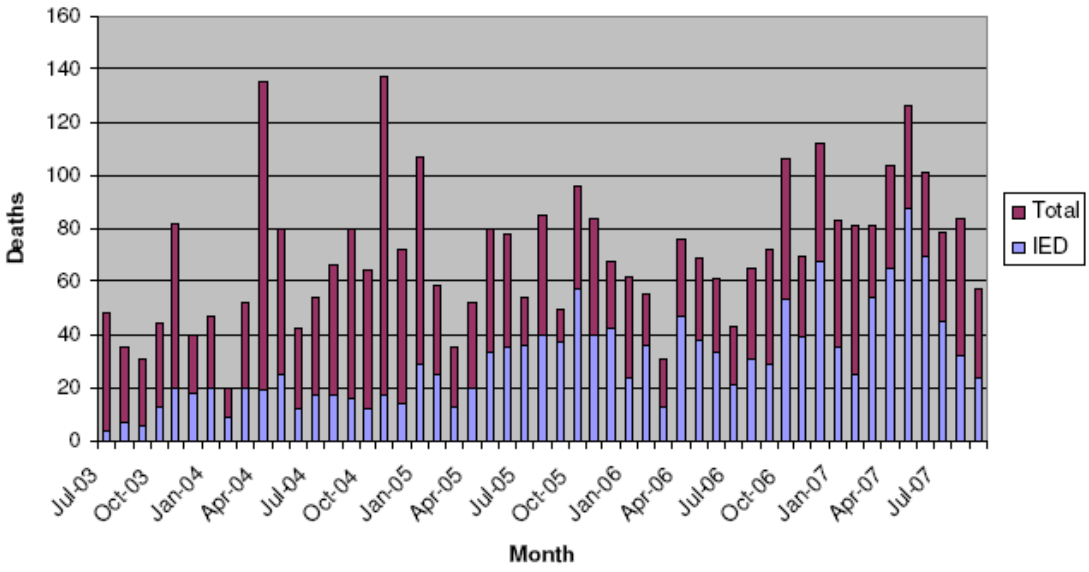


Figure 1.1 Fatalities in Iraq by IEDs.

## 1.4 SCALING

Dynamic tests are conducted on a small scaled model in order to obtain the response characteristic of a geometrically similar full-scale prototype which is the actual system of interest. During this procedure, modeling or similitude is governed by certain principles. This procedure is known as scaling. Scaling is powerful and commonly used. It can improve the understanding of physical phenomenon and the analysis. In practice, small scale model are lower cost, quicker execution and increased accessibility. Instead, full scale test, such as full-scale vehicle testing "are very expensive, and each damage test by land mine detonation expends not only the vehicle but also many man-hours of skilled engineering and support labor" (Wenzel 1973). More important, results of scaled model could be scaled up to full-scale prototype quantitatively.

## 1.5 PARTICLE TRACKING STUDY

A manufacturing process, known as friction extrusion, was invented and patented at the Welding Institute (Cambridge, UK) in 1993 and subsequently largely ignored until the patent lapsed in 2002. Until now, there is little literature involving the friction extrusion process (Tang 2010). However, the friction extrusion process, which is derived from friction stir welding shown in Figure 1.2(a), is being developed and refined to demonstrate its potential for helping to reduce the cost of the increased performance in aerospace structures. As shown in Figure 1.2(b), the friction extrusion is a friction based process which can be produced high quality wire, rod, disk or fully consolidated bulk via consolidation and extrusion of recycling materials like machining chips, low-cost titanium powder as well as metal blocks. The extrusion die rotates about the extrusion axis and is loaded downwards. At first, the billets will be consolidated under high

pressure in the chamber. Then severe plastic deformation occurs in the billets and generates a large amount of heat which results in a temperature increase in the material. Significantly, temperature rise in the billet could be achieved solely by deformation heating rather than by external heating of the billet chamber although external heating may also be utilized. Under high pressure, the metal will be extruded out through the extrusion hole and form a wire or other models. To help extrude the metal out, scroll geometry may be used on the surface of the extrusion die that contacts with the billet charge. The friction extrusion process would likely be economical and "green". It demonstrates the potential for creating high value products from low value input streams. Unfortunately, to date there has been limited success in extruding long sections of wire, most likely due to a lack of understanding of the transient material deformation processes that are occurring as wire is heated and extruded from the billet chamber.

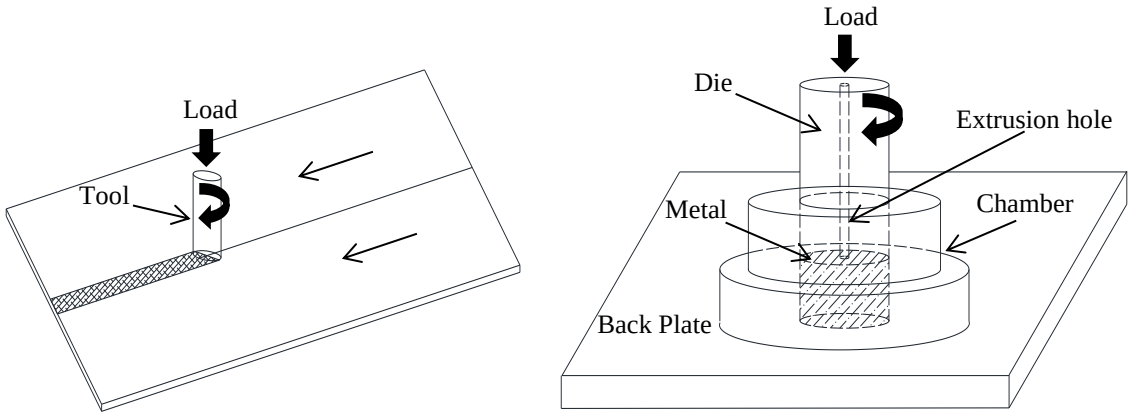


Figure 1.2 Schematic of (a) friction stir welding and (b) friction stir extrusion.

# CHAPTER 2

## SCALING OF STRUCTURE SUBJECTED TO SAND BLAST LOADING

### 2.1 LITERATURE REVIEW

Scaling of explosive events has a long history. Hopkinson (Hopkinson 1915) near the beginning of WW1 and Cranz (Cranz 1926) in Germany in the 1920s were two of the earliest investigators to study how scaling would be employed for quantifying the effects of different spherical air blast waves. While studying a specific physical property, they showed that both the distance from the center of the explosion and the time at which it is evaluated are proportional to the diameter of the spherical charge. Since the diameter is proportional to the cube root of the charge mass, their results imply that both the physical time and measurement position at which a physical property is evaluated are proportional to the cube root of the energy released by the explosive mass. In 1965, Chabai (Chabai 1965) published his studies regarding the proper scaling of crater dimensions resulting from buried explosives. He performed detailed dimensional analysis and developed four different scaling rules, including the well-known 1/3 power rule. Chabai used data generated from a series of explosive experiments to discern which scaling rules are most relevant for crater size estimation.

In recent experimental and scaling works, Nurick and Shave (Nurick 1995) experimentally studied the failure of thin edge clamped steel plates subjected to explosive loading by using a ballistic pendulum. The authors estimated the total impulse and analyzed the type of failure mode experienced by the clamped plate. Zhu (Zhu 1995)

used streak camera to obtain the early transient deformation of square plate under air explosive loading. Though, the optical technique employed is dependent on the presence of symmetric deformation in the plate. Zhu showed good agreement between numerical and experimental results for the transient deformation reported. Jacob et al (Jacob 2004) reported a series of experimental results and numerical predictions for clamped mild steel quadrangular plate of different thickness and varying length-to-width ratios subjected to localized blast loads of varying size. They introduced a localized loading parameter to the dimensionless damage number to simplify the complexity of interaction between charge diameter and plate geometry and showed good agreement between their findings and the results of Nurick (Nurick 1989). For the studies by Alves and Oshiro (Alves 2006), the authors used impact mass, impact velocity and stress as dimensionless variables to analyze (a) the axial impact of a mass on a strain rate sensitive type Ⅱ double plate structure and (b) the transverse impact of a mass on a strain rate sensitive clamped beam. Their results showed that a correction procedure was required to match the scaled model and prototype results. Neuberger and his co-authors (Neuberger 2007) have been actively studying the applicability of scaling in air blast as well as buried blast explosions. Focusing primarily on simulations, the authors acquired a limited set of measurements for the center-point maximum surface displacement using a specially devised comb-like device.

Regarding analytical models and numerical simulations studies for blast loading events, in the 1950s, Hudson (Hudson 1950) performed theoretical studies to describe the observed motion and plastic deformation of clamped metal diaphragms used in certain underwater explosion experiments. The theoretical solutions specified the final deformed

diaphragm profile, the distribution of thickness after deformation, the swing-time (total time for deformation to take place) and other quantities. Wang and Hopkins (Wang 1954) developed a theoretical analysis based on the Tresca yielding failure criterion and associated flow rule for the deformation of built-in circular plates under uniform dynamic loads of sufficient intensity to cause plastic deformation. The most important results from these studies are the estimation of total plate response time and residual deflection. In the 1960s, Florence (Florence 1966) performed theoretical studies of clamped circular plates subjected to blast loading uniformly distributed over a central circular area. Assuming rigid-plastic material properties, he showed the dependence of the permanent central deflection on pressure, impulse when the blast pulse is taken as a rectangular pulse. In 1972, Johnson (Johnson 1972) presented results from impulsive loading of thin metal plates, where the analytical studies assumed that plastic deformation was due to bending loads and elastic strains were negligible. In 1979, Bodner and Symonds (Bodner 1979) investigated the relation between deflections estimated by the "mode approximation" technique. The results were later extended to large deflections by Symonds and Chon. In the 1990s, Yu and Chen (Yu 1992) improved the estimates of large defection dynamic plastic response of simply-support or fully-clamped rectangular plates based on the bending-only theory and provide a new way to trace the transient phase of dynamically loaded plates when the effect of membrane forces is significant. Olson et. al. (Olson 1993) presented experimental and numerical results for clamped square mild steel plates subjected to uniformly distributed blast pressure loading. Three modes, large ductile deformation, tensile-tearing and transverse shear, are exhibited and compared with the prediction of numerical studies. Recently, Zaera (Zaera 2002) proposed a yield criterion

and reported an analytical approach based on an energy balance equation for the dynamic response of metallic circular plate subjected to impulsive loads. He showed the results are close to those obtained by experiments. Schleyer (Schleyer 2003) used an assumed-mode, elastic-plastic analytical approach to predict the maximum and residual deflections of the test plates under dynamic loading with an approximate triangular form and showed reasonable success. Taylor & Szymczak (Taylor 2007) have shown that their computations compare favorably with post-blast observations, the global velocity data and measured impulse. Gupta and Nagesh (Gupta 2007) numerically studied the deformation, tearing and shock absorption response of clamped circular plates under uniform impulsive loads with ring support of varying edge configuration at the boundary. Yankelevsky et. al. (Yankelevsky 2008) studied the pressure distribution along the rigid obstacle for various stand of distances of the explosive, buried in soil, from the obstacle and used modified variational-difference method and Lagrange approach to simulate the process. Zakrisson et. al. (Zakrisson 2011) performed numerical simulations of air blast loading in the near-field acting on deformable steel plates and compared to experiments. Rimoli et. al. (Rimoli 2011) utilized a combination of experimental and modeling methods to investigate the mechanical response of edge-clamped sandwich panel and equivalent monolithic plates subjected to localized high intensity dynamic loading, which was generated by the detonation of spherical explosive charges encased by a concentric shell of wet sand placed at difference standoff distances.

A common thread in all of the experimental studies noted previously is the use of limited measurement data: single-point deflection and/or post-deformation shape of the plate. Use of full-field deformation and motion measurements throughout the transient

loading regime would significantly improve the assessment of the quality of model predictions, while also providing baseline data to improve theoretical analyses, especially for blast loading studies.

In this chapter, both dimensional analysis results and the design of a set of scaled experimental configurations subjected to saturated sand blast loading are described in detail. This study focuses on use of small charges and depths of burial to determine the range of parameters where scaling remains effective. Then, results from a comprehensive set of experimental measurements report for surface deformations during the blast loading process including (a) 3D surface displacements, (b) surface strain components, (c) surface velocity and acceleration components for the out-of-plane displacement field and (d) surface strain rate components. Results include comparisons of the scaled measurements to the baseline data in the form of temporal variations as well as spatial variations for the plates.

## 2.2 DIMENSIONAL ANALYSIS

The authors identified an appropriate set of input and output parameters for a circular plate specimen subject to saturated sand blast loading. The Buckingham π-theorem (Bridgman 1949, Jones 1989) is used to generate a complete set of dimensionless π-terms, with equality of these π-terms for different experiments producing the scaling requirements, which are used in the design of the plates and surrounding frames.

### 2.2.1 DIMENSIONAL ANALYSIS VARIABLES

For plate impact due to the expulsion of sand during detonation of a buried explosive, the independent variables and their dimensions are listed in Table 2.1. The input variables consist of three principal components: geometrical characteristics, material properties and

explosive parameters. The geometry of the plates and frames are specified by characteristic length parameters, which are taken as the plate thickness, plate dimensions and frame dimensions. The material properties include the density of sand and mechanical properties of the plate and the frame. The explosive energy, depth of burial (DoB) and stand-off distance (SoD) are selected since they play important roles in the transfer of energy to the specimen. The output or response parameters in this study include the spatial and temporal variations for all of the following: displacement, velocity and acceleration vectors, residual deflection, surface strain components and surface strain rate components.

Table 2.1 Scaling factors and dimensions for variables

| **Variables** | **Dimensions** | **Scaling Factor** |
|---|---|---|
| **Input** | | |
| **x** plate coordinate position vector | L | β |
| h plate thickness | L | β |
| $L_p$ plate in-plane dimension | L | β |
| $\sigma_0$ plate initial yield stress | $ML^{-1}T^{-2}$ | 1 |
| $E_p$ plate Young's modulus | $ML^{-1}T^{-2}$ | 1 |
| $\rho_p$ mass density of plate | $ML^{-3}$ | 1 |
| $U$ explosion energy | $ML^{2}T^{-2}$ | β |
| d(DoB) depth of buried explosive from sand surface | L | β |
| D(SoB) stand-off distance from plate to sand surface | L | β |
| $\rho_s$ sand mass density | $ML^{-3}$ | 1 |
| $L_f$ frame dimensions | L | β |
| $E_f$ frame Young's modulus | $ML^{-1}T^{-2}$ | 1 |
| $\rho_f$ frame mass density | $ML^{-3}$ | 1 |
| t time | T | β |
| **Response** | | |
| $\mathbf{U}$ plate displacement vector | L | β |
| $\dot{\mathbf{U}}$ plate velocity vector | $LT^{-1}$ | 1 |
| $\ddot{\mathbf{U}}$ plate acceleration vector | $LT^{-2}$ | 1/β |

Table 2.1 Scaling factors and dimensions for variables (cont′d)

| **Variables** | **Dimensions** | **Scaling Factor** |
|---|---|---|
| **Response** | | |
| $\Delta$ permanent axial deflection of plate | L | $\beta$ |
| $\varepsilon$ strain | \ | 1 |
| $\dot{\varepsilon}$ strain rate | $T^{-1}$ | $1/\beta$ |
| H height | L | $\beta$ |
| P impulse | $MLT^{-1}$ | $\beta^3$ |
| E potential energy | $ML^2T^{-2}$ | $\beta^4$ |

According to the Buckingham π-theorem, three parameters are selected as repeating variables to span the primary dimensions. In this work, they are: (a) Young's modulus of the plate, $E_p$, (b) mass density of the plate, $\rho_p$, and (c) explosion energy, $U$. Using this set of repeating variables, the Buckingham π-analysis gives the following non-unique set of input and output non-dimensional π-terms:

$$\Pi_1 = \frac{x}{\sqrt[3]{\frac{U}{E_p}}},\ \Pi_2 = \frac{h}{\sqrt[3]{\frac{U}{E_p}}},\ \Pi_3 = \frac{L_p}{\sqrt[3]{\frac{U}{E_p}}},\ \Pi_4 = \frac{\sigma_0}{E_p},\ \Pi_5 = \frac{SOD}{\sqrt[3]{\frac{U}{E_p}}},\ \Pi_6 = \frac{DOB}{\sqrt[3]{\frac{U}{E_p}}},\ \Pi_7 = \frac{\rho_s}{\rho_p},$$
$$\Pi_8 = \frac{L_f}{\sqrt[3]{\frac{U}{E_p}}},\ \Pi_9 = \frac{E_f}{E_p},\ \Pi_{10} = \frac{\rho_f}{\rho_p},\ \Pi_{11} = \frac{t}{\sqrt[6]{\frac{\rho_p^3 U^2}{E_p^5}}},\ \Pi_{12} = \frac{U}{\sqrt[3]{\frac{U}{E_p}}},\ \Pi_{13} = \frac{\ddot{U}}{\sqrt[2]{\frac{E_p^2}{\rho_p^2}}},\ \Pi_{14} = \frac{\ddot{U}}{\sqrt[3]{\frac{E_p^4}{\rho_p^3 U}}},$$
$$\Pi_{15} = \frac{\Delta}{\sqrt[3]{\frac{U}{E_p}}},\ \Pi_{16} = \varepsilon,\ \Pi_{17} = \dot{\varepsilon} \cdot \sqrt[6]{\frac{\rho_p^3 U^2}{E_p^5}} \qquad (2\text{-}1)$$

According to the similitude analysis in Gibbings' studies (Gibbings 1982, Gibbings 1986), the function relating the non-dimensional plate displacement vector to input parameters can be written as:

$$\Pi_{12} = f\left(\Pi_1,\ \Pi_2,\ \Pi_3,\ \Pi_4,\ \Pi_5,\ \Pi_6,\ \Pi_7,\ \Pi_8,\ \Pi_9,\ \Pi_{10},\ \Pi_{11}\right) \qquad (2\text{-}2)$$

and the displacement vector is expressed

$$U = \sqrt[3]{\frac{U}{E_p}}\, f\left(\Pi_1,\ \Pi_2,\ \Pi_3,\ \Pi_4, \Pi_5,\ \Pi_6,\ \Pi_7,\ \Pi_8, \Pi_9,\ \Pi_{10},\ \Pi_{11}\right) \qquad (2\text{-}3)$$

Expressions for other response variables can also be written in similar forms using the π-terms for position, **x**, and time, t. They are given as follows.

$$\dot{\mathbf{U}} = \sqrt[3]{\frac{E_p}{\rho_p}}\mathbf{g}\left(\Pi_1,\ \Pi_2,\ \Pi_3,\ \Pi_4,\ \Pi_5,\ \Pi_6,\ \Pi_7,\ \Pi_8,\ \Pi_9,\ \Pi_{10},\ \Pi_{11}\right) \tag{2-4}$$

$$\ddot{\mathbf{U}} = \sqrt[3]{\frac{E_p^4}{\rho_p^3 U}}h\left(\Pi_1,\ \Pi_2,\ \Pi_3,\ \Pi_4,\ \Pi_5,\ \Pi_6,\ \Pi_7,\ \Pi_8,\ \Pi_9,\ \Pi_{10},\ \Pi_{11}\right) \tag{2-5}$$

$$\varepsilon = \mathrm{p}(\Pi_1,\ \Pi_2,\ \Pi_3,\ \Pi_4,\ \Pi_5,\ \Pi_6,\ \Pi_7,\ \Pi_8,\ \Pi_9,\ \Pi_{10},\ \Pi_{11}) \tag{2-6}$$

$$\dot{\varepsilon} = \frac{1}{\sqrt[6]{\frac{\rho_p^3 U^2}{E_p^5}}}q\left(\Pi_1,\ \Pi_2,\ \Pi_3,\ \Pi_4,\ \Pi_5,\ \Pi_6,\ \Pi_7,\ \Pi_8,\ \Pi_9,\ \Pi_{10},\ \Pi_{11}\right) \tag{2-7}$$

$$\Delta = \sqrt[3]{\frac{U}{E_p}}f\left(\Pi_1,\ \Pi_2,\ \Pi_3,\ \Pi_4,\ \Pi_5,\ \Pi_6,\ \Pi_7,\ \Pi_8,\ \Pi_9,\ \Pi_{10},\ \Pi_{11}\right) \tag{2-8}$$

### 2.2.2 IMPLICATION OF DIMENSIONAL ANALYSIS

As shown in Eqs. (2-1) to (2-3), the displacement vector and its components can be written as $(U/E_p)^{1/3}$ times an unknown function of a series of non-dimensional parameters. Considering experiments A and B, then each displacement components of displacement for experiment B can be divided by the corresponding value for experiment A to give:

$$\frac{(\Pi_{12})_B}{(\Pi_{12})_A} = \frac{\dfrac{\mathbf{U}_B}{\sqrt[3]{\dfrac{U_B}{(E_p)_B}}}}{\dfrac{\mathbf{U}_A}{\sqrt[3]{\dfrac{U_A}{(E_p)_A}}}} = \frac{f\left((\Pi_1)_B,\ (\Pi_2)_B,\ (\Pi_3)_B,\ (\Pi_4)_B,\ (\Pi_5)_B,\ (\Pi_6)_B,\ (\Pi_7)_B,\ (\Pi_8)_B,\ (\Pi_9)_B,\ (\Pi_{10})_B,\ (\Pi_{11})_B\right)}{f\left((\Pi_1)_A,\ (\Pi_2)_A,\ (\Pi_3)_A,\ (\Pi_4)_A,\ (\Pi_5)_A,\ (\Pi_6)_A,\ (\Pi_7)_A,\ (\Pi_8)_A,\ (\Pi_9)_A,\ (\Pi_{10})_A,\ (\Pi_{11})_A\right)} \tag{2-9}$$

Assuming all π-parameters in the function, $f$ are equal (scaling has been performed) for experiments A and B, then the right hand side of Eq. (2-9) is unity, giving the following scaling equation:

$$\mathrm{U_B}(\mathrm{x}_B^s, t_B^s) = \frac{\sqrt[3]{\dfrac{U_B}{(E_p)_B}}}{\sqrt[3]{\dfrac{U_A}{(E_p)_A}}} \mathbf{U}_A(\mathrm{x_A}, t_A) = \frac{\sqrt[3]{U_B}}{\sqrt[3]{U_A}} \mathbf{U}_A(\mathrm{x_A}, t_A) = \beta\, \mathbf{U}_A(\mathrm{x_A}, t_A)$$

$$\text{when } (E_p)_B = (E_p)_A, x_B^s = \frac{\sqrt[3]{\dfrac{U_B}{(E_p)_B}}}{\sqrt[3]{\dfrac{U_A}{(E_p)_A}}} x_A = \frac{\sqrt[3]{U_B}}{\sqrt[3]{U_A}}\, x_A = \beta\, x_A; \quad \frac{\sqrt[3]{U_B}}{\sqrt[3]{U_A}} = \beta \tag{2-10}$$

$$t_B^s = \frac{\left(\sqrt[6]{\dfrac{\rho_p^3 U^2}{E_p^5}}\right)_B}{\left(\sqrt[6]{\dfrac{\rho_p^3 U^2}{E_p^5}}\right)_A} t_A = \frac{\sqrt[3]{U_B}}{\sqrt[3]{U_A}}\, \mathrm{t}_A = \beta\, \mathrm{t}_A \text{ when } (\rho_p)_B = (\rho_p)_A$$

where the scale factor $\beta$ indicates the well-known cube-root form for the scaling and hence is consistent with previous results.

Similarly, other response variables can be scaled when comparing results from experiment A and B. Assuming that the material properties for both experiments are the same, Table 2.1 presents the required scaling for all variables, along with the corresponding dimension of the parameter (M for mass, L for length, T for time). As shown in Eq. (2-10), the variable for the small plate (A) is multiplied by the scale factor in Table 2.1 to obtain the corresponding comparative value for the large plate (B).

## 2.3 DESIGN OF SPECIMENS

As shown in Eq. (2-10) and Table 2.1, scaling of the specimens is based upon the explosive energy of the charge being used. In these studies, the total charge weights for the scaling studies were 0.50 grams and 1.9 grams, respectively.[1] Letting $U_A$ be the energy associated with 0.5 grams of PETN for the small plate experiment and $U_B$ the energy associated with 1.9 grams of PETN for the large plate experiment, and assuming equal

[1] The total charge weights included both the detonator and a small quantity of PETN sheet explosive. In addition, total charge weights are limited to less than 5grams at Dynamic Effect Laboratory.

specific energy content for both charges, then $(U_B/U_A)^{1/3} \approx 1.56$.

Consistent with Eq. (2-10) and Table 2.1, the same materials are used for all specimens. The material used to fabricate all circular plates is Al6061-T6 which is obtained from the same manufacturer. In this study, $\beta$=1.56 is used for geometric scaling of the components. Table 2.2 presents the values for the geometric variables for the small plate (A) and large plate (B) specimens used in this study.

Table 2.2 Experimental geometry

| **Variables** | **Experiment A** | **Experiment B** |
|---|---|---|
| **Plates and Frame** | | |
| Plate thickness, h | 1.00 | 1.56mm |
| Plate diameter, $L_p$ | 227.6mm | 355.6mm |
| Steel frame thickness, $h_f$ | 16.3mm | 25.4mm |
| Depth of circular cutout in steel frame, $d_{co}$ | 8.2mm | 12.7mm |
| Inner and outer diameter of steel frame cutout, $D_i/D_o$ | 195.1/227.6mm | 304.8/355.6mm |
| Square steel frame outer dimension, $L_f$ | 277mm | 428mm |
| ***Explosive Positioning*** | | |
| SoD | 48.8mm | 76.2mm |
| DoB | 16.3mm | 25.4mm |

### 2.3.1 EXPERIMENTAL SETUP

Figure 2.1 shows a schematic of the overall experimental configuration. The setup is somewhat different than previous studies (Tiwari 2009) as it consists of (a) two matched Vision Research Phantom V12.1 high speed digital cameras that are focused on the circular plate,(b) two matched Vision Research Phantom V7.1 high speed digital cameras which are focused on the steel frame to provide an estimate for the impulse transferred to the plate-frame structure, and (c) one Vision Research Phantom V7.2 high speed digital camera which recorded a full field video of the structure during blast loading. The two Phantom V12.1 cameras' optical arrangement used in the experiments has the following

overall configuration: total pan angle between the two optical axes ≈ 17 °; distance from the lens to the center of plate ≈1 m; lenses used on both cameras with focal length ≈ 28mm; lens F # ≈ 8; image intensity quantization at 8 bits; cross-camera synchronization within ±1 μs using external TTL pulse; lighting using multiple halogen lamps attached to structure near the edge of sand pit.

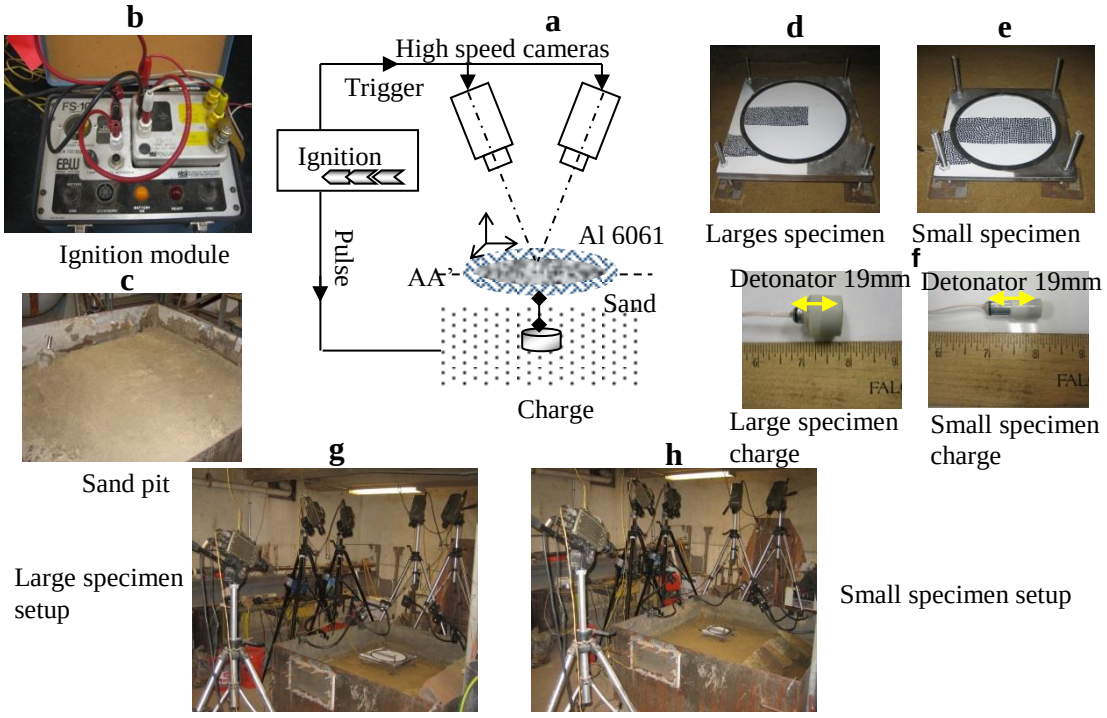


Figure 2.1 Schematic (a) with photos of the experimental setup; top left (b) ignition module; middle left(c) sand filled steel container serving as blast pit; top right: (d) large specimen with frame; (e) small specimen with frame; middle right; (f) two igniters with PETN explosive and delrin casing used to encase explosive for experiment; bottom; (g) large specimen setup for blast experiment; (h) small specimen setup for blast experiment.

Figure 2.2 shows a typical high contrast random speckle pattern that is placed on the specimen and frame in the regions of interest. The specimen and frame were lightly coated with white enamel paint and then a sharpie marker was used to manually apply a dot pattern of the appropriate size for our studies. The fields of view for the two Phantom V12.1 (http://www.visionresearch.com) cameras are 57mm × 184mm with the same

image sizes of 80 × 208 pixels for both small plate and large plate, corresponding to approximate magnification factors of 1.4 pixels/mm by 1.13pixels/mm. Average size of the permanent ink dots on each specimen is 3.2mm, corresponding to sampling by 3.6 to 4.5 pixels in each direction. The fields of view for the two Phantom V7.1 (http://www.visionresearch.com) cameras are 40mm × 40mm, with image sizes 96×96 pixels, for both small frame and large frame, corresponding to an approximate magnification factor of 2.4 pixels/mm. Average size of the permanent ink dots on each frame is 2.0mm, corresponding to sampling of each dot by 4.8 pixels in each direction.

After pattern application, the circular plate is placed in the circular recess at the bottom surface of the steel frame, covered with a steel annular ring and then tightly bolted to the steel plate using 6.35mm bolts with centers 12.7mm from the outer edge and angular spacing of $30^{o}$ around the circumference. Once the specimen is assembled to the frame fixture, threaded spacers are affixed at the four corners of the fixture. The height of the spacers is adjusted to meet the required SoD for the experiment. Then the specimen is approximately centered above the buried explosive. All of the high speed cameras are mounted on tripods which are isolated from sand pit. Stereo camera calibration is performed for both stereo-vision systems prior to blast loading. The calibration grid consists of a series of circular dots with spacing of 35mm arranged in a rectangular grid. Commercial software (Correlated Solution, Inc.) was used to convert the calibration images into the camera parameters. Once a final check is performed and the sand pit is fully saturated with water, the laboratory is evacuated and two simultaneous electric pulses are sent to the detonator to initiate the explosion and to synchronize the image acquisition for all five cameras recording the event. In this work, synchronized stereo

images are acquired with 5.25μs inter-frame time and 15.0μs inter-frame time for Phantom V12.1 and Phantom V7.1 respectively, for both the small specimen (A) and large specimen (B) experiments.

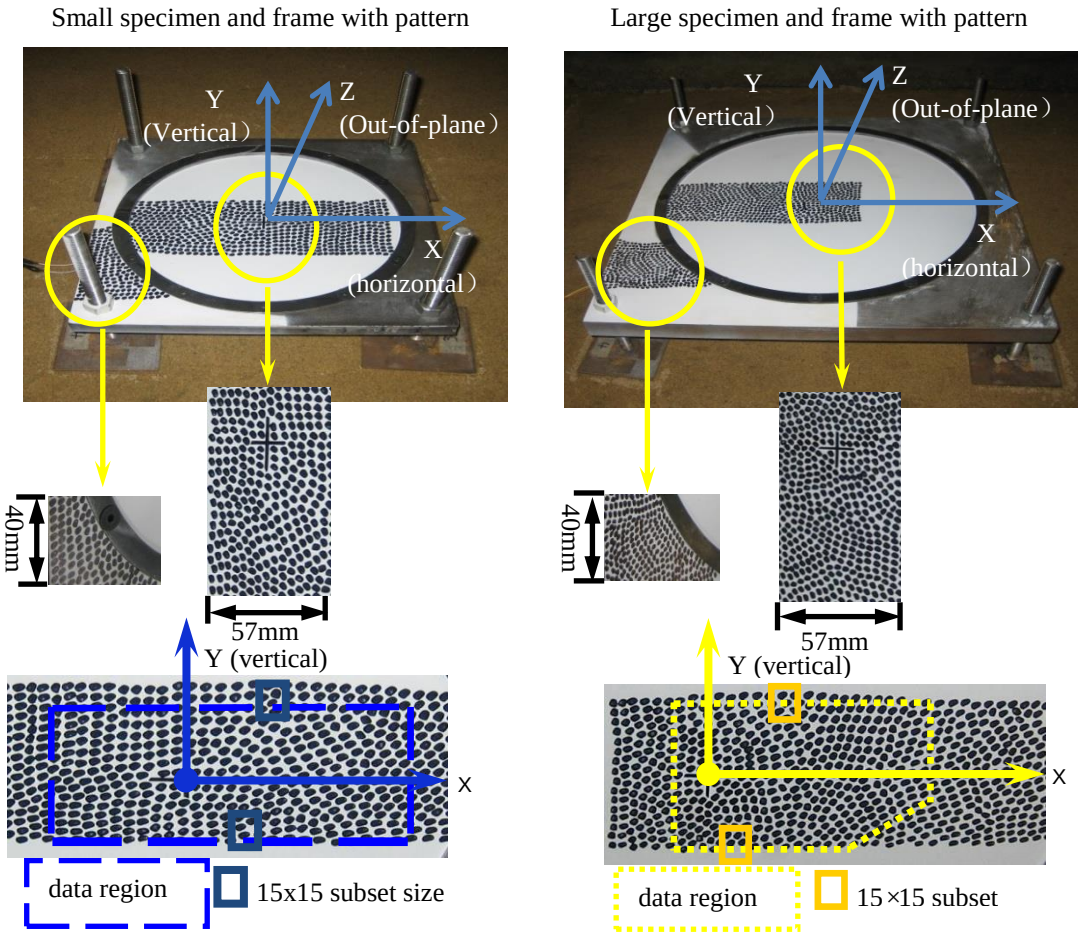


Figure 2.2 Speckle patterns for small plate and large plate specimens, with coordinate systems, data region and approximate subset size. Area imaged is 57mm by 184mm and 40mm by 40mm for both specimens.

## 2.4 PROCESSING OF IMAGES AND DATA EXTRACTION

Digital image correlation is performed using undeformed and deformed image pairs to match common image subsets within the speckle pattern (Sutton 1986, Beyer 1996, Luo 1993). After the displacement field is obtained in the X-Y coordinate system shown in Figure 2.2, out-of-plane velocity and acceleration components are obtained in the

following manner. First, a time series of data for $U_z$ at each spatial position of interest is obtained at every 5.25μs interval. Second, using this time sequence, a "moving window least squares quadratic fit" is performed in time using seven consecutive data points for each displacement component, beginning with data at time $t_o$. Third, the quadratic fit is differentiated (a) once to obtain the velocity at the midpoint of the time span and (b) twice to obtain the acceleration at the midpoint of the time span. This process is repeated by moving forward in time $\Delta t = 5.25\mu s$ and selecting seven consecutive points starting at time $t_o + \Delta t$, continuing until the entire velocity and acceleration history is obtained for a point P of the plate. Then, velocity and acceleration data are both filtered using a low pass filter with a relatively high cut-off frequency 19khz.

The Lagrangian strain field on the object at any time is obtained by least squares fitting of a quadratic function to each component of the displacement data using a $9 \times 9$ set of displacement measurements. By differentiating the local surface fit at the center point location, P, the displacement gradients for each component of surface strain are obtained at the midpoint of the $9 \times 9$ data set using Eq. (2-11)

$$\begin{aligned}
\varepsilon_{xx}(P,t_o) &= \frac{\partial u_{xx}}{\partial x}(P,t_o) + \frac{1}{2}\left[\left(\frac{\partial u_{xx}}{\partial x}(P,t_o)\right)^2 + \left(\frac{\partial u_{yy}}{\partial x}(P,t_o)\right)^2 + \left(\frac{\partial u_{zz}}{\partial x}(P,t_o)\right)^2\right] \\
\varepsilon_{yy}(P,t_o) &= \frac{\partial u_{yy}}{\partial y}(P,t_o) + \frac{1}{2}\left[\left(\frac{\partial u_{xx}}{\partial y}(P,t_o)\right)^2 + \left(\frac{\partial u_{yy}}{\partial y}(P,t_o)\right)^2 + \left(\frac{\partial u_{zz}}{\partial y}(P,t_o)\right)^2\right] \\
\varepsilon_{xy}(P,t_o) &= \frac{1}{2}\left(\frac{\partial u_{xx}}{\partial y}(P,t_o) + \frac{\partial u_{yy}}{\partial x}(P,t_o)\right) + \frac{1}{2}\left(\frac{\partial u_{xx}}{\partial x}(P,t_o)\frac{\partial u_{xx}}{\partial y}(P,t_o) + \frac{\partial u_{yy}}{\partial x}(P,t_o)\frac{\partial u_{yy}}{\partial y}(P,t_o) + \frac{\partial u_{zz}}{\partial x}(P,t_o)\frac{\partial u_{zz}}{\partial y}(P,t_o)\right)
\end{aligned} \tag{2-11}$$

To obtain the strain rate field data in the Lagrangian system employed in this work, the strain components in Eq. (2-11) are processed in a manner similar to the velocity data to obtain the strain rate field as a function of time at each point of interest since the displacement gradient components are small compared to unity.

## 2.5 EXPERIMENTAL RESULTS

Using the procedures described previously, multiple experiments are performed, three experiments are performed for the small specimen and three experiments are performed for the large specimen. Regarding estimation of variability, at each time and location where data is obtained, the maximum and minimum values for the quantity of interest are used to define a range and this range is shown as an error bar in the average value plotted in each graph.

### 2.5.1 CRATER DIMENSIONS AND RESIDUAL SPECIMEN SHAPES

Figure 2.3 shows a photograph of both the inner impacted plate surface and also the conically-shaped crater for a typical set of experiments. The average dimensions of the craters are (a) 203mm(diameter) × 55mm(depth) for the small charge and (b) 311mm(diameter) × 83mm(depth) for the large charge. The measured large crater dimensions are within 5% of the scaled small plate estimate, which is 317mm(diameter) ×86mm(depth).

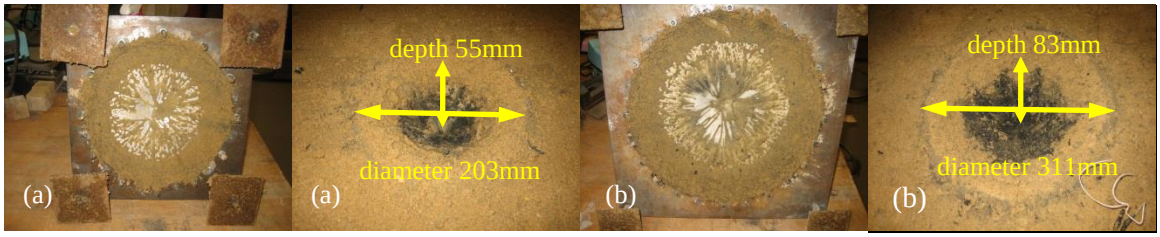


Figure 2.3 Rear sides of specimens and craters in the sand after explosion: (a) small specimen experiment; (b) large specimen experiment.

In addition to scaled crater comparisons, Figure 2.4 shows a direct comparison of residual out-of-plane displacements between the scaled small specimen and the large specimen shape. The residual shapes of plates are measured by stereo-vision with 3D-Digital Image after blast loading was completed. As shown in Figure 2.4, the general

trends are consistent for both plates with the only significant difference being the 15% difference in the scaled magnitude of the maximum residual displacement.

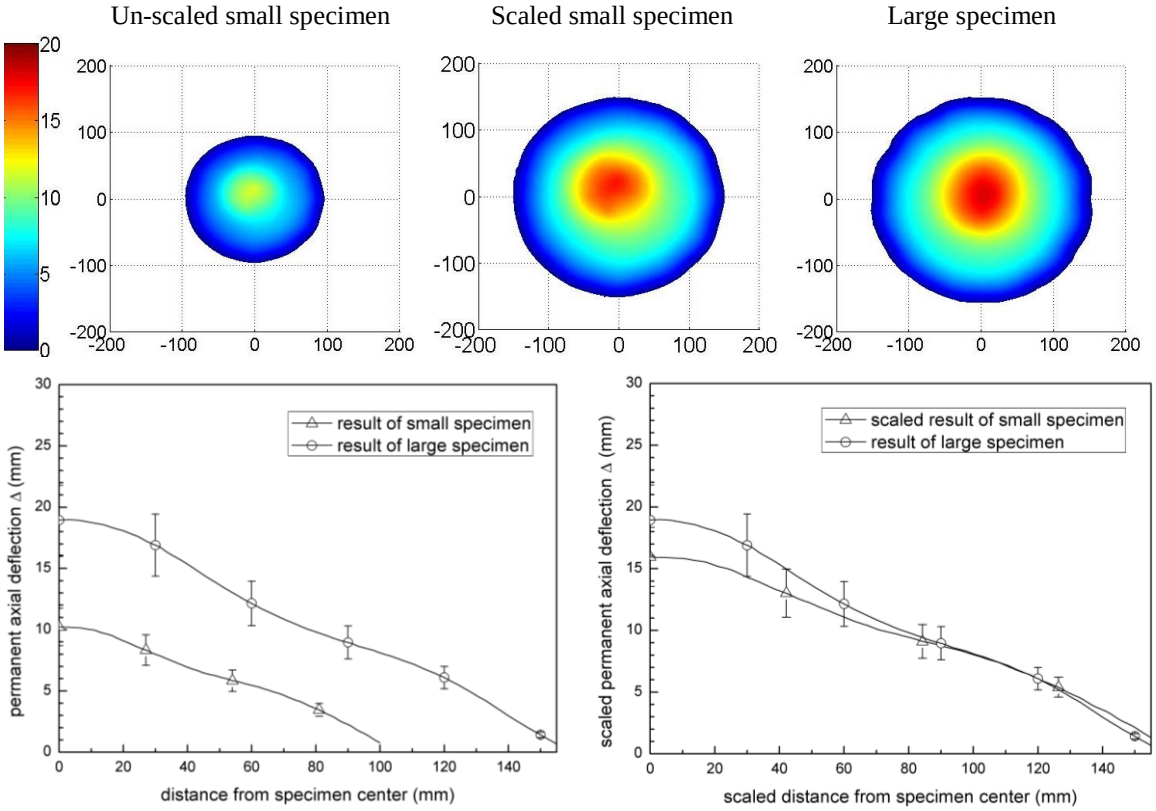


Figure 2.4 Comparison of spatial variation of permanent axial deflection. Range of Δ: ±15% for small specimen and large specimen (all unite is mm unless specified).

### 2.5.2 TEMPORAL RESPONSE FOR SPECIFIED POSITIONS

#### 2.5.2.1 PLATE CENTER

Figure 2.5 presents a time history at the approximate center-point location of the plate for the measured out-of-plane displacement $U_z$(**0,**t) in Z direction, horizontal displacement $U_x$(**0,**t) in X direction and vertical (circumferential) displacement $U_y$(**0,** t) in Y direction, where X and Y directions are shown in Figure 2.2. Results for each component include both un-scaled measurements shown on the left in the figures and a direct comparison of the large plate response to the scaled small-plate response shown on the right in the figures, where scaling is performed both for the displacement amplitude and time using

Eq (2-10). Figures 2.6 and 2.7 present the temporal variation in out-of-plane velocity and acceleration, respectively, for the large plate and small plate, as well as a direct comparison of the scaled small plate results to the large plate data.

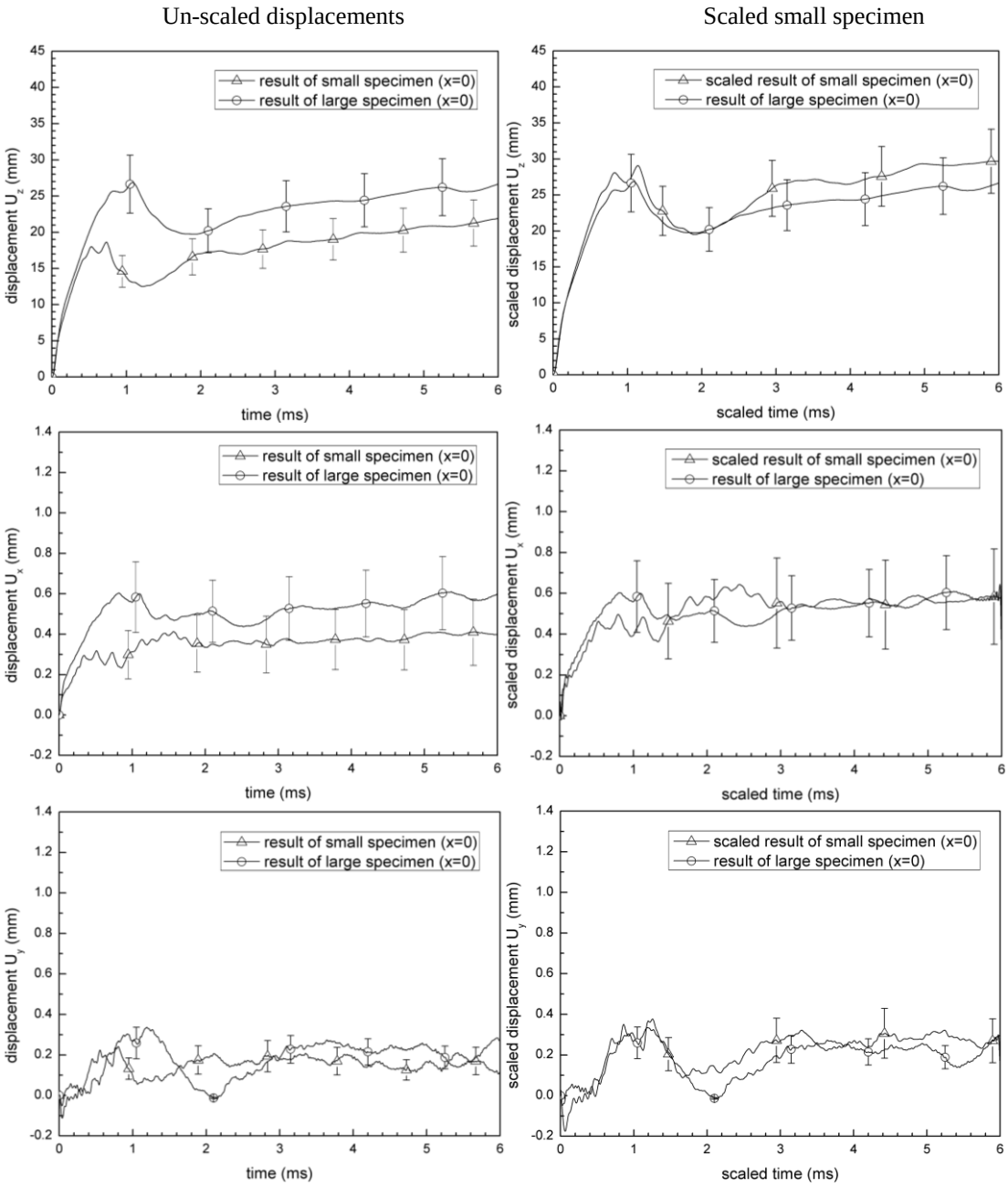


Figure 2.5 Time history of measured displacement components $U_z(\mathbf{0},t)$, $U_x(\mathbf{0},t)$, $U_y(\mathbf{0},t)$ at approximate center-point location. Range of $U_z$: ±15% for large and small specimens; Range of $U_x$: ±40% for small specimen and ±30% for large specimen; Range of $U_y$: ±40% for small specimen and ±30% for large specimen.

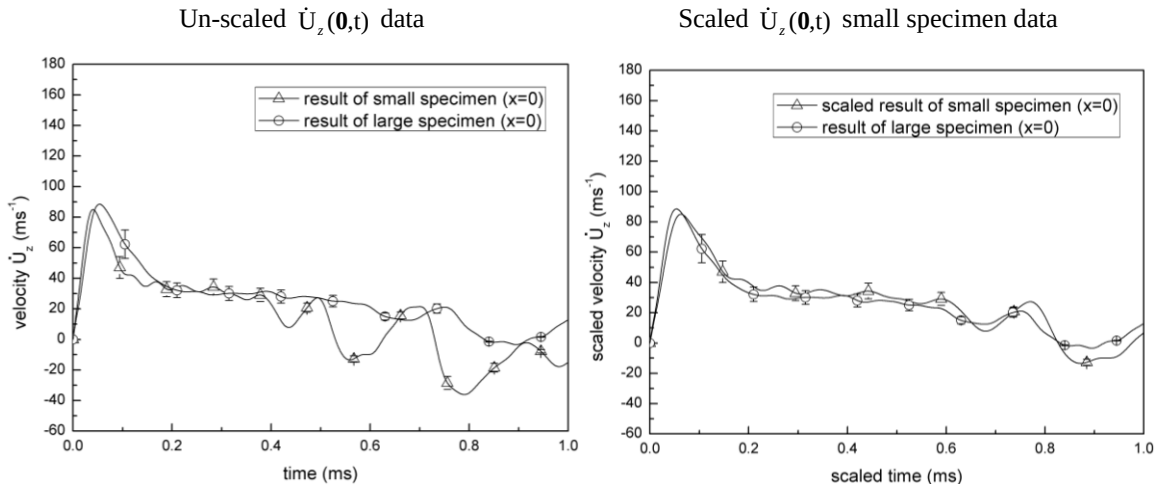


Figure 2.6 Time history for out-of-plane velocity $\dot{U}_z(\mathbf{0},t)$ at approximate center-point location. Range of $\dot{U}_z$: ±15% for small and large specimens.

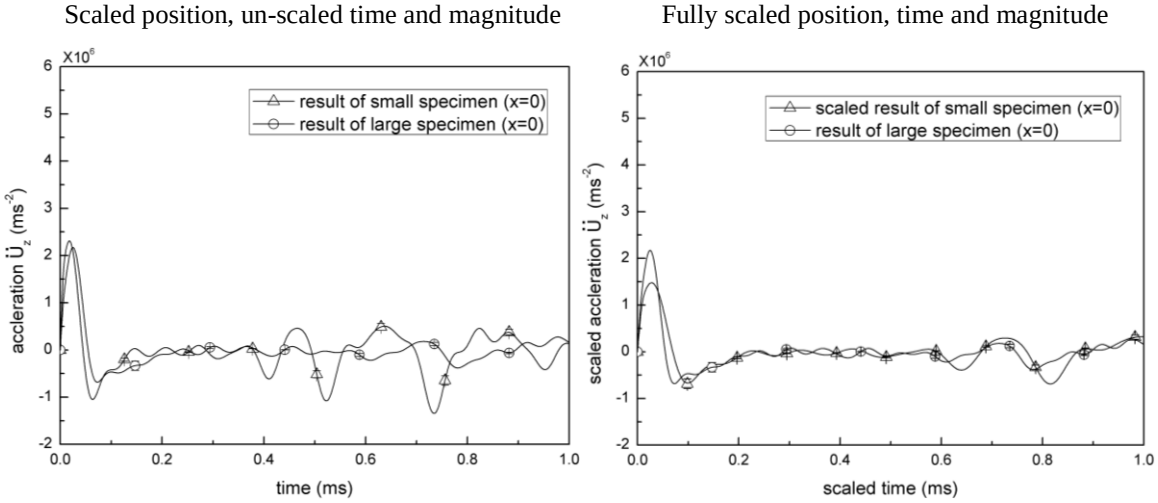


Figure 2.7 Time history for out-of-plane acdeleraton $\ddot{U}_z(\mathbf{0},t)$ at approximate center-point location. Range of $\ddot{U}_z$: ±15% for small specimen and 30% for large specimen.

#### 2.5.2.2 RESULTS AT OFFSET HORIZONTAL POSITION

Measurements of the three displacement components for a point Q located at X=50mm in the small plate and the scaled location X=78mm in the large plate are shown in Figure 2.8. Temporal variations in out-of-plane velocity and acceleration at the same points are shown in Figures 2.9 and 2.10, respectively.

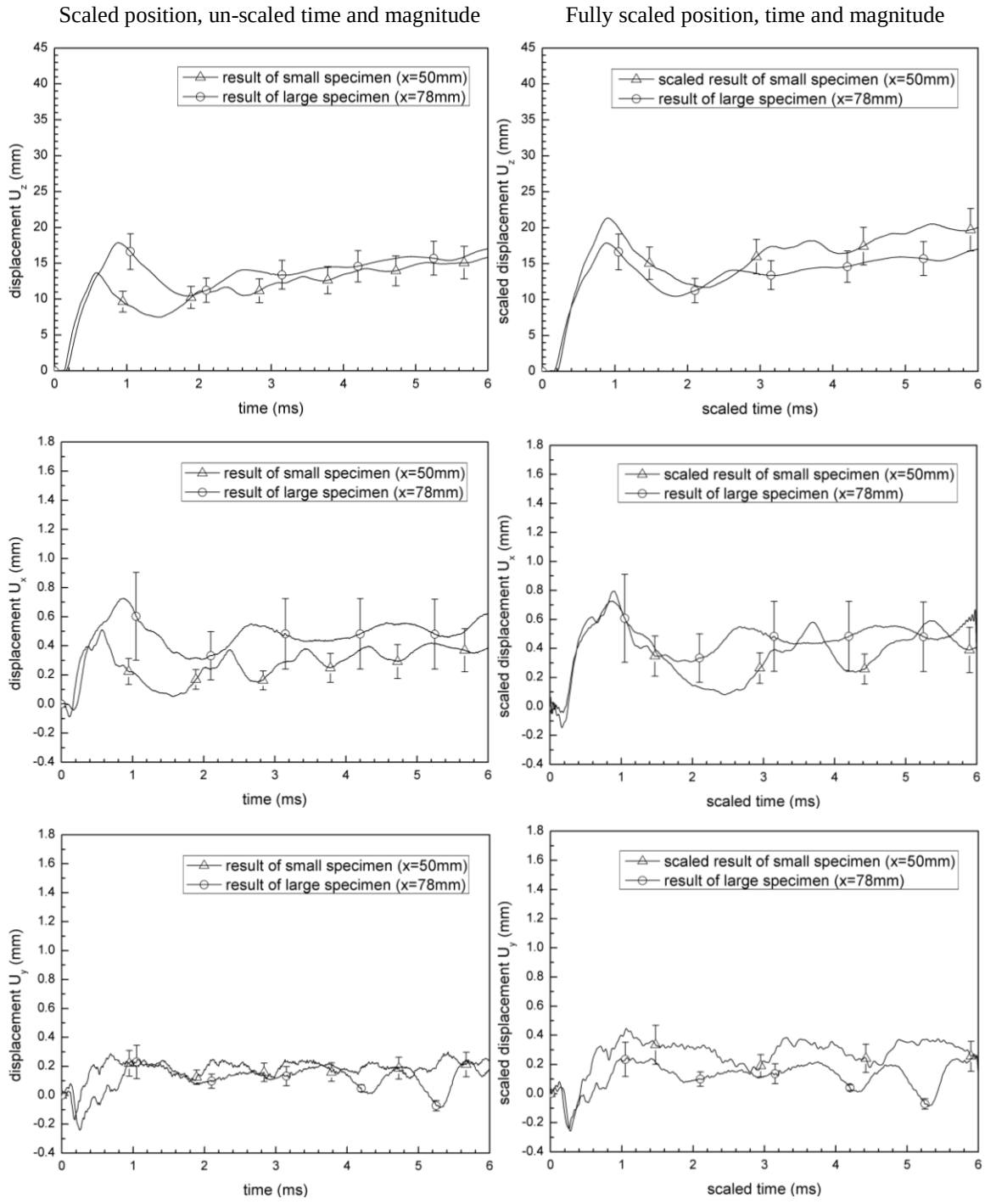


Figure 2.8 Time history of measured displacement components $U_z(\mathbf{x_0},t)$, $U_x(\mathbf{x_0},t)$, $U_y(\mathbf{x_0},t)$ at $\mathbf{x_0}$=(50mm, 0, 0) along horizontal direction away from center-point location for small specimen and the corresponding horizontal scaled location of (78mm, 0,0) for the large specimen. Range of $U_z$: ±15% for small and large specimen; Range of $U_x$: ±40% for small specimen and ±50% for large specimen; Range of $U_y$: ±40% for small specimen and ±50% for large specimen.

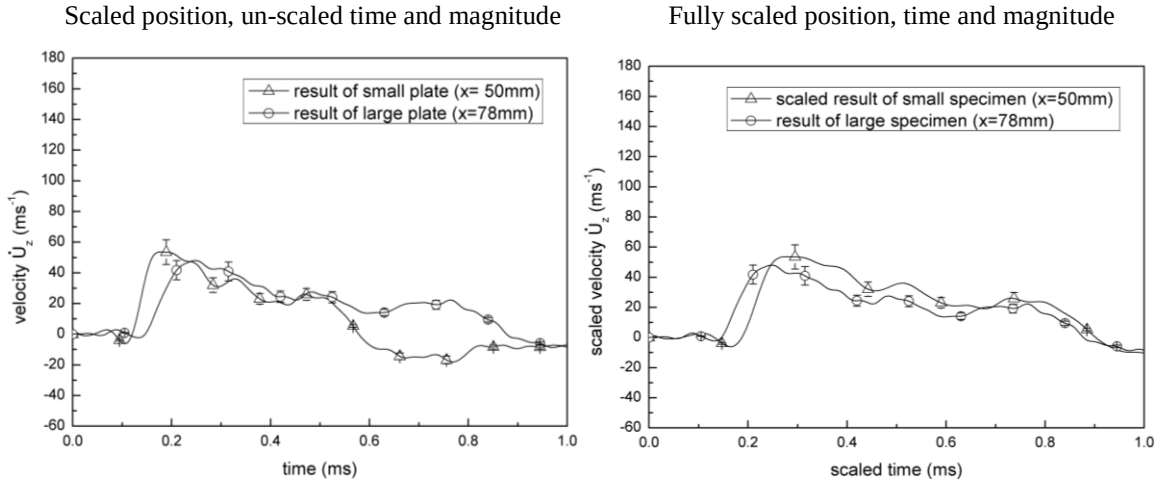


Figure 2.9 Time history of measured out-of-plane velocity $\dot{U}_z(\mathbf{x_0},t)$ at $\mathbf{x_0}$=(50mm, 0, 0) along horizontal direction away from center-point location for small specimen and the corresponding horizontal scaled location of (78mm, 0, 0) for the large specimen. Range of $\dot{U}_z$: ±15% for small specimen and large specimen.

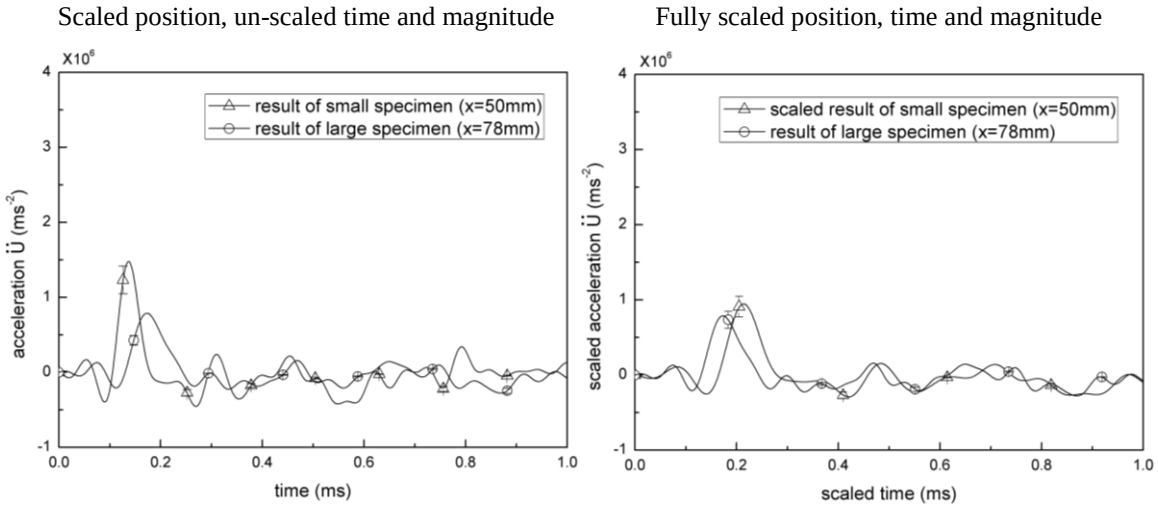


Figure 2.10 Time history of measured out-of-plane acceleration $\ddot{U}_z(\mathbf{x_0},t)$ at $\mathbf{x_0}$=(50mm, 0, 0) along horizontal direction away from centerpoint location for small specimen and the corresponding horizontal scaled location of (78mm, 0, 0) for the large specimen. Range of $\ddot{U}_z$: ±15% for small and large specimens.

For the same offset point, Q, temporal variations in the horizontal (radial), vertical (circumferential) and shear strains and strain rates are shown in Figures 2.11 and 2.12 for both the large and small plate specimens, results include both un-scaled and scaled data.

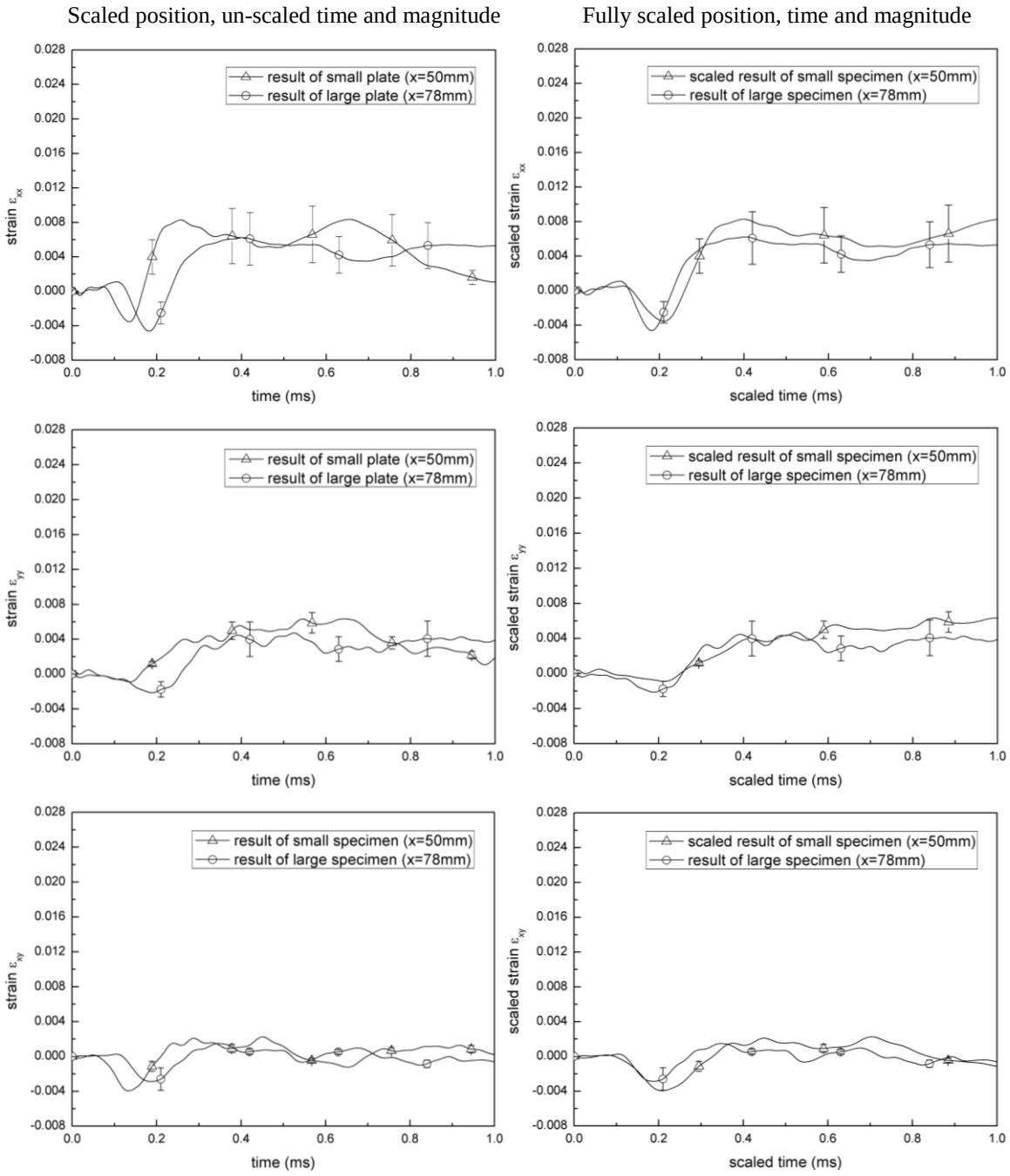


Figure 2.11 Comparison of the time history of strain components, $\boldsymbol{\varepsilon}_{xx}$, $\boldsymbol{\varepsilon}_{yy}$ and $\boldsymbol{\varepsilon}_{xy}$ at $\mathbf{x}_0$=(50mm, 0, 0) along horizontal direction away from center-point location for small specimen to the data at the corresponding horizontal scaled location (78mm, 0, 0) for the large specimen. Range of $\boldsymbol{\varepsilon}_{xx}$ and $\boldsymbol{\varepsilon}_{xy}$: ±50% for small and large specimens; Range of $\boldsymbol{\varepsilon}_{yy}$: ±20% for small specimen and ±50%large specimens.

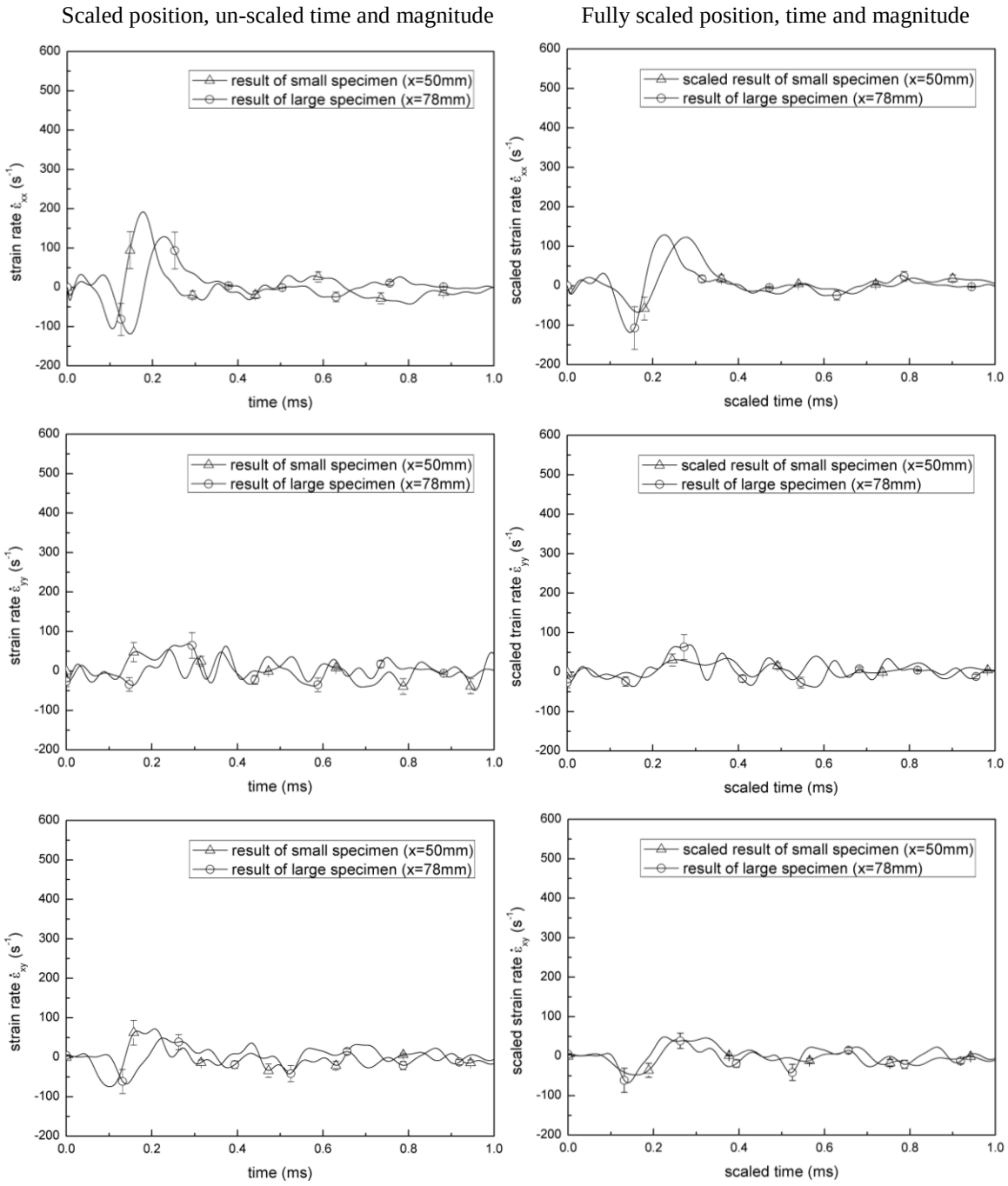


Figure 2.12 Comparison of the time history of strain rate components at $\mathbf{x_0}$=(50mm, 0, 0) along horizontal direction away from center-point location for small specimen and the corresponding scaled horizontal (78mm, 0, 0) for the large specimen. Range of $\dot{\boldsymbol{\varepsilon}}_{\mathbf{xx}}$, $\dot{\boldsymbol{\varepsilon}}_{\mathbf{yy}}$ and $\dot{\boldsymbol{\varepsilon}}_{\mathbf{xy}}$ : ±50% for small specimen and ±50% for large specimen.

### 2.5.3 SPATIAL VARIATIONS ALONG HORIZONTAL LINE

In addition to the temporal comparisons, Figures 2.13-2.15 show the spatial variations in

the out-of-plane displacement, velocity and acceleration along a horizontal line emanating from the plate centerline, respectively, for $0 \leq t \leq 1$ms.

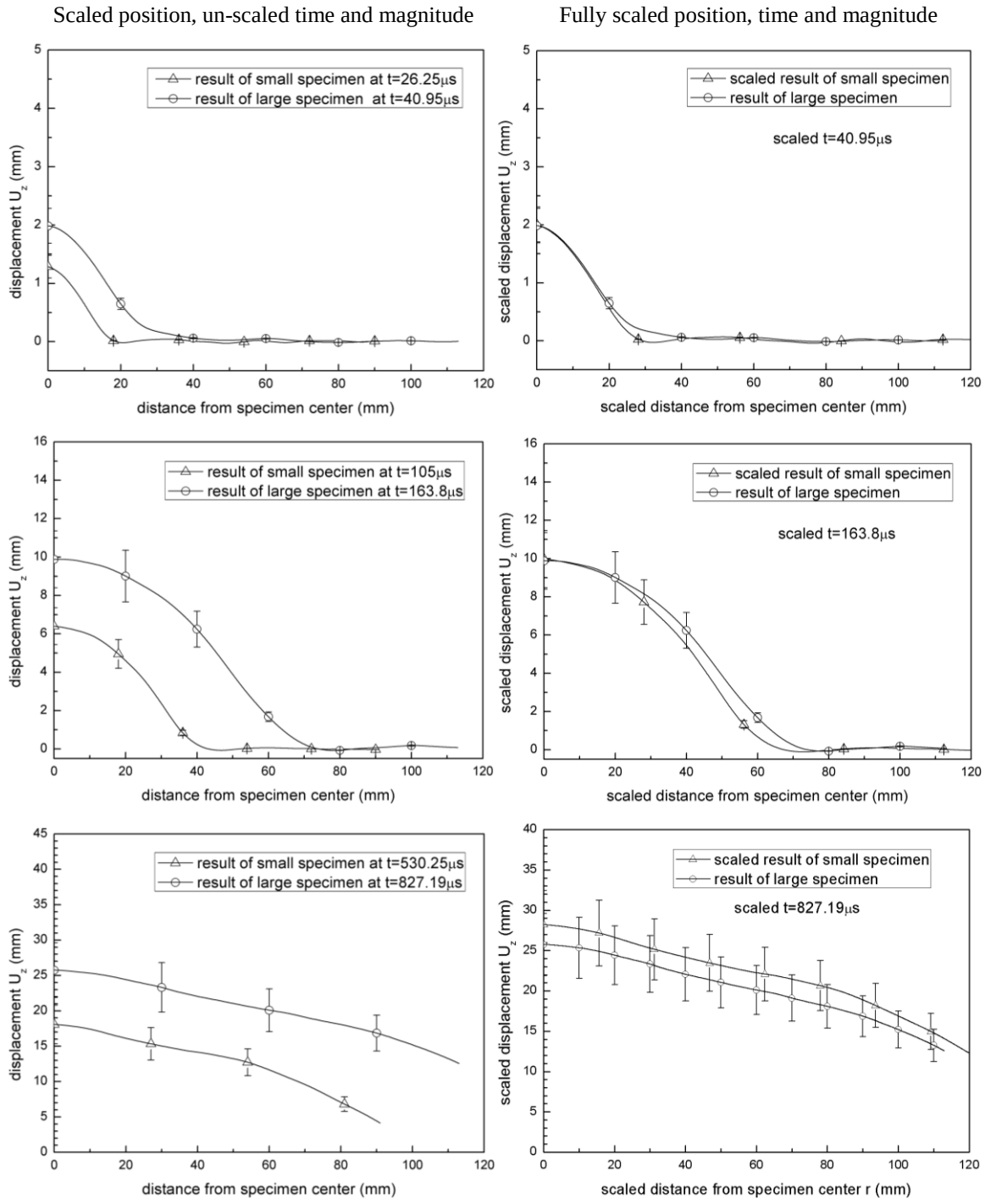


Figure 2.13 Results of the spatial variation in experimentally measured out-of-plane displacement along a horizontal line from the center-point locations at several times. Range of $U_z$: ±15% for small specimen and large specimen.

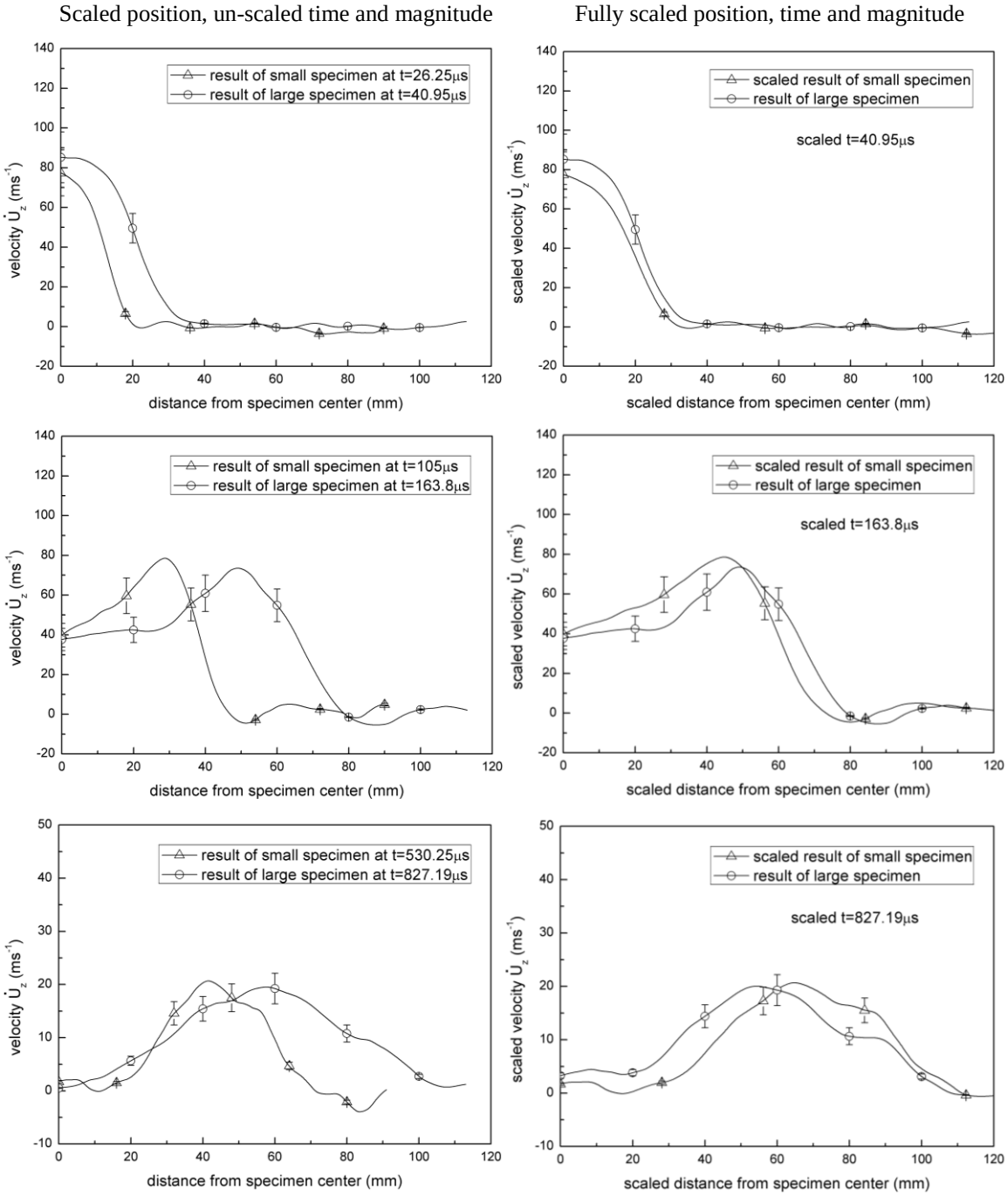


Figure 2.14 Results of the spatial variation in experimentally measured out-of-plane velocity along a horizontal line from the center-point locations at several times. Range of $\dot{U}_z$: ±15% for small specimen and large specimen.

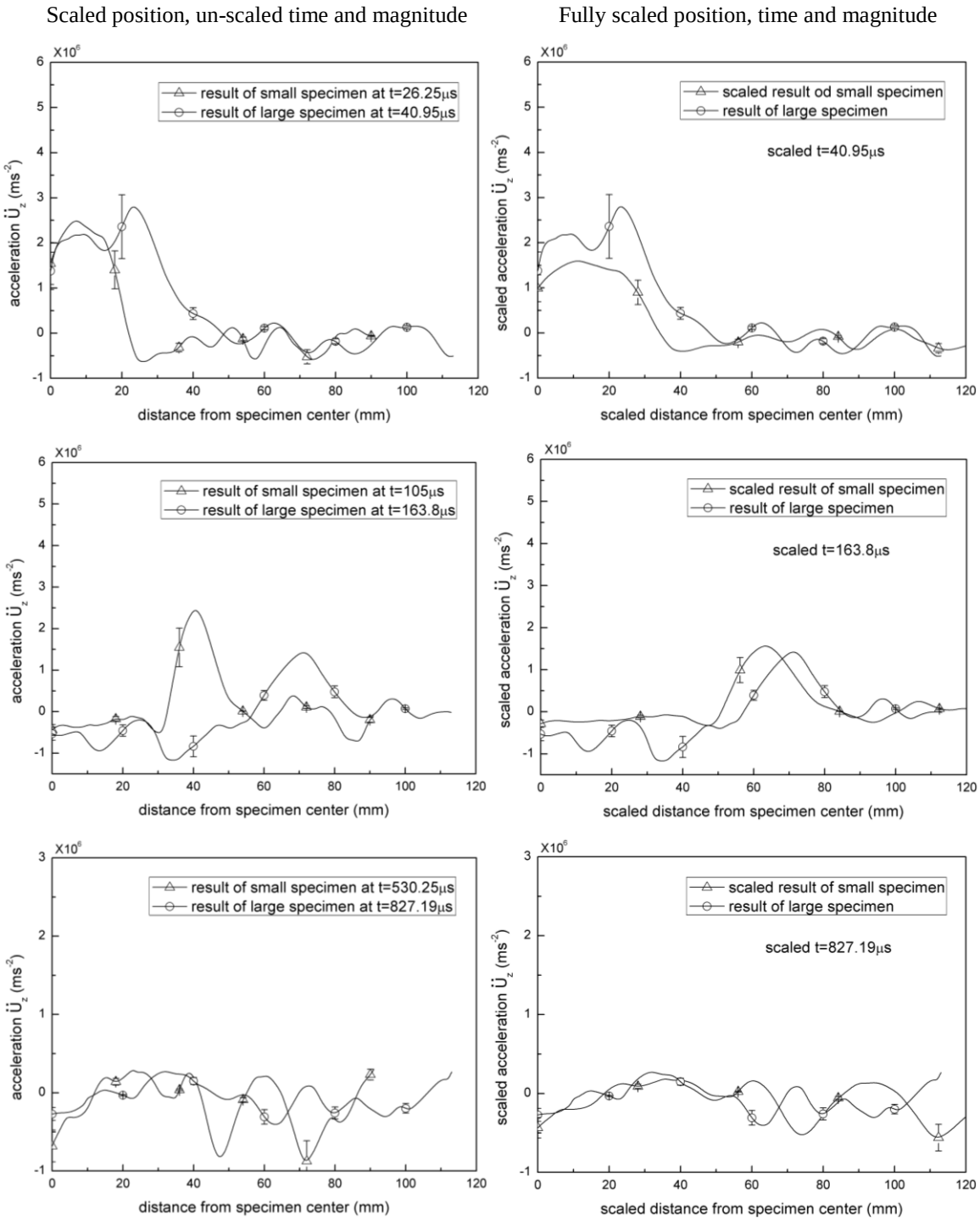


Figure 2.15 Results of the spatial variation in experimentally measured out-of-plane acceleration along a horizontal line from the center-point locations at several times. Range of $\ddot{U}_z$: ±30% for small specimen and large specimen.

### 2.5.4 DISPLACEMENT WAVE PROPAGATION

During the blast loading process, visual inspection of the image sequence shows a clearly observable vertical displacement wave propagating outward from the plate center. Defining the wave front position as the horizontal location where $U_z$ initially reaches 1mm, Figure 2.16 shows the time history of wave front propagation from the plate center along the horizontal direction.

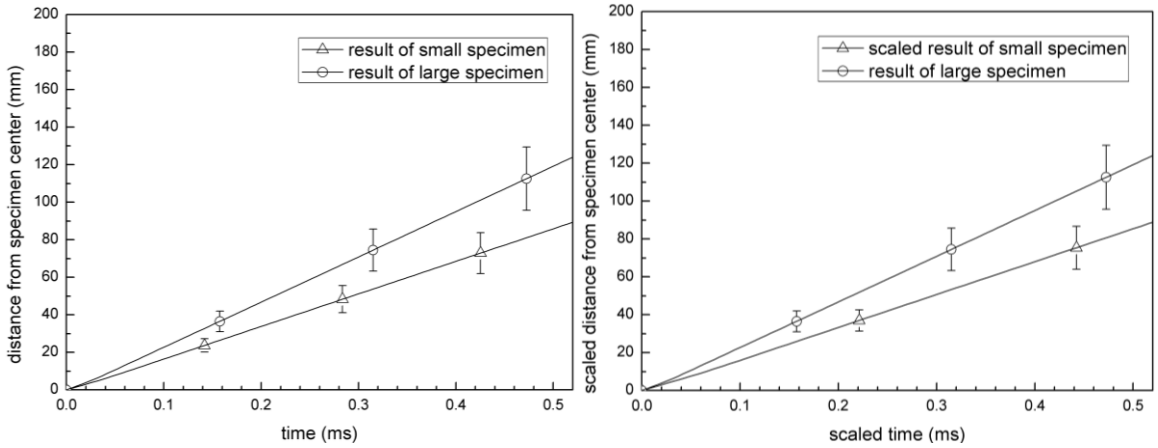


Figure 2.16 Comparison of time history of displacement wave front. Wave front propagation speeds are 173.07ms$^{-1}$ and 240.56ms$^{-1}$ in small specimen and large specimen respectively. Range: ±15% for small specimen and large specimen.

### 2.5.5 GLOBAL MEASUREMENTS

Using images from the Phantom V7.1 cameras, motion of the entire plate-frame structure is measured and the results used to extract the impulse and potential energy of the system. In addition, reviews of video data from cameras indicate that frame-plate structure move upward rigidly with minimal rotation and it is true for all the experiments performed in this study. Figure 2.17 shows the rigid movement of the small and large plate structures, including both scaled and un-scaled comparisons. Figure 2.18 presents both the total impulse and potential energy of the plate-frame system, both un-scaled and scaled comparisons.

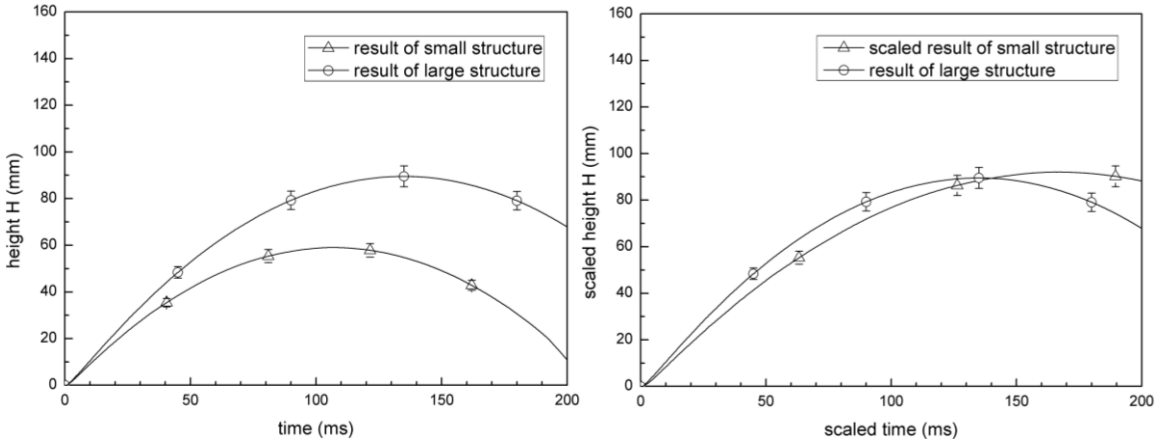


Figure 2.17 Comparison of time history of up-ward rigid movement of structure Range of H: ±5% for small plate-frame system and large plate-frame system.

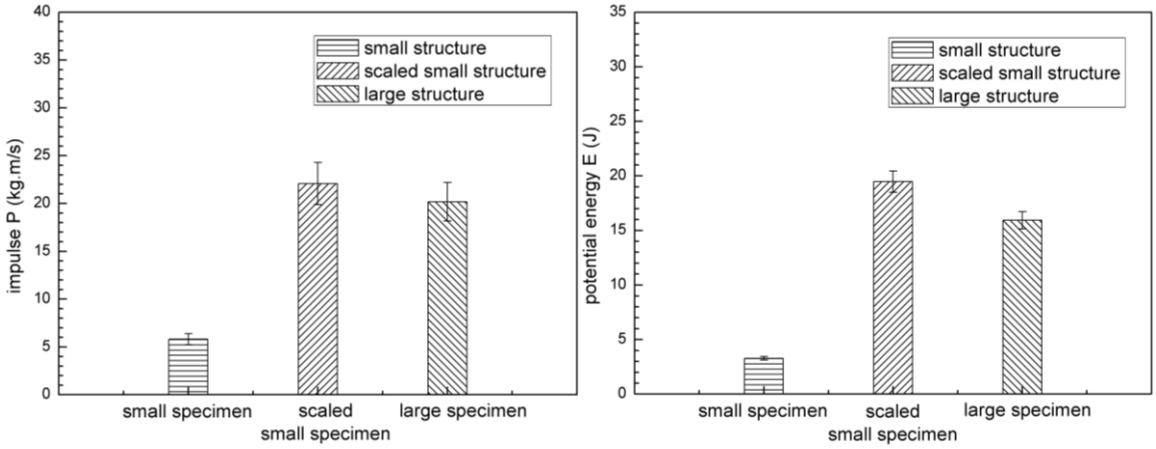


Figure 2.18 Comparison of impulse and potential energy of plate-frame structure system. Range of P: ±10% for small structure and large structure; Range of E: ±5% for small structure and large structure.

## 2.6 DISCUSSIONS

### 2.6.1 YIELD STRESS OF SPECIMEN

The vertical residual displacement data shown in Figure 2.4 indicates that the largest difference in the scaled residual data occurs at the centerline of the specimen. One plausible reason for this difference may be related to slight differences in yield stress for the two plates. Independent material characterization studies were performed to assess the accuracy of the manufacturer-supplied data and the average result from several uniaxial

experiments is shown in Figure 2.19. As shown in Figure 2.19, there is a 10-15% difference in yield stress, with the LP specimen having the higher yield stress. This slight difference is nominally consistent with the $U_z$ results in Figure 4, though scatter in the data tends to mask the effect.

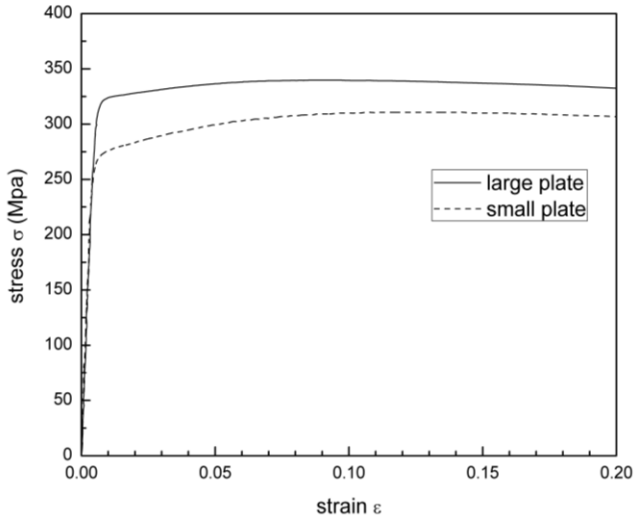


Figure 2.19 Measured uniaxial stress strain response along rolling direction for Al6061-T6 aluminum from both small plate and large plate.

### 2.6.2 SAND FINGERS AND SMALL SCALE STUDIES

For shallow buried explosives, it is well known that sand generally does not form a smooth dome-like shape after detonation has occurred. Figure 2.20 shows the shape of the sand ejecta after detonation of a buried explosive, as viewed through a transparent rubber sheet. Here, it can be seen that several small regions are ejected at higher velocity than the surrounding material, forming "sand fingers" that impact the sheet with different velocities and at different times and locations. Such effects are not modeled by the scaling law and hence will contribute to local differences in sheet response. In the context of our studies, these differences contribute to scatter in the measurements that are obtained from repeated experiments for small and large specimens. Fortunately, though

the scatter in our measurements is not small, the trends in the scaled comparisons are very good, indicating that "sand-fingering" does not alter the quality of the scaling comparisons, even though we are using the minimum explosive size and SoD in our studies.

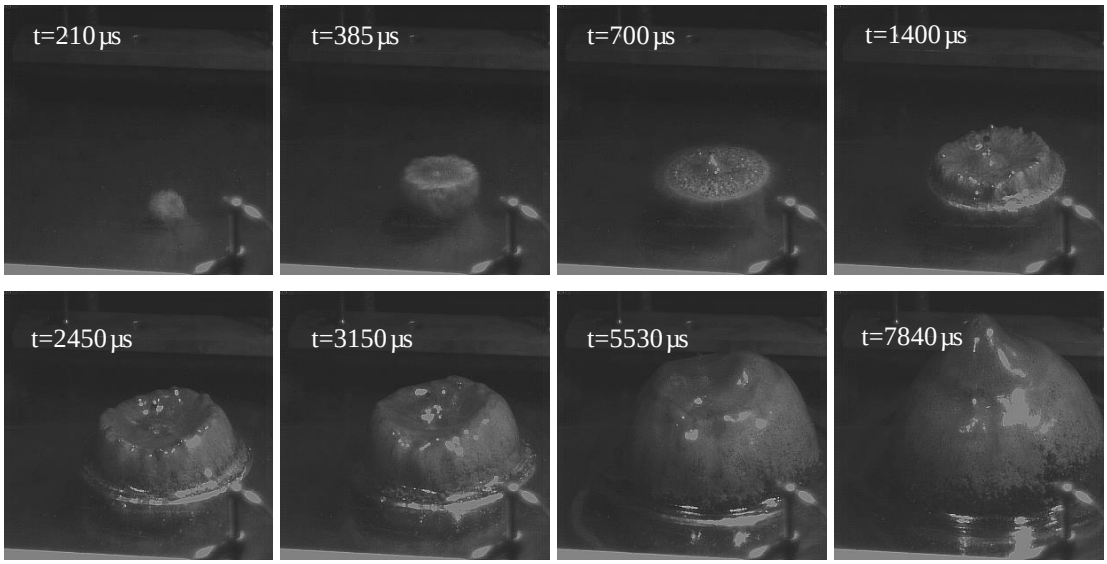


Figure 2.20 Sand fingers during DoB (0.5 inch) blast when viewed through transparent rubber sheet.

### 2.6.3 EFFECTS OF EXPLOSIVE, DETONATOR AND CONTAINER

As noted in the previous paragraph, one of the goals of our studies is to push the lower limit on explosive mass and determine whether scaling is achievable in such cases. Here, the RP-87 detonator used in experiments contains 0.203grams effective explosive, which takes up to 40.6% of total 0.5grams PETN, comparing 10.68% of total 1.9grams PETN.

In addition to an extremely small mass for the explosive, the geometry shape of detonator is not spherical, but cylindrical with a diameter of 0.27 inches and a length of 0.75 inches. Seen from the photos of charges (f) in Figure 1, part of the detonator was wrapped by the PETN sheet for the large charge, but it is not wrapped for the small charge due to geometry limitations of the 0.30 in diameter delrin casing. In such

situations, detonation can spread more quickly in the large charge, resulting in slight time differences between the small and large plates that are not accounted for in the scaling law. Also, the presence of the delrin casing could tend to focus the detonation energy somewhat, especially for the small charge experiments where the casing is smaller.

Regarding the effect of these explosive-related factors, a cursory inspection of the scaled comparisons in Figures 2.1-2.17 show that, in general, they do not affect the quality of the scaling comparisons. The one difference that may be attributed to the focusing effects of the delrin casing is the slight 5% difference in final scaled height shown in Figure 2.18. However, other factors (e.g., bolted joint effects) could have a similar effect on the measurements.

### 2.6.4 DISPLACEMENT WAVE FRONT PROPAGATION

As shown in Figure 2.16, the velocity of the displacement wave front is 173.07ms$^{-1}$ for the small structure and 240.56ms$^{-1}$ for the large structure, giving a scaled clamped-ring boundary arrival time of 0.6105ms and 0.6863ms for the small specimen and large specimen, respectively. The small difference in arrival time, which may be related to factors noted in Sections 2.5.1 and 2.5.2, will introduce a slight time shift in the scaled comparison of the measurements.

### 2.6.5 DISPLACEMENTS, VELOCITIES, ACCELERATIONS, STRAINS AND STRAIN RATES

Figures 2.5, 2.8 and 2.13 show that the temporal history for all three displacement components at two different horizontal locations is accurately scaled using Eq. (2-10); most oscillations in the measured displacement data occur at nearly the same time for both the large plate (LP) and the scaled small plate (SSP). During the early stages of the loading process, where the deformations are occurring under nominal sand-ejecta loading

conditions, there is excellent agreement in the both time and amplitudes of the large plate and the scaled small plate results for all components of displacement at both locations. The slight difference in scaled SSP magnitude for the maximum $U_z$ may be due to differences in yield stress, with dynamic yield stress estimates providing a similar comparison[2]. Inspection of Figure 2.4 (a) shows that the blast loading event is not ideal for the small plate; the shape of the large deformation zone is more irregular for the small plate and the central large deformation zone is not at the plate centerline. Taken together, these results suggest that there will be slight differences in the deformations of the central location due to irregularities in the sand blast loading process.

It should be noted that the effect of frame lift-off on the measured response is visible in Figures 2.5 and 2.8. According to the video camera, the entire frame began to move vertically around 1ms after detonation and the entire plate structure was vibrating (oscillating) during this time. The generally upward trend in the $U_Z$ measurements in Figures 2.5 and 2.8 for $t \rightarrow 1$ms is consistent with the observed upward frame motion, with the oscillations corresponding to plate vibrations.

Inspection of Figures 2.6, 2.7, 2.9 and 2.10 show that there is reasonably good agreement between the LP and SSP data for $du_z/dt$ and $d^2u_z/dt^2$ for both spatial positions considered throughout the entire time from $0 < t < 1$ms. Similar results are obtained in the range $0 \leq r \leq 120$mm at several times shown in Figures 2.14 and 2.15 The slight differences in magnitude and shift the time are believed to be due to factors noted previously.

[2] Dynamic yield stress which are calculated using Cowper-Symonds relation (Johns 1989) for large plate and small plate at approximate center location using the effective stress rate showed dynamic yield stresses between 330-350MPa for the LP and 280-300MPa for the SSP.

Inspection of Figures 2.11 and 2.12 demonstrate that, in general, all three strain components and all three strain rate components are in very good agreement throughout the entire time from $0 < t < 1$ms; both the magnitude and temporal variations can be scaled effectively with slight differences in the peak amplitudes of the components for the LP and SSP specimens.

## 2.7 CONCLUSIONS

Dimensional analysis is performed to develop the appropriate parameters to guide the design of a set of scaled experimental configurations. Using the scaled experimental configurations, blast loading of the structures is developed by detonation of small explosive charges buried in saturated sand. To assess the quality of the scaling predictions when using small explosive charges, high-speed stereo-vision system is employed successfully to quantify the transient dynamic plate displacements, velocities, accelerations, strains and strain rates over a substantial portion of the structure.

Results indicate that, in a broad sense, even when small explosive charges are used in the experiments, remarkably accurate agreement is obtained after scaling of displacements, velocities, accelerations, strains, strain rates and final deformed shape. Furthermore, given the quality of agreement and the ability to quantify strains and strain rates throughout the experiment, results also indicate that small explosive charges may be used effectively with scaling laws in blast mitigation, materials and optimal structural design studies.

## 2.8 SUMMARY

Dimensional analysis is performed to develop the appropriate parameters to guide the design of a set of scaled experimental configurations. Using the scaled experimental

configurations, buried blast loading of scaled small structures is performed by detonation of scaled explosive charges buried in saturated sand. To assess the quality of the predictions for the response of scaled structures, high-speed stereo-vision system is employed to quantify the transient dynamic plate response over a substantial portion of the structure. Results are reported for surface deformations during the blast loading process, including 3D surface displacements, surface strain components, surface velocity and acceleration components for the out-of-plane displacement field and surface strain rate components. Data presented in the form of scaled measurement for both plates indicates that both (a) temporal variations and (b) spatial variations are in very good agreement throughout the measurement period. Even for conditions where the buried explosive is quite small and the depth of burial is shallow, results clearly show that scaling of small specimen buried blast loading experiments can be applied to quantitatively predict the dynamic response of larger structures, provided that the physical process activated during the blast are similar.

# CHAPTER 3

## SMALL SCALE MODEL OF VEHICLE STRUCTURE SUBJECTED TO BLAST LOADING BY BURIED CHARGE

### 3.1 LITERATURE REVIEW

The adverse physiological consequences of vertical acceleration on humans were first observed in the early 1900s. In 1919, Head and Brown (Head 1920, Brown 1956) noticed a phenomenon known as "fainting in the air" caused by sustained airplane accelerations of 4.5 G's or higher. Similar phenomena such as blackout and grayout were also observed around the same time. Over the coming decades, these effects became attributed to cessation of blood flow in the eyes and brain (Duane 1953). Since the technology did not yet exist to apply and then accurately measure accelerations large enough to cause dramatic injuries, early research on the response of humans to vertical accelerations focused on non-life-threatening acceleration levels. In the 1950s, research began to evolve that resulted in designation of a range of acceleration thresholds that could cause severe injury and death. Investigators began to understand that rapid vertical acceleration could cause, in addition to blackout and unconsciousness, fracture of the spinal cord, and brain contact with the skull. Stoll (Stoll 1956) determined that the severity of human response to vertical acceleration depends not only on maximum acceleration, but also on the rate that acceleration is applied. Later, Eiband (Eiband 1959) published data showing the effects of acceleration on scales smaller than previously investigated. He also developed graphs illustrating the vertical acceleration tolerance thresholds of human

beings. Gurdjian and co-workers (Gurdjian 1953, 1964) first proposed the "Wayne State University Cerebral Concussion Tolerance Curve (WSTC)". Based on the curve, an important severity index was developed which is known as Head Injury Criterion (HIC). In 1969, Stech (Stech 1969) proposed another injury criterion Dynamic Response Index (DRI). The DRI is a model that assesses the physical response of the human body to upward acceleration and is based on a differential equation describing the stiffness of the spinal cord. In the following decades, a variety of other head injury criteria had been proposed and investigated (Verse 1971, Goldsmith 1979, Hutchinson 1998). The Department of Defense (DoD) and U.S. Army have developed limiting thresholds for human vertical acceleration tolerance based on the WSTC and other research studies. The DOD has suggested limiting human acceleration to 25G for 100ms (DOD 1998). The U.S. Army has suggested a limit of 23G for 25ms (US Army 1989), where G is the acceleration of gravity. The National Highway Traffic Safety Administration (NHTSA) specified the limit for HIC evaluated over a maximum time interval of 36ms for the 50th percentile male. As of 2000 (Eppinger 1999, 2000), the NHTSA final rule adopted limits that reduce the maximum time for calculating the HIC from 36ms ($HIC_{36}$) to 15ms ($HIC_{15}$). The NHTSA final rule also revised the HIC limits for different sizes of dummies. The HIC value is calculated using equation (3-1).

$$\mathrm{HIC} = max\left\{(t_2 - t_1)[\frac{1}{t_2 - t_1}\int_{t_1}^{t_2} a(t)dt]^{2.5}\right\} \qquad (3\text{-}1)$$

where a(t) is the acceleration history (expressed in G′s), and ($t_2$-$t_1$) is the time interval (expressed in s). The $HIC_{15}$ metric was used in these studies, consistent with the requirements of the National Highway Traffic Safety Administration (NHTSA). Details regarding the procedure used to compute $HIC_{15}$ will be presented in Section 3.6.2.

Regarding the investigations on buried blast loading experiments,.Nurick and Shave (Nurick 1995) experimentally studied the failure of thin edge clamped steel plates subjected to explosive loading by using a ballistic pendulum. The authors estimated the total impulse and analyzed the type of failure mode experienced by the clamped plate. Jacob et al (Jacob 2004) reported a series of experimental results and numerical predictions for clamped mild steel quadrangular plate of different thickness and varying length-to-width ratios subjected to localized blast loads of varying size. They introduced a localized loading parameter to the dimensionless damage number to simplify the complexity of interaction between charge diameter and plate geometry and compared with the results of Nurick (Nurick 1989) with good success. Later, they (Jacob 2007) studied the effect of stand-off distance and charge mass on the response of fully clamped circular mild steel plates using blast tube and indicated that blast loading is localized or uniformly distributed depending on the ratio of stand-off distance to diameter of plate. Fourney and his co-authors (Fourney 2005, 2006, 2008) performed a series of buried blast experiments to quantify the effect of parameters. In some cases, when the soil was saturated sand, there were explosive 'bubble' effects similar to those encountered in shallow water. Schleyer et. al. (Schleyer 2007) reported the response of a panel, which was based on a deep trough trapezoidal profile with welded angle connections at the top, bottom and free sides, loaded by a shock pressure pulse representative of the positive phase of the air blast loading arising from a high-explosive charge. Lawrence (Lawrence 1944) and Hargather (Hargather 2007) reported photographic studies on the mechanism of detonation in explosives and the scaling of blasts respectively. Tiwari et al. (Tiwari 2009) measured the full-field transient plate deformation of a limited specified center

area during blast loading by using 3D image correlation. In Snyman's work (Snyman 2010), he showed the similarity of the imparted impulse of different shape of charges obtained by the horizontal motion of a pendulum. Fox et. al. (Fox 2011) performed computational investigations of rigid targets with various geometries to the detonation of shallow buried explosives and compared to experiments with good agreement. It is noted that these related experimental studies primarily focused on dynamic behavior of a single unprotected plate subjected to high rates of loading.

In this chapter, small scale model experiments employing (a) passenger floorboard and external frame support with lower V-shaped hull and (b) steel frame and inverted V-shape hull with various frame connections and coatings, but without a floorboard, are designed and manufactured via input-based scaling of full sized components, respectively. The effects of various hull modifications on measured vertical acceleration are presented. In addition, $HIC_{15}$ values calculated from experimental results using Eq (3-1) are employed to assess the merits of various mitigation strategies for protecting personnel.

## 3.2 INPUT SCALING OF EXPERIMENTAL STRUCTURE CONFIGURATION

Recent studies have shown that the full specimen-explosive-structure scaling via dimensional analysis can be used to accurately predict the deformation response of appropriately scaled blast loading structures. For blast loading studies, dimensional analysis has shown that a scaling factor can be derived from the cube root of the ratio of the full size charge mass to the small scale charge mass.

Even when complete scaling of the structure is not feasible, small scale experiments are oftentimes performed using a smaller amount of explosive, and the

results used to estimate the behavior of full-scale structures. In our studies, the investigators scale the explosive weight (input scaling) and approximately scale various structural elements using a 1/3 scaling law to be nominally consistent with large-scale structures. As shown in Eq (3-2), the scaling factor β=10.102 is used in our studies unless otherwise noted, so that detonation of 1.031 kg of Pentaerythritol Tetranitrate (PETN) explosive for a full-scale vehicle corresponds to detonation of a 1g PETN explosive in these experiments (see Eq (3-2)).

$$\beta = \left(\frac{m_{full}^{explosive}}{m_{small}^{explosive}}\right)^{1/3} = \left\{\begin{array}{ll} \left(\frac{1031g}{1g}\right)^{1/3} & \text{--- } Exps\ 1\text{-}15 \\ \left(\frac{4536g}{4.4g}\right)^{1/3} & \text{--- } Exps\ 18\text{-}26 \end{array}\right\} = 10.102 \qquad (3\text{-}2)$$

For partial scaling such as performed in these studies, Eqs (3-3a), (3-3b), (3-3c) and (3-3d) are approximate relationships between time, distance (e.g., depth of burial (DoB)), velocity and acceleration, respectively.

$$\frac{t_{full}}{t_{small}} \cong 10.1\mathbf{0}2 \rightarrow \quad t_{full} \simeq 10.102\ t_{small} \qquad (3\text{-}3a)$$

$$\frac{DoB_{full}}{DoB_{small}} \cong 10.102 \rightarrow \quad DoB_{full} \simeq 10.102\ DoB_{small} \qquad (3\text{-}3b)$$

$$\frac{v(t)_{full}}{v(t)_{small}} \cong 1 \rightarrow \quad \mathbf{v}(t)_{full} \simeq \mathbf{v}(t)_{small} \qquad (3\text{-}3c)$$

$$\frac{a(t)_{full}}{a(t)_{small}} \cong \frac{1}{10.102} \rightarrow \quad a(t)_{full} \simeq \frac{a(t)_{small}}{10.102} \qquad (3\text{-}3d)$$

Thus, a 7.62mm DoB of 1 gram of PETN explosive in our small scale experiments would correspond approximately to 77mm DoB of 1.031kg of PETN explosive in full-sized structures. Details regarding the relationship between small-scale parameters and their full scale equivalents are shown in Table 3.1.

Table 3.1 Relationship between small scale and full-scale parameters for blast loading experiments.

| **Parameters** | **Small size test** | **Full size test** |
|---|---|---|
| DoB (depth of bury) | 7.62mm | 77.0mm |
| SoD (stand-off distance) | 81.0mm | 817.88mm |
| Vehicle length | 406.4mm | 4105.45mm |
| Vehicle width | 355.6mm | 3592..27mm |

## 3.3 EXPERIMENTS

Two independent sets of experiments are performed. The first set focuses on the effects of hull type/shape on the mitigation of floorboard motions and accelerations in small scale model structures emulating reduced weight aluminum vehicles; the application of interest relates to the effect of floorboard motions during blast loading on passengers in contact with floorboards in nominally aluminum structures. In these studies, 3D digital image correlation is used to measure floorboard motions, velocities and accelerations during blast loading.

A second set of experiments (Hurley 2011) focuses on frame motions and accelerations when steel frames and steel structures are employed with various frame connections and coatings for frame blast mitigation. In addition, direct comparison of measurements using 3D-DIC and accelerometers are reported in a second set of experiments (Hurley 2011), which shows that the data obtained using 3D-DIC is as accurate as the data obtained using accelerometers. Furthermore, the 3D-DIC data is obtained successfully in all cases whereas the accelerometers failed in multiple blast loading experiments.

## 3.4 MEASUREMENT OF FLOORBOARD DEFORMATIONS DURING BLAST LOADING USING STEREOVISION DIGITAL IMAGE CORRELATION

Figure 3.1 shows a schematic of the overall experimental configuration, including cameras, specimen-frame combination and sand blast facility. The setup consists of two matched Vision Research Phantom V12.1 high speed digital cameras. The cameras' optical arrangement used in the experiments has the following overall configuration;

- total pan angle between two optical axes ≈ 30 °
- distance from the lens to the center of plate ≈ 1.2m
- spacing of the calibration grid ≈ 12mm
- lens focal length ≈ 50mm; lens F stop number ≈ 8; 8 bit image intensity quantization
- cross-camera synchronization within ±1 μs using external TTL pulse
- lighting using multiple halogen lamps attached to concrete walls
- image sizes ranging from 48 x 256 pixels to 64 x 368 pixels
- inter-frame time ranging from 3.36 μs to 5.49 μs

For the magnification of interest, a high contrast random speckle pattern is placed on the specimen center area that is undergoing maximum deformation and acceleration when exposed to detonation under the central region. The specimen is lightly coated with white enamel paint and then a sharpie marker is used to manually apply a dot pattern of the appropriate size and distribution on the specimen. Once the specimen is assembled to the frame fixture, threaded spacers are affixed at the four corners of the fixture. The height of the spacers is adjusted to meet the stand-off distance (SoD) to be used in the experiment. The assembled experimental configuration is temporarily placed on the sand surface and the outer edge of the frame carefully etched into the sand surface, with the center location identified using diagonal lines. The specimen is then removed and the

explosive charge and detonator are assembled and carefully buried in the sand below the center location and at the appropriate depth of bury (DoB).

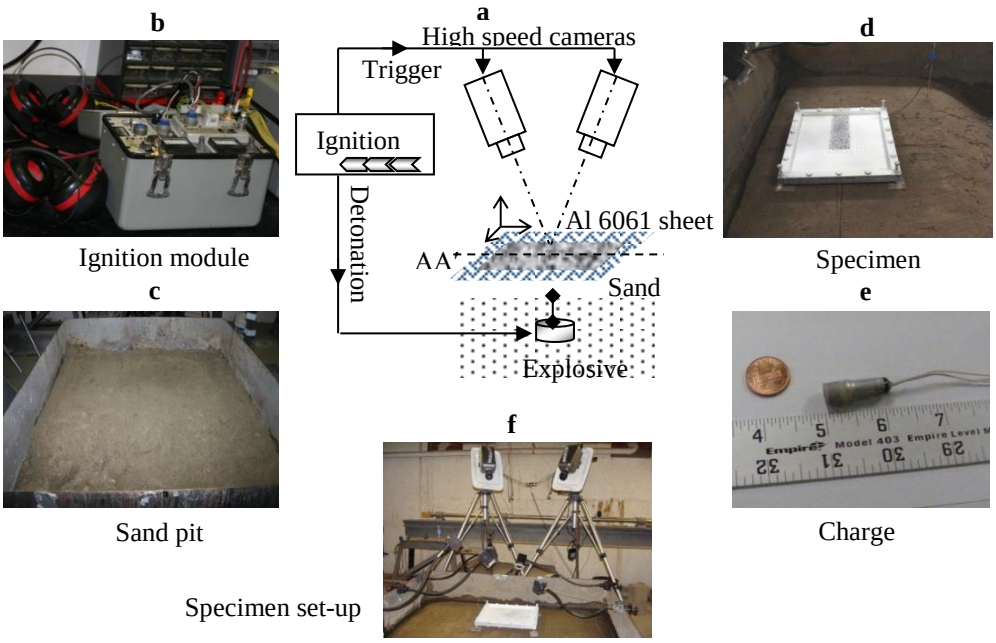


Figure 3.1 Experimental set up for buried blast loading experiments.

After the explosive is buried, the cameras are mounted on tripods and oriented to view the position where the specimen will be located. Calibration images of a grid located near the buried explosive are obtained. The calibration grid images are used to verify that a convergent calibration analysis is obtained. After calibration has been confirmed, the cameras are covered with plastic protective enclosures to mitigate impact from sand or other debris expelled during blast loading. The plastic protective enclosure is fabricated using a high quality, flat transparent and thin (<1mm) epoxy plate, with the front plate approximately orthogonal to the optical axis of the lens. In such cases, addition of the plate should not affect the calibration process and will have minimal effect on the measurements. Finally, the specimen is replaced above the buried charge and the SoD is again confirmed prior to initiating the blast loading. Once a final check is

performed, the laboratory is evacuated and two simultaneous electric pulses are sent to the detonator to initiate the explosion and simultaneously trigger both cameras to record the event.

Table 3.2 List of blast loading experiments with aluminum frames

| Exp. # | DoB | SoD to floor-board | Cha-rge* | Floorboard and Al6061 frame dimensions | Al6061 floorboard thickness | Hull | Al6061 Hull thickness | Angle of hull (degree) | Image size (pixels) | 1/FPS (μs) | Deto-nator |
|---|---|---|---|---|---|---|---|---|---|---|---|
| 1 | 7.62 | 81.0 | 1g | 355.6×406.4 | 0.51 | No hull | None | None | 256x64 | 4.34 | RP80 |
| 2 | 25.4 | 81.0 | 1g | 355.6×406.4 | 0.51 | No hull | None | None | 384x56 | 4.80 | RP80 |
| 3 | 25.4 | 81.0 | 1g | 355.6×406.4 | 0.51 | Single hull | 2.29 | 13/154/13 | 512x48 | 5.07 | RP80 |
| 4 | 12.7 | 81.0 | 1g | 355.6×406.4 | 0.51 | Single hull | 2.29 | 13/154/13 | 512x48 | 5.07 | RP80 |
| 5 | 7.62 | 81.0 | 1g | 355.6×406.4 | 0.51 | Single hull | 2.29 | 13/154/13 | 368x64 | 5.49 | RP80 |
| 5R* | 7.62 | 81.0 | 1g | 355.6×406.4 | 0.51 | Single hull | 2.29 | 13/154/13 | 368x64 | 5.49 | RP80 |
| 6 | 7.62 | 81.0 | 1g | 355.6×406.4 | 0.51 | Foam and single hull | 2.29 | 13/154/13 | 512x48 | 5.07 | RP80 |
| 7 | 7.62 | 81.0 | 1g | 355.6×406.4 | 0.51 | Double hull | 2.29 | 13/154/13 | 400x48 | 5.13 | RP80 |
| 8 | 7.62 | 81.0 | 1g | 355.6×406.4 | 0.51 | Cantilevered single hull | 2.29 | 13/154/13 | 384x56 | 4.80 | RP80 |
| 9 | 7.62 | 81.0 | 1g | 355.6×406.4 | 0.51 | Cantilevered single corrugated hull | 2.29 | 13/154/13 40/100/40 | 256x48 | 3.36 | RP80 |
| 10 | 25.4 | 81.0 | 1g | 355.6×406.4 | 0.51 | Corrugated hull | 2.29 | 13/154/13 40/100/40 | 384x48 | 4.23 | RP80 |
| 11 | 7.62 | 81.0 | 1g | 355.6×406.4 | 0.51 | Corrugated hull | 2.29 | 13/154/13 40/100/40 | 384x48 | 4.23 | RP80 |
| 12 | 7.62 | 81.0 | 1g | 355.6×406.4 | 1.60 | Corrugated hull | 2.29 | 13/154/13 40/100/40 | 256x48 | 3.36 | RP80 |
| 13 | 7.62 | 81.0 | 1g | 355.6×406.4 | 1.60 | No hull | None | None | 384x56 | 4.80 | RP80 |
| 14 | 7.62 | 31.0 | 1g | 355.6×406.4 | 1.60 | No hull | None | None | 384x56 | 4.80 | RP80 |
| 14R* | 7.62 | 31.0 | 1g | 355.6×406.4 | 1.60 | No hull | None | None | 384x56 | 4.80 | RP80 |
| 15 | 25.4 | 31.0 | 1g | 355.6×406.4 | 1.60 | No hull | None | None | 384x48 | 4.23 | RP80 |

Charge* ---mass of PETN charge; all unit in mm unless specified; R* ---repeated experiment.
FPS---Frame per second. Since camera resolution is a function of frame rate, the frame rate used in each experiment was changed slightly for high-speed Phantom cameras to maintain approximately the same number of pixels/mm for the as-applied speckle pattern. Since these slight changes in frame rate give essentially the same pixels/mm for the speckle pattern, when using the same subset size this approach maintains similar 3D-DIC accuracy for all experiments.

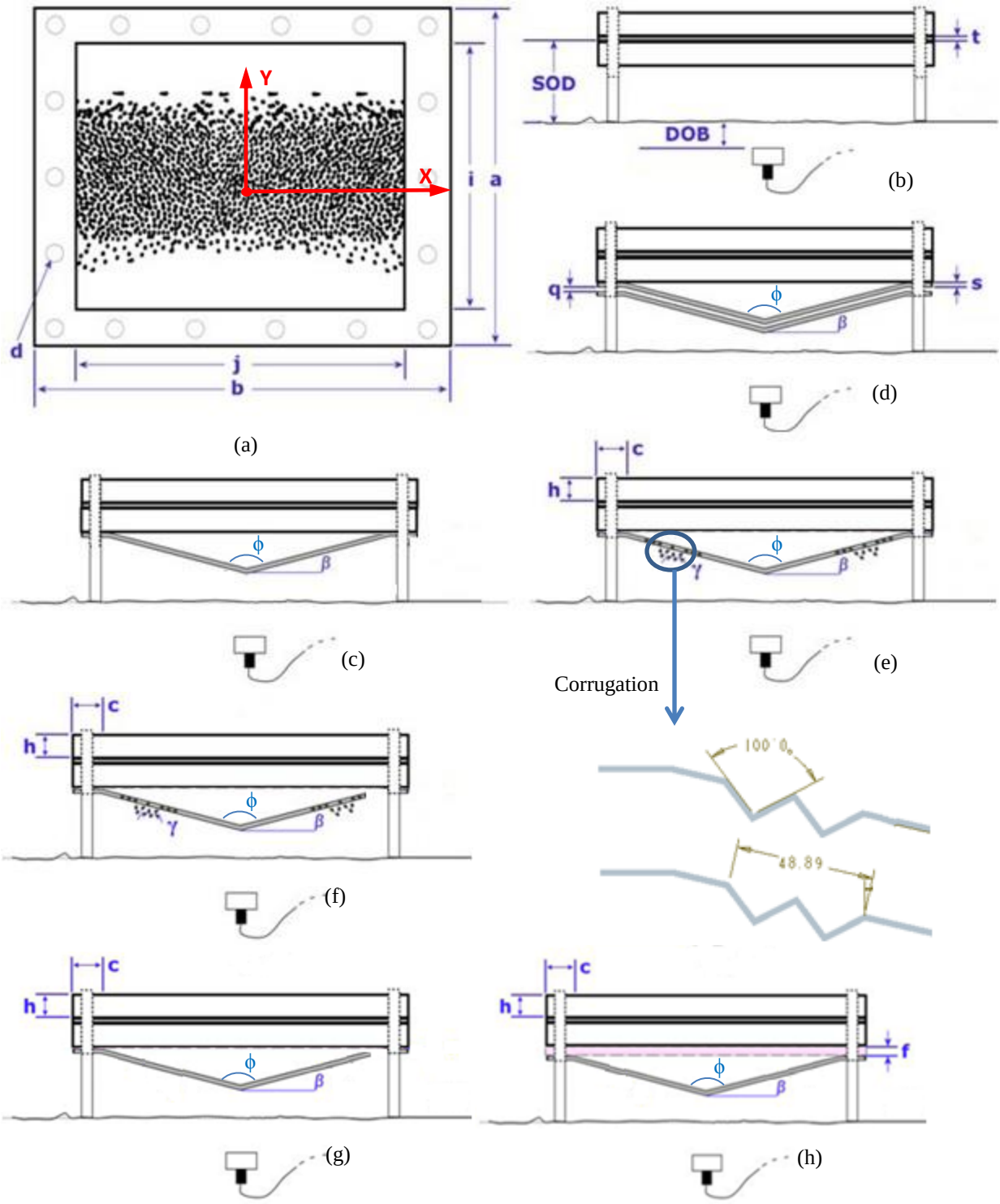


Figure 3.2 Specimen and frame configurations with and without hulls: (a) floorboard alone; (b) no hull; (c) single hull; (d) double hull; (e) corrugated hull; (f) cantilevered single corrugated hull; (g) cantilevered single hull; (h) frame foam padding with single hull. In figure: d=9.53, b=406.4, j=355.6, i=304.8, a=355.6, t=0.51, h=12.7, c=25.4, q=4.57, f=8.89, s=2.29, γ=100 °, β=13 °. Φ=154 °(all unit in mm unless specified).

### 3.5 FLOORBOARD MEASUREMENTS IN ALUMINUM FRAME-HULL STRUCTURES

The aluminum alloy Al6061-T6 is used to manufacture the floorboards, frame and hulls for all experiments. Details for all experiments are given in Table 3.2. Figure 3.2 shows a top view (Fig 3.2(a)), side view of specimen-frame structure without a hull (Fig. 3.2(b)) and several side views (Figs. 3.2(c)~(h)) of all the V-shaped hulls used in the first set of experiments listed in Table 3.2. The specimen and hulls are bolted onto an aluminum frame that consists of two geometrically identical parts; upper clamping member and lower frame. The lower rectangular frame has outer dimensions of 355.6mm × 406.4mm × 12.7mm, and an inner cutout opening with dimensions 304.8mm × 355.6mm. The rectangular shape for the lower frame and clamping member are constructed using pieces from a 25.4mm × 12.7mm aluminum bar stock welded at the corners. Each half of the frame is machined with 18 - 9.525mm diameter matching holes. The specimen has a similar set of 18 holes and is bolted between the two frames using 9.525mm diameter stainless steel bolts, lock washers and stainless steel nuts.

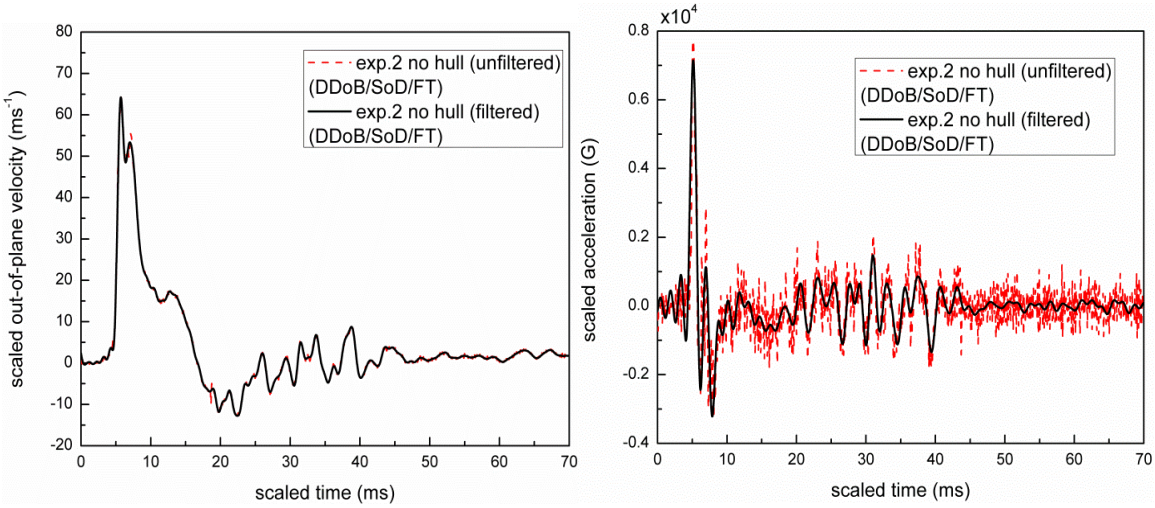


Figure 3.3 Left: un-filtered and filtered out-of-plane velocity; right: unfiltered and filtered acceleration data for floorboard center.(DDoB-25.4mm, SoD-81mm, FT-0.51mm floorboard).

### 3.5.1 VELOCITY AND ACCELERATION DETERMINATIONS OF FLOORBOARD

For all standard hulls with frames and floorboards (see Table 3.2), the out-of-plane displacement, $U_z$, which is in the Z direction (coordinate system shown in Figure 3.2(a)), of the center-point location (0,0,0) in each floorboard is measured using 3D digital image correlation; all three displacement components are measured, but only $U_z$ is used in this study[3]. Out-of-plane velocity and acceleration results at the center-point are obtained by differentiating the out-of-plane displacement $U_z$ time history in the following way. First, a time series of data for $U_z(x,y,0,t)$ is obtained at every time interval; the component $U_z$ will be used in the following discussion. Second, using this time sequence for $U_z$, a "moving window least squares quadratic fit" is performed in time to seven consecutive data points, beginning with the data at time $t_o$. Third, the quadratic fit is differentiated (a) once to obtain the velocity at the midpoint of the time span and (b) twice to obtain the acceleration at the midpoint of the time span. This process is repeated by moving forward in time $\Delta t$ and selecting seven consecutive points starting at time $t_o + \Delta t$, continuing until the entire velocity and acceleration history is obtained for a point on the plate. Then, velocity $\partial U_z/\partial t(t)$ and acceleration $\partial^2 U_z/\partial t^2(t)$ time histories, are filtered using an FFT with a Butterworth low pass filter having a 10 kHz cutoff frequency to remove high frequency, low amplitude oscillations that occur later in the time period. Direct comparisons of filtered data and unfiltered data for both velocity and acceleration data are shown in Figure 3.3, confirming that the filtering process does not have an appreciable effect on the velocity and acceleration results.

[3] Review of video data indicates that each plate-frame structure moves upward rigidly, with minimal rotation, during the first 36ms after initial detonation. This is true for all experiments performed in this study.

### 3.5.2 HULL SYSTEMS

The weight of Army Ground Combat Vehicle keeps growing due to increased threats to passengers from blast events and more lethal weapon systems. The current total weight of ground vehicles can exceeds 70 tons contributed by armor protection employed to mitigate blast effects, at the cost of reduced mobility and speed, increased fuel consumption and decreased transportability. Concern regarding these issues has resulted in DoD mandates to decrease weight while maintaining reasonable levels of protection and cost. Protective hulls remain an important contributor to overall vehicle safety, while adding a minimum of weight to the structure. As shown in Figure 3.2 and Table 3.2, four types of small scale hull designs are evaluated experimentally. In one experiment, rigid foam was also employed. Details for each design are provided in the following sections.

#### 3.5.2.1 SINGLE HULL

The standard single hull is shown in Figure 3.2(c). The optimum bending angle (measured along an axis parallel to the floorboard and along the long side of the frame) for each side of the hull is between 13 ºand 20 º(Genson 2006, Benedetti 2008, Fourney 2010). Though delivering similar amounts of transmitted impulse, a 13 ºangle is preferred to maximize clearance distance between the floorboard and the ground.

In these studies, each hull is shaped with a $13^{o}$ bend on each side, culminating in a total angle of $26^{o}$ and a 154 ºV shape, returning symmetrically back to the original height for the opposing 13 º bend. For the standard case hull, the original sheet is cut to dimensions of 368.3mm × 406.4mm. The width reduces to 355.6mm after introducing the hull bends.

#### 3.5.2.2 DOUBLE HULL

The double hull is shown in Figure 3.2(d). The double hull is constructed from two standard single hulls combined in one experiment. The process for creating them is exactly the same. However, the double hull specimens are mounted differently on the specimen. Larger bolts are required to pass through the extra material. The larger bolts and the extra hull increased the overall weight of the structure. Furthermore, a 4.57mm spacer is placed between each hull on both sides of the specimen to ensure the floorboard and lower hull do not interfere during the early stages of the blast. Interference between the two hulls will transfer load across the contact region, altering the behavior of the double hull system.

#### 3.5.2.3 CORRUGATED HULL

The corrugated single hull design is shown schematically in Figure 3.2(e). The corrugated hull is considered as a simple approach for increasing flexibility and energy absorption, reducing transmission of energy into the frame and floorboard. The corrugated hull has the same dimensions as the standard single hull, with the exception of the introduction of the corrugation at a distance 87.12mm (3.43 in) from the center of the hull. The initial flat plate has a size of 393.7mm × 406.4mm. An additional 38.1mm is needed due to the shaping of the hull, with 25.4mm specifically for corrugation.

#### 3.5.2.4 CANTILEVER HULL

Figures 3.2(f) and 3.2(g) show the geometry of the cantilevered and corrugated hulls, respectively. In each case, the hull is attached along one side, unrestrained on the other side, and has an initial clearance of 12.7mm on the unrestrained side.

#### 3.5.2.5 RIGID FOAM AND SINGLE HULL

A specific experiment focused on the effect of rigid foam padding between the frame and a single V-shaped hull is performed. In these studies, a foam thickness of 8.89mm is used. The foam padding and single hull, shown in Figure 3.2(h), has a bolted connection through the hull, frame and floorboard. The foam padding and frame widths are the same.

## 3.6 EXPERIMENTAL RESULTS

Unless otherwise note, the measured time, displacement, velocity and acceleration measurements are "input-scaled" according to Eqs (3-2a~3-2d) so that the presentation will correspond approximately to the expected full-scale results for similar structures with 1.031 kg of PETN explosive.

To demonstrate the consistency of the blast loading methodology with 3D digital image correlation measurements, experiment 5 in Table 3.2 is repeated using the same DoB, SoD, charge mass, aluminum frame, hull and floorboard dimensions and image resolution. The measured center point displacement data on the floorboard for both experiments are compared in Figure 3.4. As shown in Figure 3.4, the peak in displacement occurred ≈ 2ms after detonation in both cases while a minimum in displacement occurred ≈ 3.5ms after detonation in both cases. Figure 3.5 compares the residual deformation of the floorboard along the plate center line at y=0 for both specimens measured by 3D digital image correlation. As shown in Figure 3.4, the measurements have maximum and minimum values at nearly the same time and show nearly identical trends for all other points. Taken together, the data shown in Figures 3.4 and 3.5 appears sufficiently similar in a dynamic and difficult-to-control environment to demonstrate repeatability of the experiments and consistency in the stereovision

measurements.

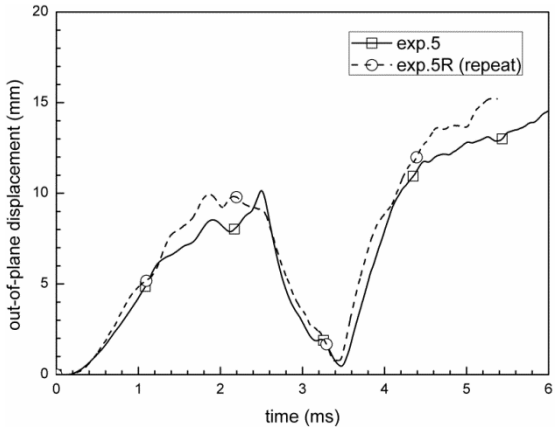


Figure 3.4 Un-scaled out-of-plane displacements at approximate floorboard center location.

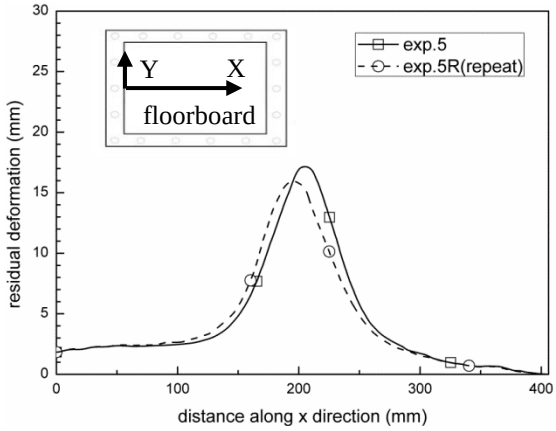


Figure 3.5 Un-scaled residual shapes along X direction.

### 3.6.1 OUT-OF-PLANE MOTIONS OF FLOORBOARD CENTER

Input-scaled displacement histories for typical floorboard center-point out-of-plane displacements in Experiments 1, 2, 3, 5, 8, 10 and 13 are shown in Figure 3.6. Results for the remaining experiments are given in Appendix A.

The procedure described in Section 2.5.1 is used to determine the input-scaled acceleration histories for the floorboard center location, with and without various protective hulls. Maximum input-scaled vertical acceleration results during the first 15ms

are presented in Figure 3.7. The complete input-scaled acceleration histories of the floorboard center location are given in Appendix B. The input-scaled peak values for the out-of-plane displacement, acceleration and $HIC_{15}$ at the floorboard center are showed in Figures 3.6, 3.7 and 3.8 and summarized in Table 3.4.

Table 3.3 Input-scaled peak values of out-of-plane displacement, acceleration and $HIC_{15}$ at floorboard center for blast loading experiments

| **Exp. #** | **1** | **2** | **3** | **4** | **5** | **6** | **7** | **8** | **9** |
|---|---|---|---|---|---|---|---|---|---|
| **Out-of-plane displacement (mm)** | 414.885 | 291.765 | 107.417 | 96.488 | 102.436 | 91.669 | 76.765 | 71.959 | 94.766 |
| **Acceleration ($G\times10^4$)** | 2.149 | 0.692 | 0.079 | 0.111 | 0.117 | 0.114 | 0.075 | 0.073 | 0.046 |
| **$HIC_{15}$ ($G^{2.5}S\times10^5$)** | 61.442 | 4.823 | 0.226 | 0.509 | 3.147 | 0.612 | 0.742 | 0.445 | 0.479 |
| **Exp. #** | **10** | **11** | **12** | **13** | **14** | **15** | | | |
| **Out-of-plane displacement (mm)** | 88.876 | 100.925 | 37.584 | 210.598 | 330.825 | 252.946 | | | |
| **Acceleration ($G\times10^4$)** | 0.171 | 0.517 | 0.065 | 1.255 | 4.073 | 1.160 | | | |
| **$HIC_{15}$ ($G^{2.5}S\times10^5$)** | 0.431 | 3.573 | 0.050 | 16.204 | 55.167 | 9.632 | | | |

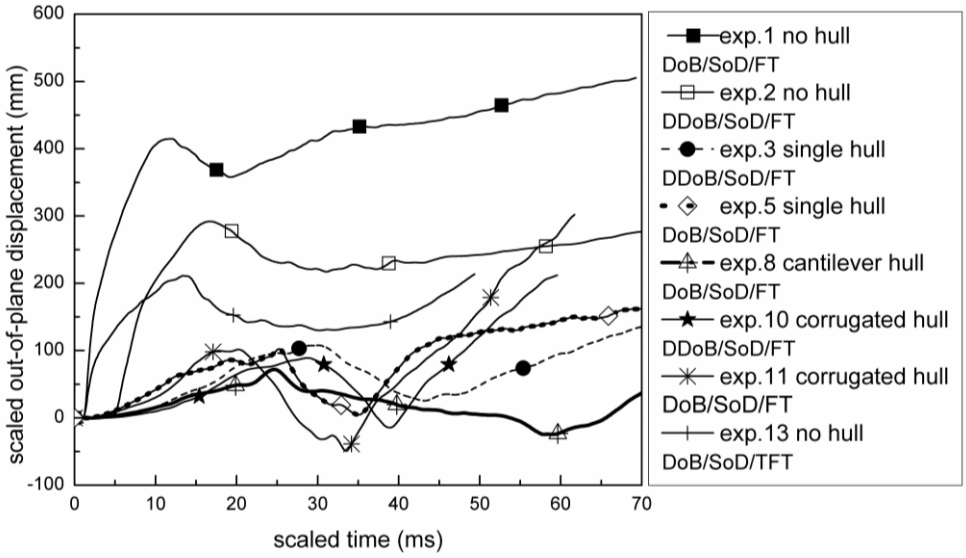


Figure 3.6 Input-scaled out-of-plane displacement histories of experiments 1, 2, 3, 5, 8, 10, 11 and 13 (top), and peak value of out-of-plane displacements of all experiments at floorboard center location (bottom). (NH-no hull, SH-single hull, FSH-foam & single hull, DH-double hull, CH-cantilever hull, CCH-cantilever single corrugated hull, CH′-corrugated hull, DoB-7.62mm, MDoB-12.7mm, DDoB-25.4mm, SoD-81mm, SSoD-31mm, FT-0.51mm floorboard, TFT-1.60mm floorboard).

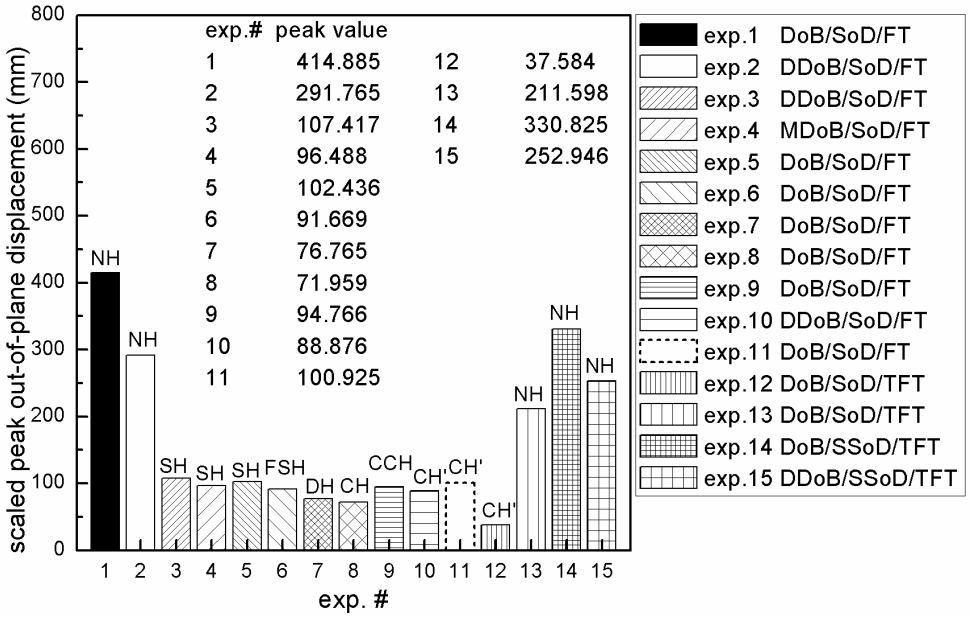


Figure 3.6 Input-scaled out-of-plane displacement histories of experiments 1, 2, 3, 5, 8, 10, 11 and 13 (top), and peak value of out-of-plane displacements of all experiments at floorboard center location (bottom). (NH-no hull, SH-single hull, FSH-foam & single hull, DH-double hull, CH-cantilever hull, CCH-cantilever single corrugated hull, CH′-corrugated hull, DoB-7.62mm, MDoB-12.7mm, DDoB-25.4mm, SoD-81mm, SSoD-31mm, FT-0.51mm floorboard, TFT-1.60mm floorboard) (cont′d).

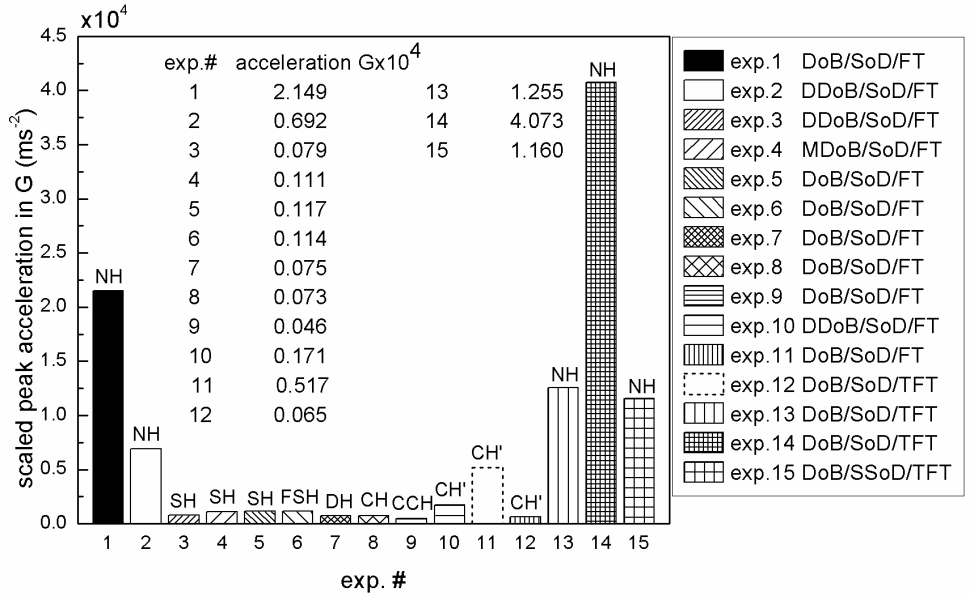


Figure 3.7 Input-scaled peak out-of-plane acceleration prior to peak negative acceleration of experiments 1 to 15 at approximate floorboard center location. (NH-no hull, SH-single hull, FSH-foam & single hull, DH-double hull, CH-cantilever hull, CCH-cantilever single corrugated hull, CH′-corrugated hull, DoB-7.62mm, MDoB-12.7mm, DDoB-25.4mm, SoD-81mm, SSoD-31mm, FT-0.51mm floorboard, TFT-1.60mm floorboard).

### 3.6.2 $HIC_{15}$ MEASUREMENTS

The procedure to obtain $HIC_{15}$ values using Eq (3-1) is given in Appendix C. Figure 3.8 shows the input-scaled maximum $HIC_{15}$ values. In addition, Appendix C presents the complete time history of input-scaled $HIC_{15}$, providing information regarding the time frame where the maximum $HIC_{15}$ occurs.

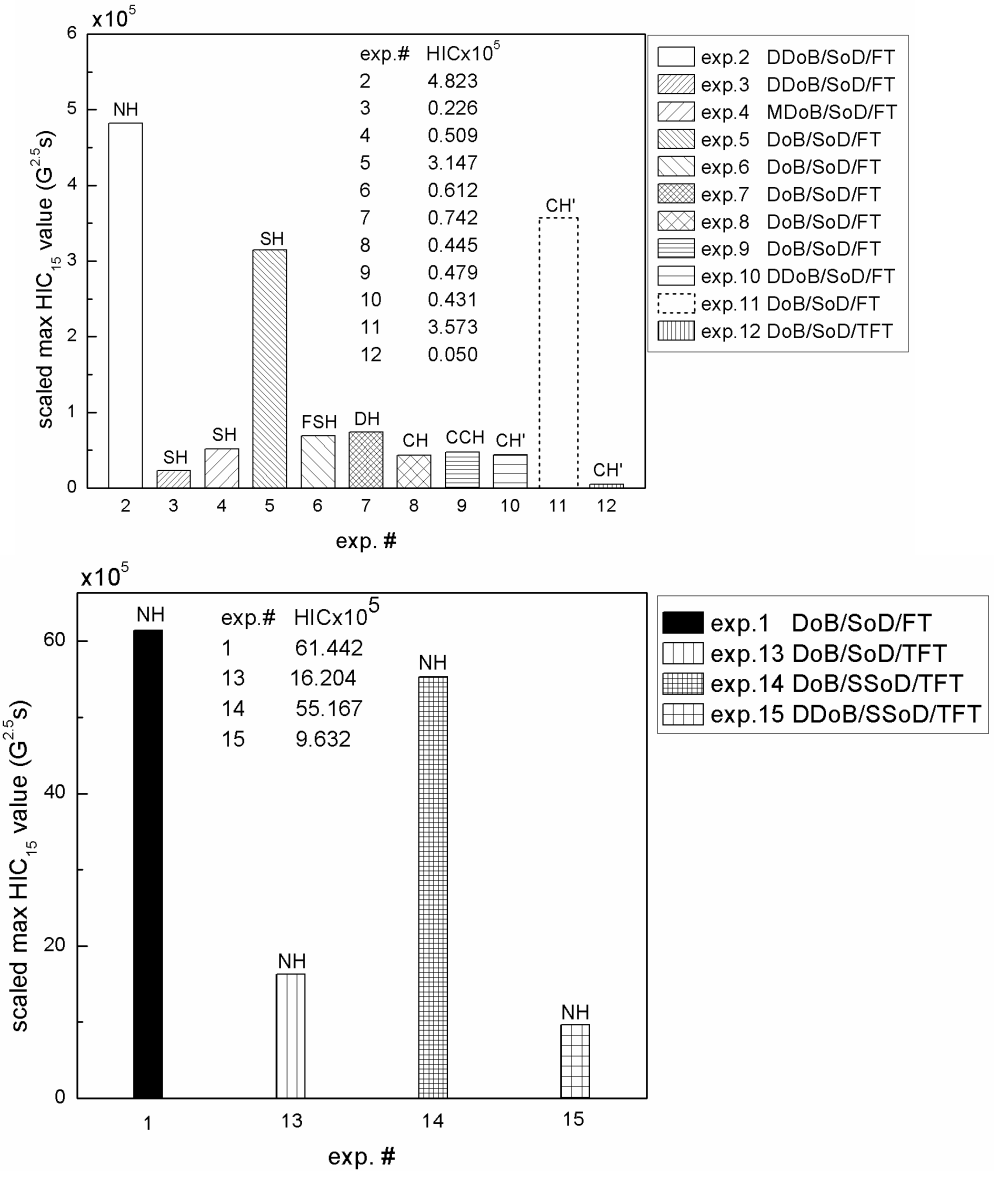


Figure 3.8 Input-scaled maximum $HIC_{15}$ value of experiments 1-15. (NH-no hull, SH-single hull, FSH-foam & single hull, DH-double hull, CH-cantilever hull, CCH-cantilever single corrugated hull, CH′-corrugated hull, DoB-7.62mm, MDoB-12.7mm, DDoB-25.4mm, SoD-81mm, SSoD-31mm, FT-0.51mm floorboard, TFT-1.60mm floorboard).

### 3.6.3 CHARACTERISTICS OF A BURIED SAND BLAST EVENT

Figure 3.9 shows the evolution of failure in an unprotected floorboard after detonation of a 5g buried explosive. Figure 3.10 show the back side of (a) a single V-shaped hull and (b) an unprotected floorboard after being subjected to a smaller blast event due to detonation of 1g of explosive. Figure 3.11 shows a side-view of the ejected sand as it interacts with a single V-shaped hull, with the separation and channeling effect of the hull clearly evident. The displacement and acceleration histories of the floorboard at locations (X=0, Y=0), (X=513.2mm, Y=0) and (X=769.8mm, Y=0) are shown (a) in Figure 3.12 for an unprotected floorboard, (b) in Figure 3.13 when using a standard V-shaped hull and (c) in Figure 3.14 when using a cantilevered corrugated V-shaped hull.

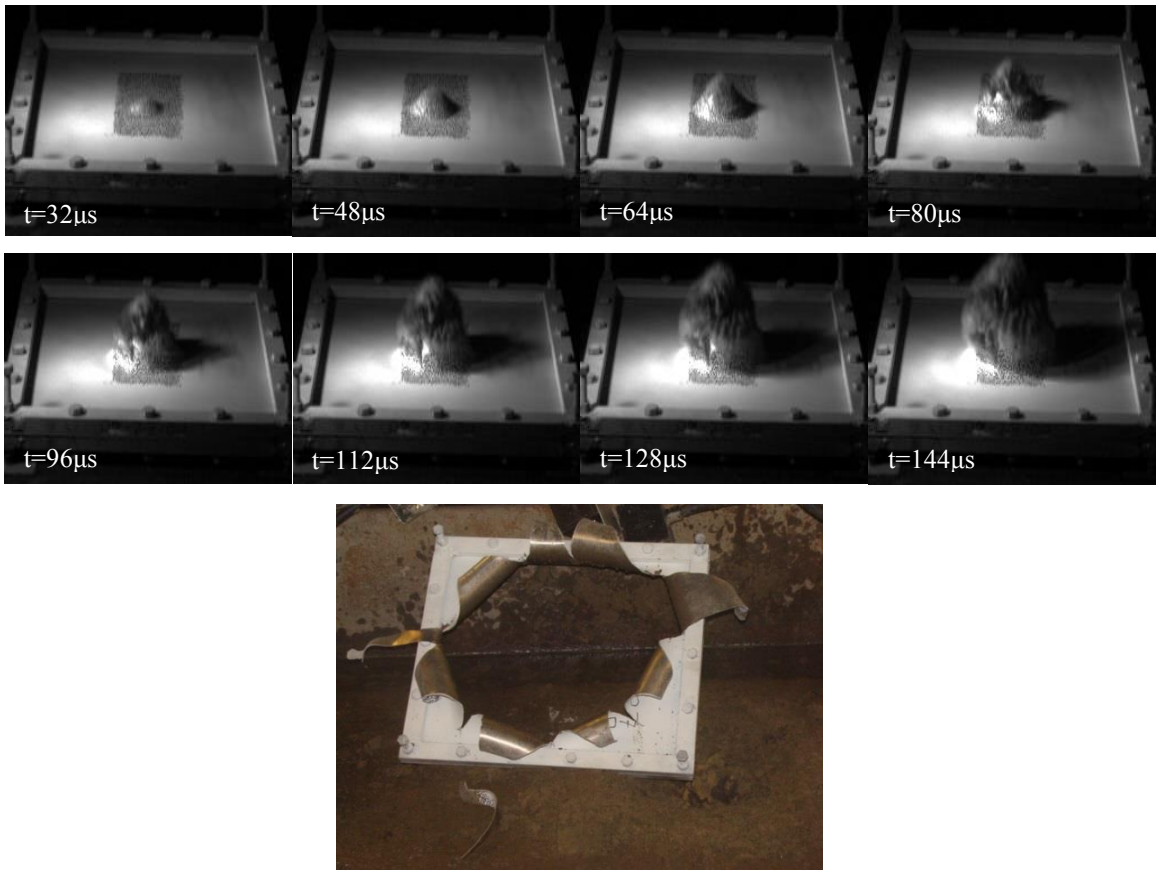


Figure 3.9 Evolution of floorboard rupture with no hull (depth of burial-7.62mm, stand-off distance-31mm, and explosive 5g).

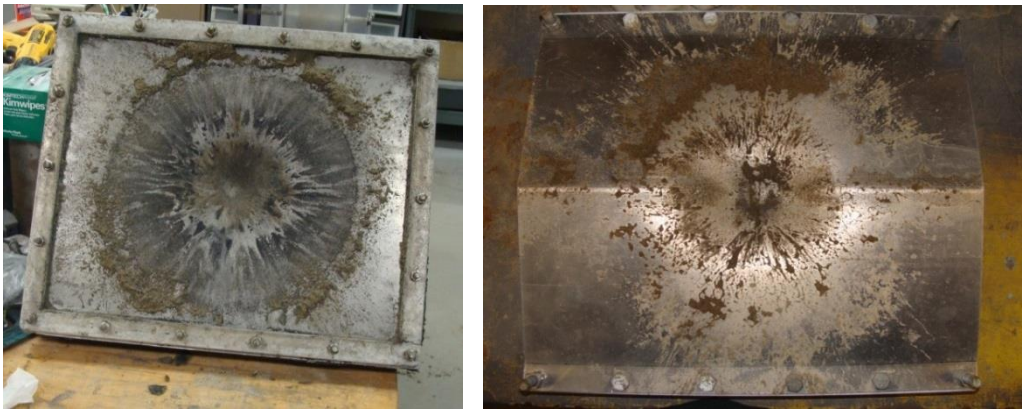

(a) (b)

Figure 3.10 Photographs of (a) back side of floorboard without protective hull after sand blast event and (b) bottom of V-shaped protective hull after sand blast event. (depth of burial-7.62mm, stand-off distance-81mm, PETN explosive 1g).

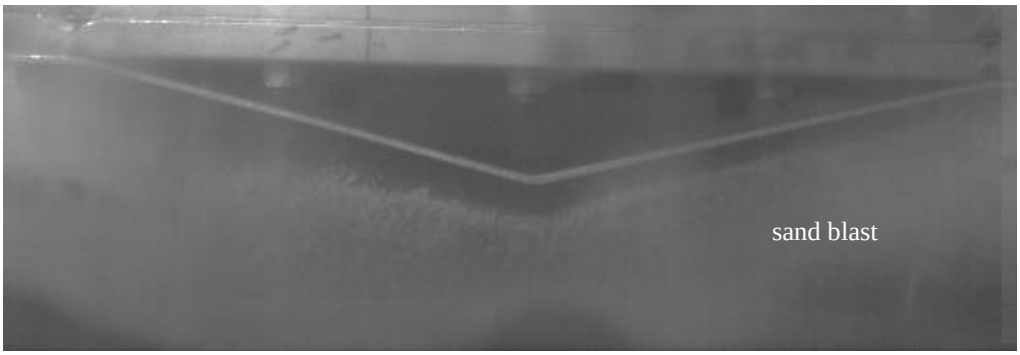


Figure 3.11 Side view of ejected sand interacting with V-shaped hull during blast event.

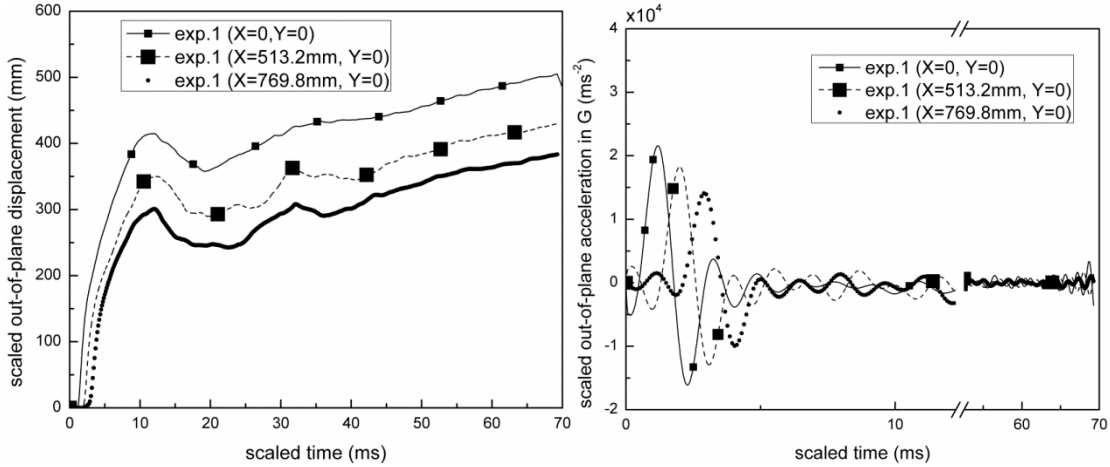


Figure 3.12 Input-scaled out-of-plane displacements and accelerations at three different locations on unprotected floorboard identified in experiment 1.

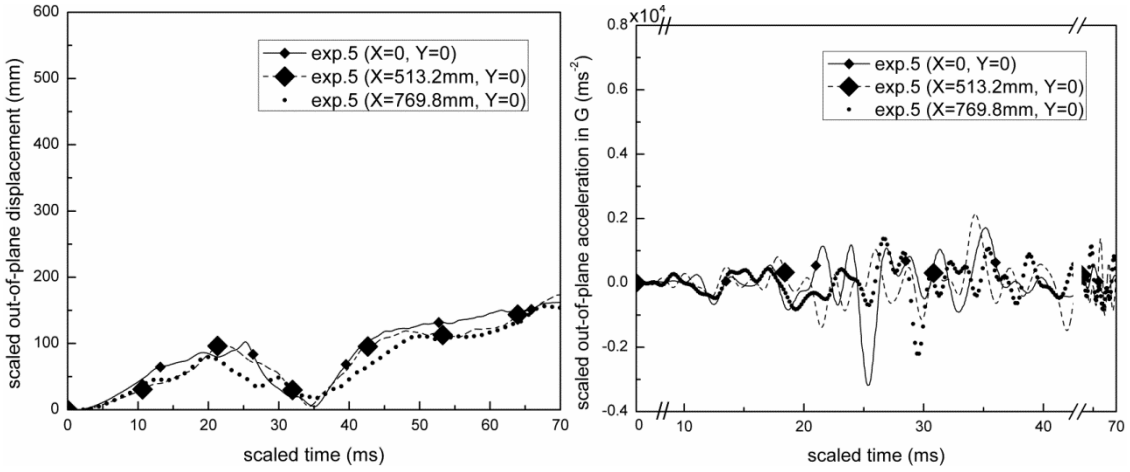


Figure 3.13 Input-scaled out-of-plane displacements and accelerations at three different locations on floorboard protected by standard V-shaped hull identified in experiment 5.

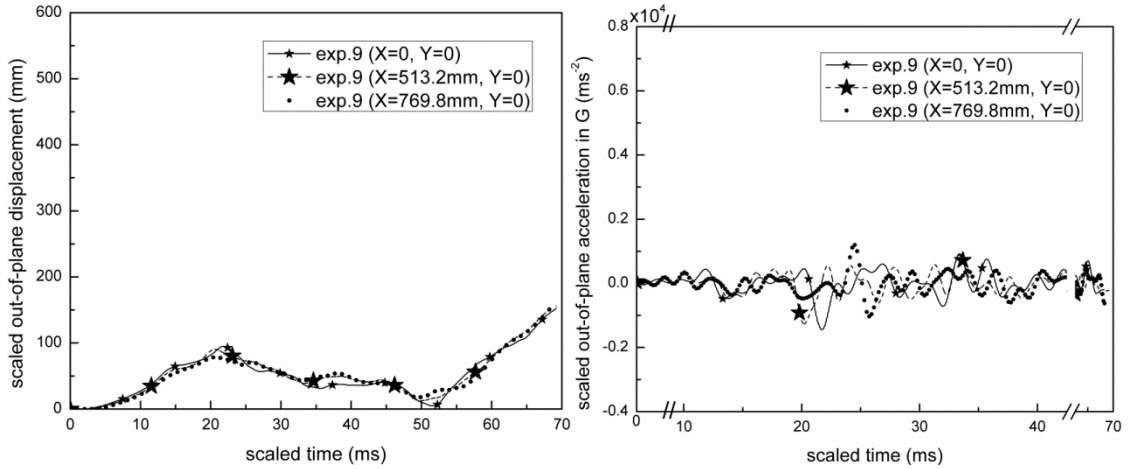


Figure 3.14 Input-scaled out-of-plane displacements and accelerations at three different locations on floorboard protected by cantilevered corrugated hull identified in experiment 9.

## 3.7 DISCUSSIONS

When employing various types of protective hulls, Figure 3.6 and Table 3.5 show that the deflection of the floorboard center-point is reduced by 6X relative to the no hull case for the same thickness of floorboard.

With regard to the results shown in Figure 3.4, there are several points to be discussed. First, the blast loading process involves the entire hull-frame-floorboard

structure, with different time scales relevant to the measured floorboard response. The actual blast loading process occurs on the time scale of microseconds, and the early time scale response of the floorboard is indicative of the localized response due to the blast process. Second, the longer time response which occurs on the scale of a few milliseconds is consistent with the complexity that arises when overall structural response ensues. Uploaded video evidence from side and top cameras shows the following: (a) Downward bending of the short side of the frame and upward bending of the long side of the frame occurs during first 2.2ms as the central region of the plate reaches a maximum upward out-of-plane displacement and the entire structure begins to lift off from the sand; (b) the structure deformations change to upward bending of the short side and downward bending of the long side from 2.2ms to 3.4ms, resulting in large downward motion of the attached floorboard even as the entire structure moves upwards; it is believed that the sudden change in structural deformation is due in part to collapse of an air bubble generated during the buried blast loading process, resulting in very low pressure conditions below the hull; (c) Reverse elastic bending again occurs in the frame members, though with reduced amplitude, from 2.2ms to 3.4ms with the floorboard center moving upwards. During this time, a variety of small waves are clearly visible on the floorboard surface as oscillations and free vibrations continue.

It is noted that some displacement results shown in Figure 3.6 have similar trends to those shown in Figure 3.4. In addition, as shown in Figure 3.6, the hull extends the period of time before the maximum in deflection occurs. This results in lower amplitudes for the floorboard acceleration and also delays the time for the peak value of acceleration. As shown in (a) Figure 3.7 and (b) results for experiments 1-11 in Appendix A-3, hulls

significantly reduce the measured center-point floorboard acceleration; the maximum acceleration is reduced by up to 47X. For a 0.51mm thick aluminum floorboard, the magnitude of maximum floorboard acceleration range from 21,490G (exp.1 no hull) to 460G (exp.9 cantilevered single corrugated hull). Though the relatively high acceleration magnitudes are well above the DoD limiting value (25G), they occur over a time period that is much less than the duration assumed to be necessary for biological damage (15ms).

When simply using thicker floorboards without protective hulls, acceleration results in Figure 3.7 show that increasing floor thickness does reduce accelerations but is not as effective as V-shaped hulls. Specifically, a thickness increase of 312.5% results in (a) a 1.7X reduction in acceleration when comparing experiment 13 to experiment 1 and (b) a 7.9X reduction in acceleration when comparing experiment 12 to experiment 11. However, as shown in Figure 3.7, for experiment 12, the use of a corrugated hull with a thick floorboard results in a 20X reduction in acceleration relative to experiment 13, confirming that hull protection is a much more effective mitigator for a range of floorboard thicknesses.

In addition to the use of acceleration to assess blast severity, the Head Injury Criterion is calculated for different hull & floorboard or frame combinations using Eq (3-1) and the procedure given in Appendix C. Though $HIC_{15}$ does not specifically determine when a head injury would or would not have occurred in a victim, the metric does act as a guide to determine when head injury is most likely to have happened. By using consistent test and calculation methods, $HIC_{15}$ values across multiple experiments can be compared to determine which conditions would be less likely to result in injuries. As shown in

Figure 3.8, for no-hull cases with floorboard thickness of 0.51mm, the $HIC_{15}$ values for the floorboard center-point range from 0.5-6 × $10^6$ $G^{2.5}$s. These measured values are orders of magnitude larger than any current standard for minimizing head injury likelihood (e.g. DoD limit is 250 $G^{2.5}$s, NHTSA limit is 700 $G^{2.5}$s), suggesting that floorboard protection without hulls is insufficient to minimize passenger injury.

Regarding the Head Injury Criterion, the time period ($t_2$-$t_1$) when acceleration occurs is considered in the HIC equation. The HIC value is used to estimate the maximum for the integrated or "average quantity" that humans can tolerate, although peak values exceed this "average" value. Conceptually, the HIC implies that even large accelerations may be "safe" as long as it occurs for a very short time. Conversely, even if the peak acceleration is not very large, it may be considered hazardous to health if it lasts for a longer time. Therefore, although the peak acceleration for experiment 9 is less than that measured for experiment 8, the time period of peak acceleration in experiment 9 extends for a longer time than that in experiment 8, resulting in a slightly larger HIC value. The difference is due to corrugation on the hull which increases the time over which the blast loading effects are transferred to the structure and the floorboard.

Since an important input variable for transmission of impulse to the hull-frame-floorboard structure is DoB, a direct comparison of the results for (a) experiments 5-9 with a constant DoB=7.62mm and floorboard thickness t=0.51mm and (b) experiments 12-14 with a constant DoB=7.62mm and different floorboard thickness t = 1.6mm, are relevant. By comparing results from experiments 6-9 to results from experiment 5, the data indicates that additional flexibility in the hull-frame connection via use of (a) foam or a spacer between the two single hulls or (b) removal of connections along one side

reduces HIC by 4-7X. For experiments 12-14, results show that increasing floorboard thickness does decrease HIC, especially when combined with increased flexibility in the protective hull via corrugation of the hull. However, in practice this solution is unlikely to be viable due to the increased weight of the vehicle when using thicker floorboard structures.

For the same structure, the effects of DoB or SoD on HIC value are investigated by comparison of (a) experiments 3, 4 and 5 which have different DoB for the same SoD=81mm and the same floorboard thickness t=0.51mm, (b) experiments 14 and 15 which have different DoB for the same SoD=31mm and floorboard thickness t=1.6mm and (c) experiments 13 and 14 which have different SoD for the same DoB=7.62mm and floorboard thickness t=1.6mm. For the effect of DoB, experiments 3-5 and experiments 14-15 show that $HIC_{15}$ is reduced by 14X and 6X, respectively, from shallow buried explosives (DoB=7.62mm) to deep buried explosives (DoB=25.4mm). For the SoD effect, experiments 13-14 indicate that the maximum $HIC_{15}$ value increases a little more than 3X from high stand-off distance (SoD=81mm) to low stand-off distance (SoD=31mm). Though it is conceptually feasible to increase the SoD to increase passenger safety, there are practical limits for SoD in real vehicles due to clearance requirements in the field.

As shown in Figures 3.9 and 3.10, detonation of a lightly buried explosive result in contained damage on both unprotected floorboard and also a protective hull. The contained area of impact on the floorboard is also evident in the data shown in Figure 3.12. Here, the amplitude of out-of-plane displacement and acceleration are reduced at locations which are further away from the floorboard center.

However, when a protective hull is employed, as shown in Figure 3.11, the sand blast loading impacts the hull with load transfer distributed more broadly to the upper structure and the floorboard. The mitigating effect of a hull is shown clearly in Figure 3.13 and 3.14 where the amplitude of displacement and acceleration at different locations are relatively close to each other. Taken together, these results confirm that protective hulls distribute loading more broadly to the structure and the floorboard, thereby minimizing localization of damage to the floorboard. However, no matter whether there is a hull or not hull, the central region in floorboard remains the most affected, experiencing peaks in acceleration before rebound of floorboard that are quite high and sufficiently large so that serious or fatal injury may occur if occupants stand or walk within this area.

An overall review of the effect of hull effectiveness indicates that various protective mechanisms will reduce $HIC_{15}$ measured on the floorboard by up to 128X. Even so, the minimum $HIC_{15}^{max} \approx 20 \times 10^3$ $G^{2.5}s$ (DoB = 25.4mm), which is nearly 2 orders of magnitude larger than the DoD limit. Based on this data, it is clear that efforts to mitigate standard floorboard accelerations to acceptable levels for human occupants will be difficult. A more appropriate design scenario would be to consider situations where the occupant is attached to the external frame and to determine whether such situations may provide a more survivable situation.

### 3.8 AN ALTERNATIVE STRUCTURE TO INCREASE SURVIVABILITY OF PASSENGER

With regard to the use of frame-mounted passenger seating to reduce the potential for injury, it is noted that most vehicles use steel structural frames. To obtain preliminary data and assess the effect of changing to a steel frame, the authors performed two buried

explosive loading experiments (SoD=31mm, DoB=7.62mm and DoB=25.4mm, 1gram PETN explosive) when using a steel frame.

Table 3.4 List of blast loading experiments with steel frames

| Exp. # | DoB | SoD to floorboard | Charge* | Floorboard and Steel frame dimensions | Al6061 Floorboard thickness | Hull | Al6061 Hull thickness | Angle of hull (degree) | Image size (pixels) | 1/FPS (μs) | Detonator |
|---|---|---|---|---|---|---|---|---|---|---|---|
| 16 | 7.62 | 31.0 | 1g | 355.6×406.4 | 1.60 | No hull | None | None | 128x128 | 5.07 | RP80 |
| 17 | 25.4 | 31.0 | 1g | 355.6×406.4 | 1.60 | No hull | None | None | 128x128 | 5.07 | RP80 |

Charge* ---mass of PETN charge; all unit in mm unless specified.

The steel frame and floorboard dimensions used in the experiments are given in Table 3.4 and shown in Figure 3.15. Designated experiments 16 and 17, the authors employ the same aluminum floorboard without benefit of a protective hull so that the results could be compared directly to data obtained in experiments 14 and 15 respectively, where an aluminum frame is used.

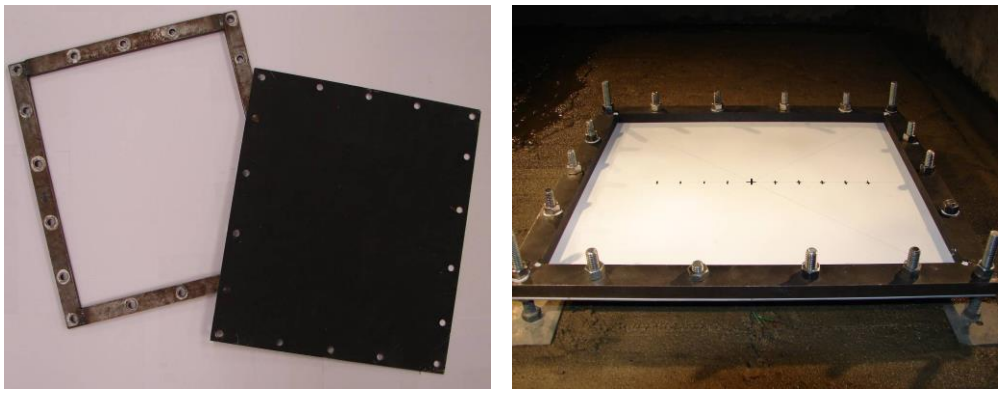

Figure 3.15 Floorboard and steel frame specimen for experiments 16 and 17 with no hull. The steel frame was constructed by welding 12.7mm by 25.4mm steel stock into a rectangle and drilling the 18 holes with 9.525mm diameter for holding the plate. The dimensions of frame are 12.7mm thickness, 25.4mm width, 355.6 x 406.4mm external dimension, which are same as aluminum frame used in experiments 1-15, (cont′d).

Figures 3.16 and 3.17 present direct comparisons of the measured out-of-plane displacement and acceleration at the plate center-point for (a) Exp 14 (aluminum frame)

and Exp 16 (steel frame) with DoB =7.62mm and (b) Exp 15 (aluminum frame) and Exp 17 (steel frame) with DoB=25.4mm. Figures 3.18 present direct comparisons of the measured $HIC_{15}$ values at the plate center-point for Exp 14 and Exp 16 and Exp 15 and Exp 17, respectively.

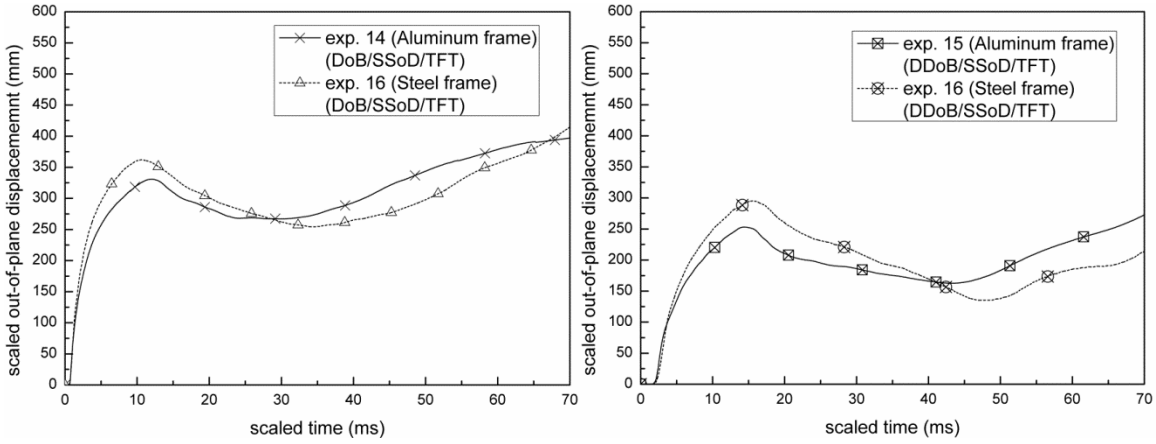


Figure 3.16 Comparison of input-scaled out-of-plane displacement for center-point of floorboard using an aluminum and steel frame with DoB= 7.62mm (top) and input-scaled out-of-plane displacement for center-point of floorboard using an aluminum and steel frame with DDoB= 25.4mm (bottom). Aluminum floorboard thickness is TFT=1.60mm in all cases and data scaled to full-size structure response. (SSoD= 31mm).

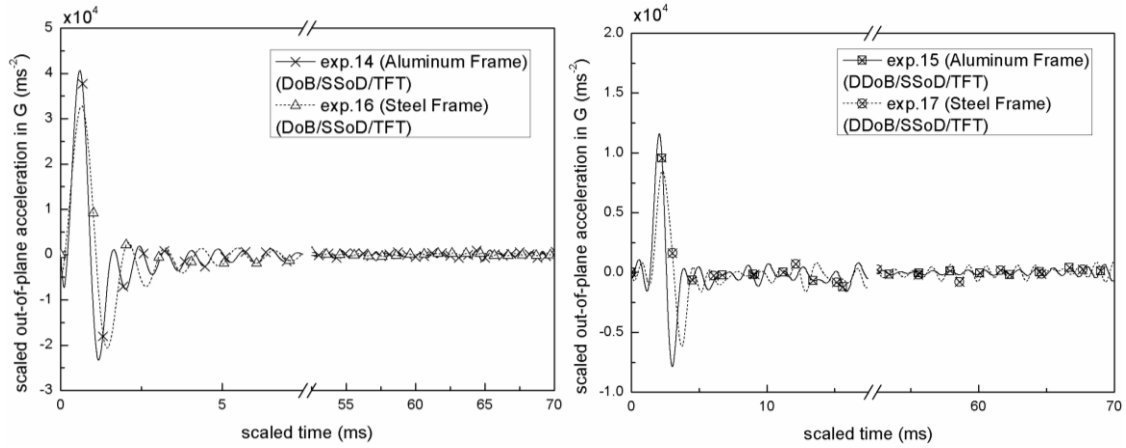


Figure 3.17 Comparison of input-scaled out-of-plane accelerations (in G's) for center-point of floorboard using an aluminum and steel frame with DoB= 7.62mm (top) and input-scaled out-of-plane accelerations (in G's) for center-point of floorboard using an aluminum and steel frame with DDoB= 25.4mm (bottom). Aluminum floorboard thickness is TFT=1.60mm in all cases and data scaled to full-size structure response. (SSoD=31mm).

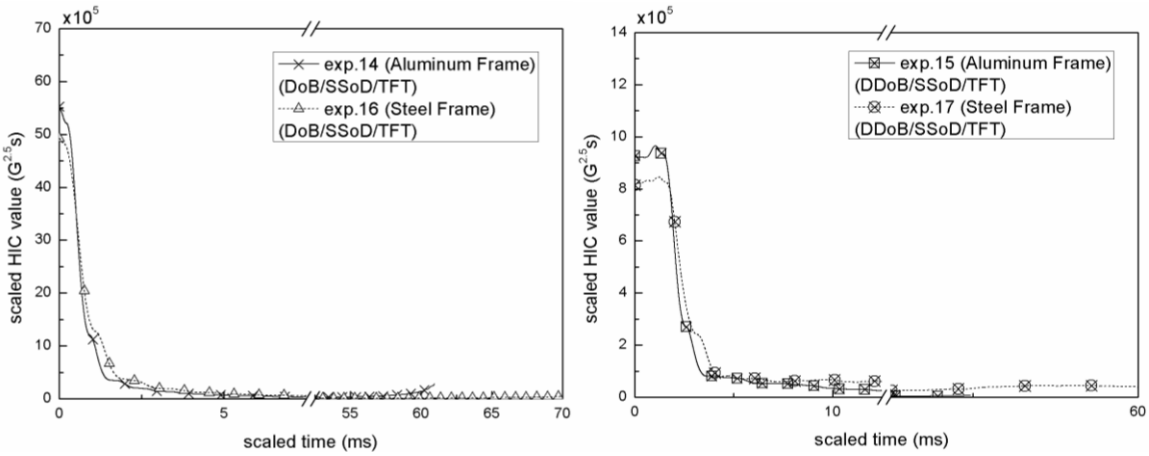


Figure 3.18 Comparison of input-scaled $HIC_{15}$ values for center-point of floorboard using an aluminum and steel frame with DOB = 7.62mm (top) and input-scaled $HIC_{15}$ values for center-point of floorboard using an aluminum and steel frame with DOB = 25.4mm (bottom). Aluminum floorboard thickness is 1.60mm in all cases and data scaled to full-size structure response. (SSoD-31mm).

Direct comparison of the results in Figures 3.16, 3.17 and 3.18 clearly show that the change from an aluminum frame to a steel frame with somewhat different attachment procedure has minimal effect on the measured center-point acceleration and $HIC_{15}$ values. Based on these results, as well as a general observation regarding the more common use of steel in frame structures, the investigators will use the steel frame for the second set of experiments (Hurley 2011).

Finally, as reported in detail in the second set of experiments (Hurley 2011), to demonstrate that the 3D-DIC data is consistent with independent measurements, the authors attach accelerometers to the frame of several structures used in our experiments. Comparison of accelerometer and 3D-DIC measurements for the same region on the various frame structures demonstrated that the 3D-DIC data were in excellent agreement with accelerometer values in all cases where the accelerometer continued to function during the blast event.

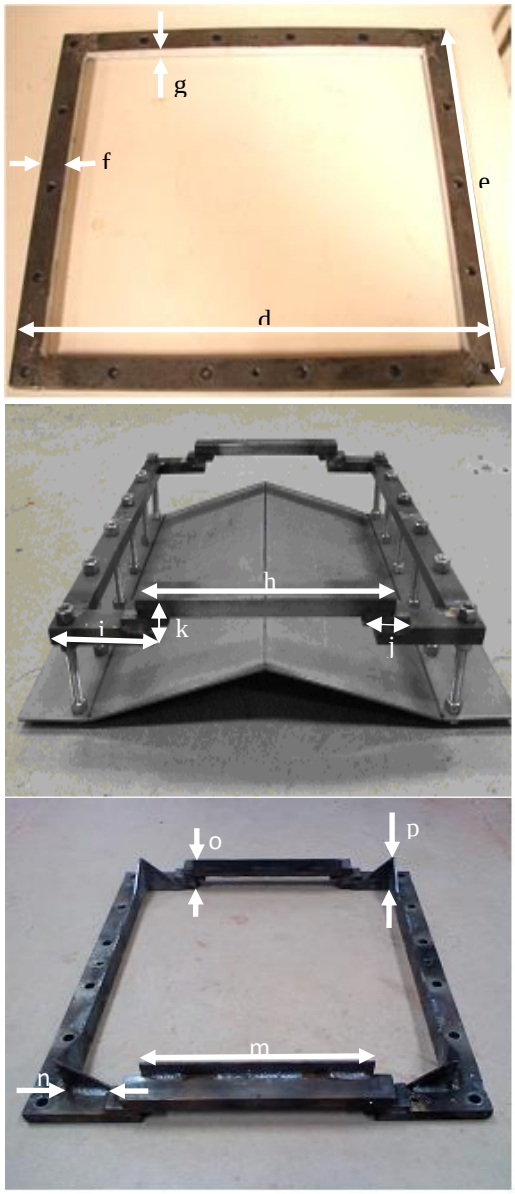


Figure 3.19 Photo of (a) original frame(top): d=355.60, e=406.40, f=25.40, g=12.70; (b) pocket frame with inverted hull (middle): h=203.20, i=76.20, j=38.10, k=38.10; (c) pocket frame without hull (bottom): m=177.80, n=25.40, o=50.80; p=50.80. (unit mm).

## 3.9 INVESTIGATIONS OF ALTERNATIVE STRUCTURES

Since floorboard motion data obtained by the investigators for the structures in the first set of experiments described in previous sections show that out-of-plane accelerations and $HIC_{15}$ values are quite high, the experiments in the second set of experiments focused on the response of frame members. All experiments are performed using 4.4g of

explosive (corresponding to 4.536kg of TNT), with 1018 steel structural elements, inverted hulls[4] and various mitigation systems, without floorboard.

### 3.9.1 STEEL FRAME STRUCTURES

The frames types are designated original, pocket and pocket-reinforced and shown in Figure 3.19.

#### 3.9.1.1 ORIGINAL FRAME

As shown in Figure 3.19 (top), the first type of steel frame tested is a rectangular frame with outer dimensions 355.60mm × 406.40mm. The steel bars used to construct the frame were 25.40mm × 12.70mm in size. The weight of the as-constructed frame is 3.541kg. Bolt holes with diameter of 9.53mm are drilled around the perimeter of the frame at 76.20mm center to center spacing along the 406.40mm spans, and 88.9mm spacing along the 355.60mm spans. To mount the accelerometers, 7.62mm deep threaded holes are tapped into the frame at the center of each 406.40mm span and at one corner with a 6.35mm-28tpi male tap.

#### 3.9.1.2 POCKET FRAME

The second type of steel frame is a modified rectangular frame shown in Figure 3.19 (middle), which will be referred to as a pocket frame. The pocket frame has outer dimensions 355.60mm × 406.40mm and a height of 31.75mm. The weight of the pocket frame is 3.987kg. Bolt holes 9.53mm in diameter are drilled through the 406.40mm spans at 76.20mm center to center spacing. Threaded holes are tapped into the frame in the same size and location as in the first steel frame in order to provide identical mounting locations for accelerometers. The pocket frame features a vertical offset along the short

[4] Recent analytical and experimental work (Brodrick 2010, Fox 2011) suggests that an inverted V-shaped hull possesses a greater capacity for deflecting blast impulse than the traditional V-shape. Because of this advantage, inverted V-shaped hulls are used in this study.

span to increase clearance between the hull and frame as the lower hull is deformed during blast loading.

#### 3.9.1.3 REINFORCED POCKET FRAME

The third type of frame is created by modifying the pocket frame and will be referred to as a reinforced pocket frame. As shown in Figure 3.19 (bottom), the original pocket frame is modified by welding 25.40mm wide, 2.66mm thick strips of 1018 sheet steel in several locations to the existing 25.40mm × 12.70mm steel bars. The weight of the reinforced pocket frame is 4.471kg.

### 3.9.2 INVERTED V-SHAPE HULLS

Two types of inverted V-shaped vehicle hulls are used in the experiments. The inverted vehicle hulls are all formed from 406.40mm x 457.20mm square sections of 1018 sheet steel with 2.29mm thickness. As shown in Figures 3.20(a-d), the first type of hull, designated IV-1, is an inverted V-shaped hull that was bent to obtain an internal angle of $154^{o}$ with a hand sheet metal bender. This hull has two unrestrained and unreinforced edges. As shown in Figures 3.20(h) and 2(i), the IV-1 hull was slightly modified to include two V-shaped 38.10mm × 1.90mm thick strips of steel bolted to the hull along both free edges as local reinforcement to reduce the potential for frame-hull contact.

The second type of hull used in the experiments is designated IV-2 and is constructed of the same material and method as the IV-1 hull, with rectangular cut-out sections removed from the free ends to provide increased space between hull and frame and reduce hull-frame contact during blast loading. The cutouts along the unrestrained edges of the hulls are shown in Figures 3.20(e-g).

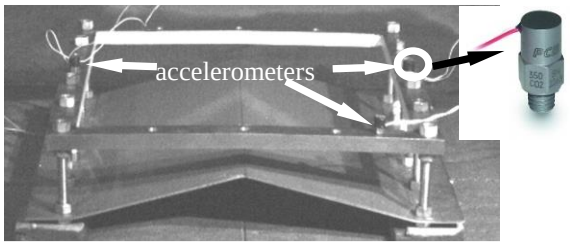


(a) original frame with inverted hull

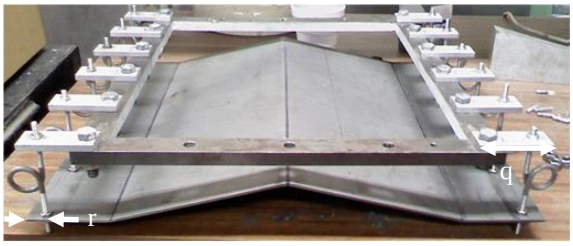


(b) original frame with inverted hull and coil springs

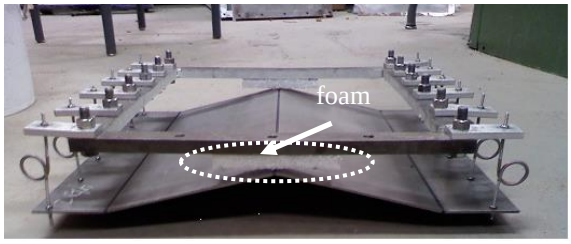


(c) original frame with inverted hull and softer coil springs

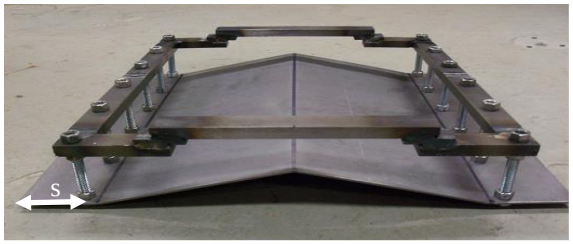


(d) pocket frame with inverted hull and no mitigation

(e) reinforced pocket frame with inverted hull and strut truss

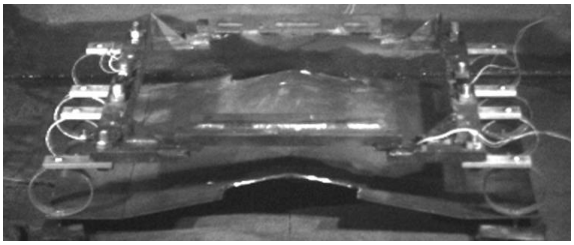

(f) reinforced pocket frame with inverted hull and tubes

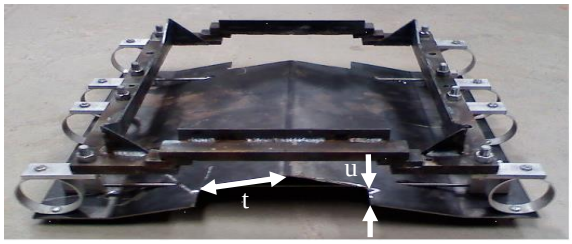


(g) reinforced pocket frame with inverted hull, tubes and strut rods

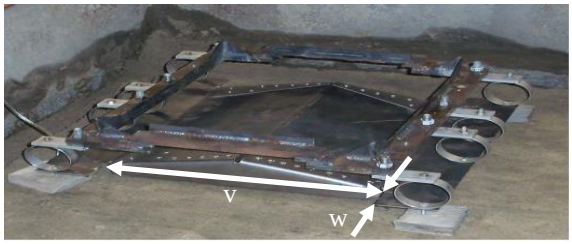


(h) reinforced pocket frame with inverted hull, tubes and hull end plates

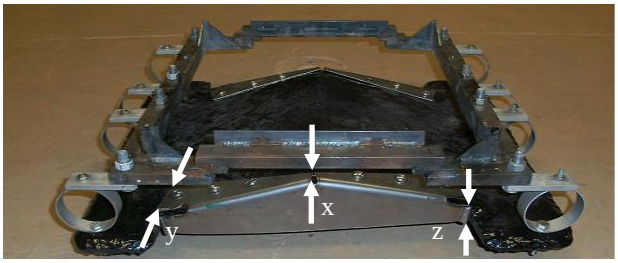


(i) reinforced pocket frame with tubes and polyurea coated inverted hull with end plates

Figure 3.20 Photos of hulls, edge mitigation components and frames (q=50.80; r=25.40; s=58.74; t=130.34; u=31.75; v=304.80; w=31.75; x=12.70; y=38.10; z=12.70; unit mm).

### 3.9.3 MITIGATION SYSTEMS

Besides the effect of steel frame construction methods and inverted hull configurations, various frame-mounted mitigation systems are employed in experiments. The mitigation systems are described in the following sub-sections and summarized in Table 3.5.

#### 3.9.3.1 ORIGINAL FRAME AND IV-1 HULL WITHOUT EDGE MITIGATION

As a control, the first experiment is performed with the original frame and an IV-1 hull in order to determine acceleration values on the frame when no mitigation techniques are used. As shown in Figure 3.20(a), the IV-1 hull is rigidly attached to the control frame with 9.53mm diameter bolts. The measured acceleration values are used as a baseline to compare against all other experiments in order to quantify mitigation improvements.

#### 3.9.3.2 ORIGINAL FRAME WITH IV-1 HULL AND COIL SPRINGS

As shown in Figure 3.20(b), the second experiment involves connecting the original frame to the IV-1 hull with hand-made 4.76mm diameter coil springs[5]. The coil springs are designed to deform under sufficient load, dissipating energy through plastic deformation when significant relative motion occurred between the hull and frame.

#### 3.9.3.3 ORIGINAL FRAME WITH IV-1 HULL, FOAM STRIP AND COMPLIANT COIL SPRINGS

Figure 3.20(c) presents the third experimental specimen, which is nearly identical to the previous one, except hand-made 3.18mm coil springs are used[6]. Each spring has a stiffness value of 27.4N/mm, providing a total stiffness of 328.3N/mm for the entire connection. In addition to the smaller springs, a thin strip of rigid white foam is inserted

[5] The springs were made by first threading an aluminum rod on a lathe with a 10-32 die. The center of the rod was then twisted around a larger rigid rod with a diameter of 19.05mm (0.75in). Tensile tests performed on the springs revealed that they had a stiffness value of 104.9N/mm, providing a total stiffness of 1258.8N/mm for the entire connection.

[6] The 3.18mm (1/8in) springs were manufactured in the same fashion as the larger springs, except a 5-40 die was used.

between the frame and hull to dampen transient impact events between the hull and the frame that occurred in previous experiments, resulting in peaks in both rigid body acceleration and high frequency frame vibration.[7]

Table 3.5 List of frame measurement for blast loading experiments

| Exp. # | DoB (mm) | SoD to frame (mm) | SoD to hull (mm) | Designation frame/hull | Technique (mm) | Frame dimensions (mm) | Charge (grams) | 1018 steel hull thickness (mm) | Angle of hull (degrees) | Detonator |
|---|---|---|---|---|---|---|---|---|---|---|
| 18 | 9.91 | 80.52 | 25.40 | Original / IV-1 | None | 335.60×406.40 | 4.4 | 2.66 | 13/154/13 | RP87 |
| 19 | 9.91 | 80.52 | 25.40 | Original / IV-1 | 4.76mm Coils | 335.60×406.40 | 4.4 | 2.66 | 13/154/13 | RP87 |
| 20 | 9.91 | 80.52 | 25.40 | Original / IV-1 | 3.18mm Coils | 335.60×406.40 | 4.4 | 2.66 | 13/154/13 | RP87 |
| 21 | 9.91 | 80.52 | 25.40 | Pocket / IV-1 | None | 335.60×406.40 | 4.4 | 2.66 | 13/154/13 | RP87 |
| 22 | 9.91 | 80.52 | 25.40 | Reinforced Pocket / IV-2 | Compression Strut truss, Hull Cuts | 335.60×406.40 | 4.4 | 2.66 | 13/154/13 | RP87 |
| 23 | 9.91 | 91.44 | 25.40 | Reinforced Pocket / IV-2 | Lateral Tubes | 335.60×406.40 | 4.4 | 2.66 | 13/154/13 | RP87 |
| 24 | 9.91 | 91.44 | 25.40 | Reinforced Pocket / IV-2 | Lateral Tubes, Compression Struts | 335.60×406.40 | 4.4 | 2.66 | 13/154/13 | RP87 |
| 25 | 9.91 | 91.44 | 25.40 | Reinforced Pocket / IV-2 | Lateral Tubes, Hull Cuts, Hull End Plates | 335.60×406.40 | 4.4 | 2.66 | 13/154/13 | RP87 |
| 26 | 9.91 | 91.44 | 25.40 | Reinforced Pocket / IV-2 | Polyurea Coat, Lateral Tubes, Hull Cuts and Plates | 335.60×406.40 | 4.4 | 2.66 | 13/154/13 | RP87 |

#### 3.9.3.4 POCKET FRAME WITH IV-1 HULL WITHOUT MITIGATION TECHNIQUES

In response to the high peak accelerations and vibrations caused by violent impact of the hull with the vehicle frame, the pocket frame shown in Figure 3.20(b) is integrated with the IV-1 hull as shown in Figure 3.20(d) to deform and dissipate energy without hull-

[7] The rigid foam fractured during blast loading, with negligible mitigation effect, and is not used in any further studies.

frame contact. As a control experiment, no additional mitigation techniques are investigated in addition to the use of the pocket frame.

#### 3.9.3.5 REINFORCED POCKET FRAME WITH IV-2 HULL AND STRUT TRUSS MITIGATION SYSTEMS

The reinforced pocket frame is created to provide additional stiffness in the frame structure. In addition, the IV-2 hull is introduced to allow more hull deformation before frame impact, while also reducing potential for frame-hull impact. The installation of a compression strut truss is the main edge mitigation technique for this experiment. The compression strut truss is created with 3.18mm diameter aluminum rods arranged in three "X" patterns on each side of the vehicle, as shown in Figure 3.20(e).

#### 3.9.3.6 REINFORCED POCKET FRAME WITH IV-2 HULL AND ALUMINUM TUBE MITIGATION SYSTEMS

As shown in Figure 3.20(f), aluminum 6061-T6 tubes are installed and configured to crush laterally, utilizing one of the more powerful energy dissipation techniques---lateral tube flattening. The tubes are 57.15mm in outer diameter, 54.66mm in inner diameter and 15.88mm in length.

#### 3.9.3.7 REINFORCED POCKET FRAME WITH IV-2 HULL AND ALUMINUM TUBES WITH STRUT ROD MITIGATION SYSTEMS

As shown in Figure 3.20(g), three aluminum bar struts are installed across the width of the specimen in the back, middle and front to prevent violent contraction of the IV-2 hull and frame during blast loading. The first technique is to install struts. The struts are 4.76mm diameter aluminum rod, threaded on each end by a 10-32 die, and attached to each side of the hull with small tapped aluminum blocks. The blocks are attached to the top surface of the sides of the hull with bolts.

#### 3.9.3.8 REINFORCED POCKET FRAME WITH IV-2 HULL AND ALUMINUM TUBES WITH HULL END PLATE MITIGATION SYSTEMS

The specimen is similar to the others that employed laterally installed aluminum tubes. Rather than using compression rods spanning the width of the specimen, "end plates" are installed on the front and back of the hull where the hull was cut out. These end plates, shown in Figure 3.20(h) on the vehicle hull, are manufacture from 1.90mm 1018 sheet steel, bent with the assistance of a table top clamp. During hull deformation, the end plates tend to buckle laterally due to in-plane moments, creating another means of energy dissipation. The end plates are attached to the hull with rivets in this experiment.

#### 3.9.3.9 REINFORCED POCKET FRAME WITH IV-2 HULL COATED IN POLYUREA AND ALUMINUM TUBES WITH END PLATE MITIGATION SYSTEMS

The experimental configuration is identical to the one shown in Figure 3.20(h), with the addition of a ~7mm thick coating of polyurea on the bottom surface of the IV-2 hull and side frame members for additional blast mitigation.

### 3.9.4 ACCELERATION MEASUREMENTS: EXPERIMENTS #18-26

Acceleration measurements are obtained on three types of steel frames that employed energy absorption techniques to mitigate the acceleration effects. All frame accelerations are measured using PCB piezotronics (Model 350C02) accelerometers. A typical accelerometer is shown as an inset in Figure 3.20a. A total of three accelerometers are mounted to each steel frame. As shown in Figure 3.20a, two accelerometers are mounted at the centers of each 406.40mm span and one is mounted in a corner of the frame. Kenlube grease is used in each accelerometer hole to ensure a tight connection between the accelerometer and the frame. The accelerometers are calibrated up to 10,000Hz and have a maximum acceleration threshold of 50,000 G's. Accelerometer signals are

processed by a PCB Piezotronics Amplifier (model 483A). After being processed by the amplifier, the signals are sent to two LeCroy oscilloscopes (9314AM and 9315AM). The signals are split between the two scopes and captured at different voltages. The different voltage settings allow one scope to capture more sensitive data than the other to prevent data clipping.

Three accelerometers are installed on each frame. Inspection of the raw accelerometer data clearly show the presence of noise due to structural vibrations associated with hull-frame impact and subsequent energy transfer. These structural vibrations induce high frequency spikes in the test data, resulting in unreasonably high, short duration peaks in the acceleration data. These peaks are not indicative of the frame's rigid body motion and therefore are not considered in the analysis of vehicle response. To remove these components, filtering of acceleration-time data using a 600 Hz cutoff frequency is used to retain the lower frequency signal and obtain meaningful results, allowing the largest peak information associated with representative frame motions to be considered while eliminating the majority of the high frequency motions associated with structural contact effects.

To verify that the filtered accelerometer data accurately represents the frame motion for experiments #18-26, independent frame displacement versus time data is acquired by stereovision-based digital image correlation at mid-span using two Phantom V7.3 cameras sharing the same trigger as the accelerometer. The resolution of images is 256×64 pixels at 100,000 frame per second. Each subset is chosen to be sufficiently large so that good contrast is present and the matching process is accurate. For all the measurements, the standard deviation of displacement is less than 0.1mm, which is much

less than the deformations measured during the blast loading process. Also, the projection error in the sensor plane is less than 0.1 pixels. For comparison to the vision-based measurements, the filtered accelerometer data of the right edge span is integrated twice with respect to time and compared to the out-of-plane displacement data obtained from 3D-DIC. Figure 3.21 compares the vision-based and accelerometer-based measurements of vertical displacement for experiments #18-26. As shown in Figure 3.21, the level of agreement ranges from good to excellent. Detailed review of the accelerometer and vision-based method[8] does not provide a conclusive reason for the differences that were observed in some cases.

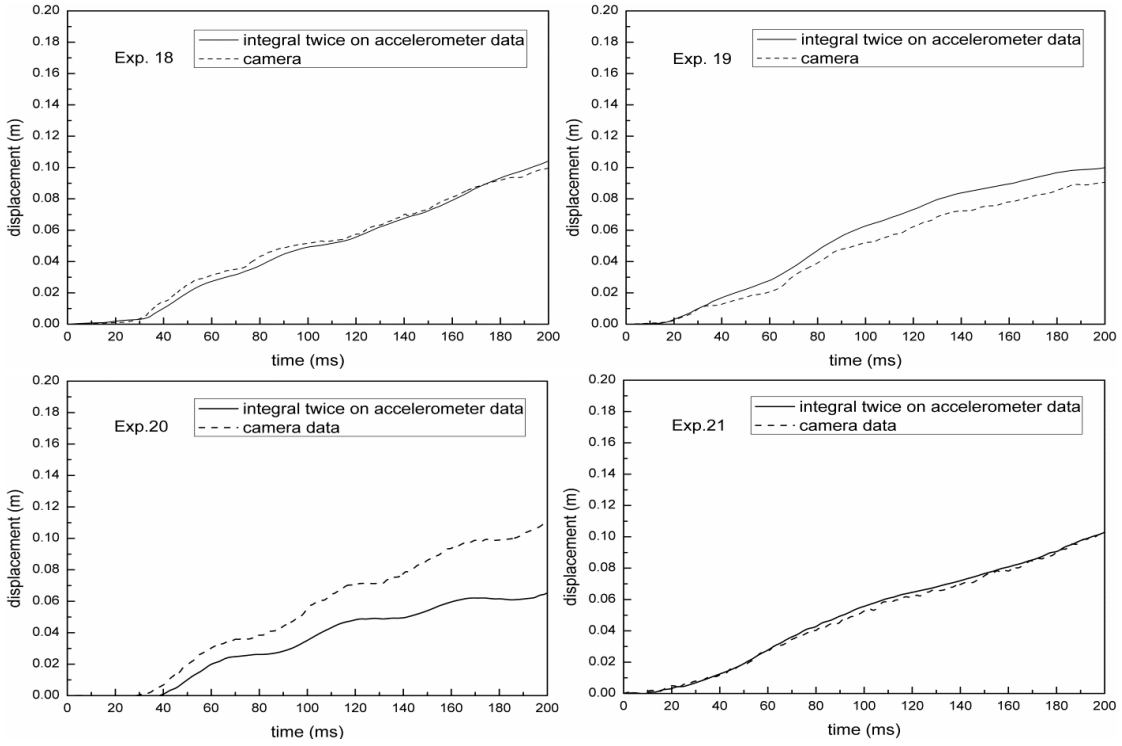


Figure 3.21 Comparison of displacement data from digital image correlation and accelerometer at the center of right 406.40mm edge span. Note that image data for exp. 24 was not usable due to trigger malfunction.

[8]Measurements from another independent stereovision system were in agreement with our vision-based measurements for Experiment 20, providing additional confidence in the vision-based measurements. It is conjectured that the slight retardation seen in the accelerometer data may have been due to variations in the screw connection between accelerometer and frame.

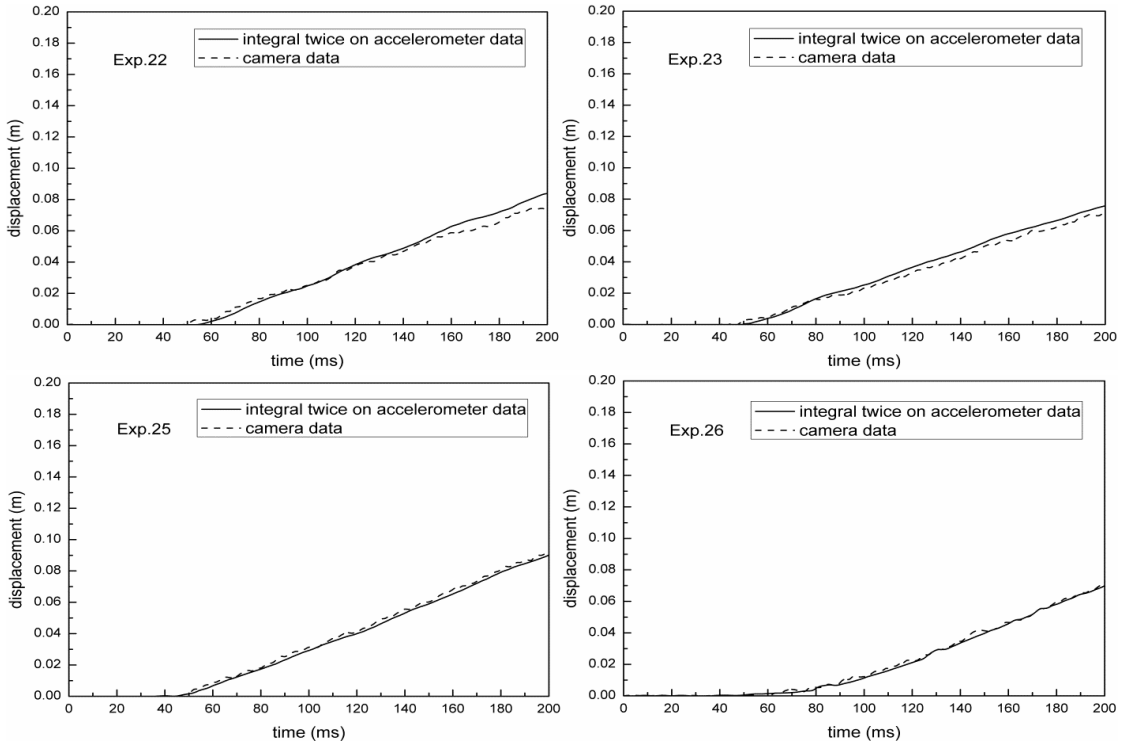


Figure 3.21 Comparison of displacement data from digital image correlation and accelerometer at the center of right 406.40mm edge span. Note that image data for exp. 24 was not usable due to trigger malfunction (cont′d).

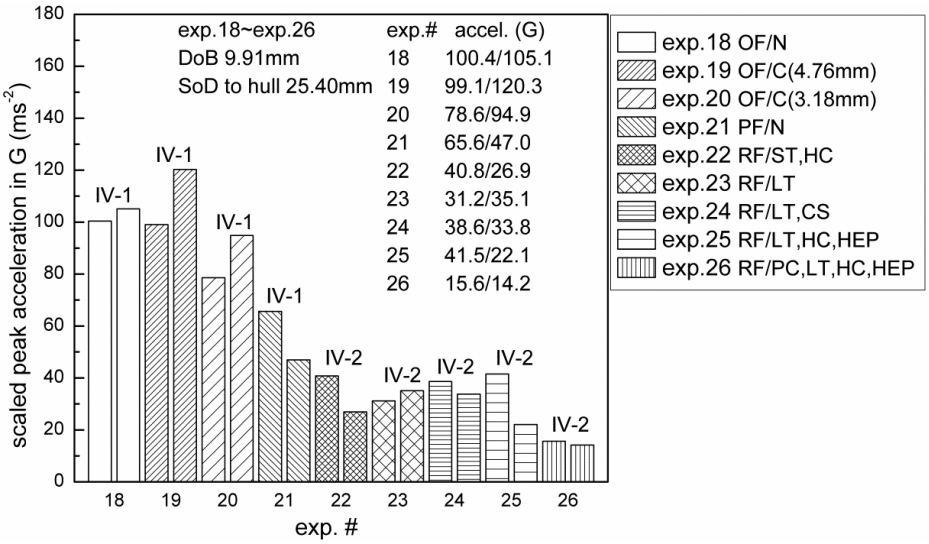


Figure 3.22 Input-scaled peak accelerometer data at middle edge span (left bar) and corner (right bar) of the frame for each experiment case from 18 to 26. (IV-1-inverted V-shape hull type 1, IV-2-inverted V-shape hull type 2. OF-original frame, PF-pocket frame, RF-reinforced frame, N-none, C-coils, ST-strut truss, HC-hull cuts, LT-lateral tubes, CT-compression struts, HEP-hull end plates, PC-polyurea coat.

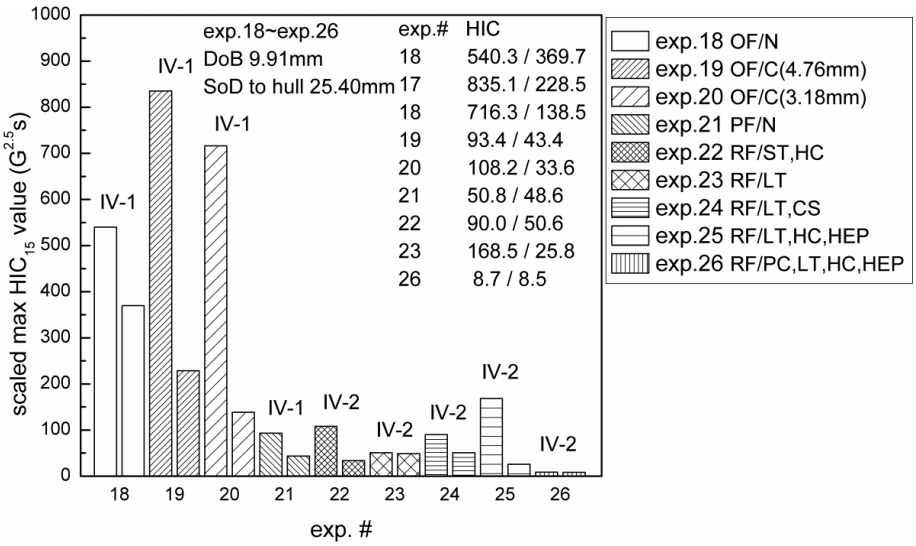


Figure 3.23 Scaled maximum HIC value at side location (left bar) and corner location (right bar) for experiments 18-26. (IV-1-inverted V-shape hull type 1, IV-2-inverted V-shape hull type 2. OF-original frame, PF-pocket frame, RF-reinforced frame, N-none, C-coils, ST-strut truss, HC-hull cuts, LT-lateral tubes, CT-compression struts, HEP-hull end plates, PC-polyurea coat).

After performing frequency filtering on all accelerometer data, Figure 3.22 presents the maximum measured frame accelerations at a corner and at mid-span for Experiments #18-26. Appendix D presents the filtered experimental data for the frame acceleration in all Experiments #18-26 at frame locations.

The $HIC_{15}$ vs. time data are obtained for Experiments 18-26 using Eq (3-2) and the procedure outlined in Appendix E. The maximum $HIC_{15}$ value for each experiment is presented in Figure 3.23.

### 3.9.5 DISCUSSIONS

In Experiments #18-26, the inverted hull is fully restrained along two edges, with edge mitigation systems used to provide increased flexibility. In such cases, hull protection emanates from plastic dissipation in the hull and edge load transfer into mitigation systems that further dissipate blast effects.

Comparison of the minimum floorboard acceleration results (460G) for experiments #1-15 in Part I to the minimum frame acceleration in experiments #18-26 shown in Figure 4 clearly shows that frame accelerations are ≈ 31X smaller than floorboard accelerations; maximum frame accelerations range from 120G (original frame, IV-1 hull, coil springs) to 15G (reinforced frame, IV-2 hull with polyurea coating, tube springs), even though the explosive mass is 4.4X larger for the frame experiments.

Further inspection of Figure 3.22 shows that

(a) measured frame accelerations generally are independent of measurement location; corner and frame mid-span gave similar results,

(b) pocket frame construction (Experiment #21) has a measurable positive effect, reducing maximum measured acceleration by minimizing hull-frame contact,

(c) pocket frame reinforcement (Experiments #22-26) in corners and along sides further reduced the measured frame acceleration results and

(d) polyurea hull coating provides substantial additional mitigation of accelerations, though at the expense of considerable weight increase.

Only one frame structure (Experiment #26) has maximum acceleration magnitudes below the DoD limiting value (25G), with temporal duration that is much less than the 100ms assumed to be necessary for biological damage.

As shown in Figure 3.22, corner frame measurements in Experiments #22-26 indicate that all edge mitigation systems have similar effects, reducing maximum acceleration. The results in Figure 6 show that edge mitigation systems have a secondary effect, increasing the vibratory response of the frame through increased edge flexibility. For this reason, damping systems such as polyurea coatings offer additional benefit.

As shown in Figure 3.23, the $HIC_{15}^{max}$ values for positions on the frame ranged from 8 to 840. In contrast to the trends observed for maximum acceleration, the smallest measured $HIC_{15}$ values always occurred at the corner of the frame-hull structure. The structures that are below the corresponding $HIC_{15}$ value of the DoD standard (25G for 100ms→ HIC=312.5$Gs^{-1}$) are

- Pocket frame with IV-1 hull (experiment #21, $HIC_{15}^{max} \approx 93$)
- Reinforced pocket frame with IV-2 hull and strut mitigation (experiment #22, $HIC_{15}^{max} \approx 108$)
- Reinforced pocket frame with cutout, IV-2 hull, tube mitigation (experiment #23, $HIC_{15}^{max} \approx 50$)
- Reinforced pocket frame with cutout, IV-2 hull, tube and strut mitigation (experiment #24, $HIC_{15}^{max} \approx 90$)
- Reinforced pocket frame with cutout, IV-2 hull, tube and hull end plate mitigation (experiment #25, $HIC_{15}^{max} \approx 168$)
- Polyurea coating of inverted hull ($HIC_{15}^{max} \approx 8$)

Though our results clearly show that the use of polyurea on hulls will substantially improve blast mitigation, the additional weight that would be required to incorporate such dense materials is most likely prohibitive, highlighting the need for additional studies focused on identifying less dense alternatives.

## 3.10 CONCLUSIONS

Single standard hulls use an optimized included angle of 154 ° in order to minimize the transmission of energy to the structure. The single corrugated hull employs similar geometry with corrugation to decrease stiffness and further reduce transmission.

Unfortunately, under the same blast loading conditions as the single hull, the increased deformation of a single corrugated hull resulted in contact with the floorboard and increased energy transfer. Specifically, the results show that the corrugated hull does not decrease the measured floorboard acceleration.

Interestingly, by adding an additional degree of freedom through cantilevering of the corrugated and standard V-shaped hulls, data shows that this geometry change results in reductions in floorboard acceleration for both hulls. The cantilevered single corrugated hull performs somewhat better than a cantilever single hull in acceleration reduction because of the corrugation.

Finally, it is noted that increasing floorboard thickness is much less effective than using protective hulls for acceleration reduction. Moreover, thicker floorboards will result in increased total vehicle weight, which is unacceptable in practice.

In conclusion, results from our experiments clearly show that V-shaped hull structures with an optimized included angle of $154°$ are effective in reducing structure acceleration and associated human injury metrics, especially the cantilevered single corrugated hull. For the same DoB, use of a cantilevered single corrugated hull (experiment 9) reduces the peak value of deflection by 4X, acceleration by 47X and $HIC_{15}$ by 128X when compared to the case with no hull (experiment 1). However, even though the V-shaped hull with the optimum bend angle does significantly reduce accelerations relative to the no-hull configuration, the resulting floorboard accelerations are still be too large to prevent serious injury. Thus, the safety of passengers in a vehicle subjected to the effects of an IED explosive blast also relies heavily on internal human seat positioning and attachment. As a result, the focus of the research in a second set of

experiments is to quantify the accelerations of a frame structure and ascertain the effectiveness of frame-mounted passenger seating in reducing passenger injury metrics.

The second set of experiments is performed by Ryan Hurley (Hurley 2011) at University of Maryland. Results from second set of experiments clearly show that hull structures are effective in reducing structure acceleration and associated human injury metrics. Even so, as shown in Experiments #1-15, though a standard V-shaped hull with the optimum bend angle does significantly reduce accelerations from the no-hull configuration, the resulting accelerations may still be too large to prevent serious injury. Thus, the safety of passengers in a vehicle subjected to the effects of an IED explosive blast also relies heavily on internal human seat positioning and attachment.

Acceleration data supported by $HIC_{15}$ values from a second set of experiments #18-26 point to a certain family of alterations capable of significantly reducing G-forces experienced by passengers; positioning of passenger seating on stiff frame support components that are designed to minimize hull-frame impact. For example, the IV-2 hull with reinforced pocket frame significantly improves acceleration mitigation. Additional mitigation is observed when using a relatively thick coating of polyurea on the inverted hull, significantly reducing both $HIC_{15}$ and maximum acceleration. In the future, thinner coatings of polyurea or development of lower density materials with similar properties should be considered.

## 3.11 SUMMARY

Small scale models representing key vehicle structural elements, including both floorboards and bottom-mounted, downward V-shape hulls in various configurations, have been manufactured and subjected to a range of buried blast loading conditions. By

varying surface stand-off distance and depth of burial for several hull and structure configurations, the *input-scaled response* of aluminum full-scale vehicle floorboards has been quantified using high speed stereo-vision. Specifically, the maximum vertical acceleration on the floorboard and the corresponding Head Injury Criterion ($HIC_{15}$) are quantified as metrics to assess the severity of the blast event. Results show standard V-shaped hulls provide essential blast mitigation, with reductions in floorboard measurements up to 47X in maximum acceleration and $HIC_{15}$. Though variations in protective hull geometry provide modest reductions in the severity of a floorboard blast event, results also show that personnel on typical floorboard structures during blast loading events will incur unacceptable shock loading conditions, resulting in either serious or fatal injury. A more appropriate design scenario would be to consider situations that employ frame-mounted passenger seating to reduce the potential for injury. Therefore, a second set of experiments focuses on frame motions and accelerations when steel frames and steel structures were performed with various frame connections and coatings for frame blast mitigation.

Results from the second set of experiments show that (a) inverted and standard V-shaped hulls provide essential blast mitigation capability, reducing the maximum frame accelerations over 100X, with similar reductions also measured for $HIC_{15}$, (b) stiffened frame structure locations experience substantially lower levels of acceleration and $HIC_{15}$ than measured previously on the floorboard at the expense of decreased damping of structural vibrations and (c) hull coating systems such as polyurea provide significant additional mitigation, though at the expense of increased overall weight.

# CHAPTER 4

# EXPERIMENTAL VALIDATION OF STEREO IMAGE BASED PARTICLE TRACKING IN FLUIDS AND APPLICATION TO FRICTION EXTRUSION PROCESS

## 4.1 LITERATURE REVIEW

The accurate measurement of full-field displacement and velocity distributions for both flow fields and also for objects that are immersed or suspended in a fluid is important in a wide variety of research and industrial areas. Since imaging often occurs through transparent media, in the past few decades investigators have worked on problems related to refraction effects at interface in various applications. Sutton et al. (Sutton 2000) calculated and measured the pseudo displacements and strains caused by refraction when light travels through a water-glass-air combination. Hobson and Watson (Hobson 1999) modeled the interface problem in holography by introducing a deliberate mismatch of recording and replying reference beams to compensate for the refraction index mismatch. Moore (Moore 2001) worked with laser line scan system for underwater measurements. Plakas (Plakas 1998) circumvented the interface problem by immersing cameras in the fluid. Kwon (Kwon 1999) pointed out in his work that the coordinates of refraction points are determined by an unknown ratio ‘k’ based on the interface-to-calibration grid distance. He proposed to optimize the distance separately and optimize other factors in the system through an iterative approach using the Newton method. In Taboada's work (Taboada 2003), she placed the cylindrical tank inside of other transparent square tank that serves as a curvature correcting lens. Corkidi (Corkidi 2008) used Taboada's

technique in order to remove the optical curvature effect caused by the refraction of the cylindrical tank and corrected the light refraction effects introduced by water or air bubbles embedded within an oil drop. Ke et al. (Ke 2008) developed a complete calibration methodology for digital image correlation measurements on submerged objects when viewing the object through a transparent window, though no experimental evidence was provided to demonstrate the efficacy of the approach. Andre (Kyme 2012) proposed a refraction compensation model for motion tracking of unrestrained small animals in positron emission tomography.

Regarding the area of fluid field measurements, one of the first optical techniques to be employed was laser Doppler velocimetry (LDV) (Durst 1976, Tropea 2007), which allows one to measure the velocity at a single point in the flow. Multiple experiments must be performed to obtain the velocity at several points in the flow. Particle image velocimetry (PIV) (Adrian 1991, Raffel 2007) allows the entire flow field in a plane of interest to be captured in a single experiment. Conventional 2D PIV allows the measurement of the two velocity components for particles illuminated by a plane of laser light. Dual-plane PIV is a first step towards 3D measurement since it maintains the side-view characteristics of PIV, but records data from two neighboring planes on separate cameras that are discriminated by polarization or wavelength (Hu 2001, Ganapathisubramani 2005). Multi-plane stereo PIV (Kähler 2000) and stereoscopic PIV (Prasad 1993, Gaydon 1997) are additional extensions of 2D PIV that allow for the measurement of all three components of the velocity flow field at points within the plane of interest. Here, the *Scheimpflug condition* is usually satisfied to overcome focusing problems in angular displacement (Larmore 1965) Since optical distortions are involved

in the mapping function for positions of points illuminated by a sheet of light (thin illuminated volume) (Soloff 1997, Raffel 1998), a refractive index matching fluid method (Johnston 1975, Hopkins 2000, Budwig 2004) oftentimes is used to mitigate refraction effects at the fluid-viewing window (such as plexiglass) interface. Besides refraction index matching, a few researchers (Arizaga 2010, Bao 2011) have considered the refraction problem at fluid and air interfaces and corrected the measurements along a known vertical direction.

In addition to PIV, particle tracking velocimetry (PTV) was developed to identify and match individual particles to obtain their Lagrangian trajectories and velocity vectors. A limitation of PTV techniques is that they can only make measurements in a small volume of several centimeters, requiring more than two cameras to reduce ambiguities in the correspondence analysis (Mass 1993, Malik 1993). Over the years, large scale PIV/PTV (LSPIV/LSPTV) systems have been developed as extensions of standard PIV/PTV, providing expanded fields of view (Muste 2004, Li 2008, Tang 2008, Coz 2010, Lobutova 2010, Dramais 2011, Kantoush 2011, , Muste 2011). The LSPIV/LSPTV approach is especially effective for shallow flow measurement. Two approaches are employed to expand the field of view: (a) oblique-imaging and (b) multi-channel methods. With the expansion of the field of view, more problems are introduced that await solutions so that they can be used more effectively in applications (Fujita 1998, Kim 2002, Kim 2006).

In this chapter, a convenient and efficient method is proposed for the accurate measurement of particle motions in applications where refraction effects must be modeled and corrected. The methodology is especially useful for applications where (a)

large scale motions are of interest or (b) complete full field measurement of particle motions is required. Following the work of Ke (Ke 2008), an air, glass and fluid optical model is employed and the orientation and position of interfaces for different media are obtained by using a calibration process. With known interface parameters, the object's true spatial position in the liquid can be reconstructed accurately. An experimental set-up is designed and tests are performed using a calibration and reconstruction process to obtain image-based quantitative position measurements for comparison to independent, known values as a way to validate the optical methodology. Finally, the motion of neutrally buoyant particles entrained in a viscous fluid that is undergoing a stirring extrusion process are tracked by stereo-vision system using the validated method.

## 4.2 PARTICLE TRACKING IN FLUID BY DIGITAL IMAGE CORRELATION

Refraction of light at multiple interfaces will introduce distortions in images that affect the accuracy of image-based measurement methods. In order to obtain accurate measurements, a calibration process was introduced for the stereo camera system to incorporate refraction effects. Once calibrated, the stereo camera system can accurately identify the true, three-dimensional positions, motions and velocity vectors for particles moving within fluid environment.

### 4.2.1 CALIBRATION PROCESS

As shown in Figure 4.1 and the symbol list in Table 4.1, for a particle physically located at Q in a fluid, a virtual position $Q'$ is obtained when image points on the camera sensor planes are back-projected into space without considering refraction effects. To obtain the true position Q, the optical path needs to be identified by including the effects of refraction at the air/glass and glass/fluid interfaces. To achieve this goal, Ke (Ke 2008)

proposes a calibration process to separately obtain (a) extrinsic and external parameters of cameras and (b) orientations and positions of interfaces. Major assumptions in this model are as follows;

- refraction indexes of media (fluid and glass) are constant
- A/G (air/glass) and G/F (glass/fluid) interfaces between different media are planar and parallel to each other
- Interfaces do not change position or orientation during the experiment

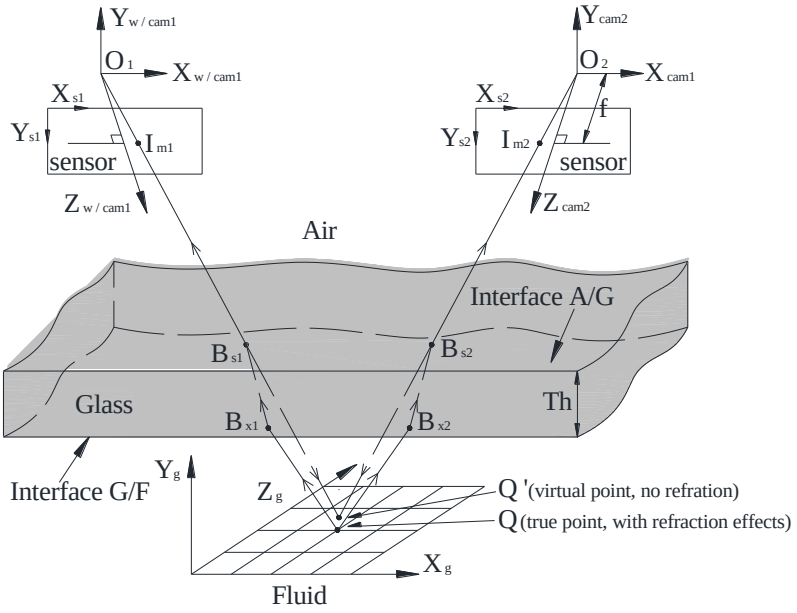


Figure 4.1 Optical model of stereo camera system.

Table 4.1 List of characters in figures for chapter 4

| **Symbols** | **Notes** |
|---|---|
| ($X_{w/cam1}$, $Y_{w/cam1}$, $Z_{w/cam1}$) | World coordinate system / Camera 1 coordinate system (see Figure 4.1) |
| ($X_{cam2}$, $Y_{cam2}$, $Z_{cam2}$) | Camera 2 coordinate system (see Figure 4.1) |
| $O_1$ / $O_2$ | Focal points for cameras 1 and 2, respectively (see Figure 4.1) |
| f | Perpendicular distance from pinhole to sensor plane (see Figure 4.1); oftentimes designated as focal length. |
| ($X_{s1}$, $Y_{s1}$) | Sensor coordinate system of camera 1 (see Figure 4.1) |
| ($X_{s2}$, $Y_{s2}$) | Sensor coordinate system of camera 2 (see Figure 4.1) |

Table 4.1 List of characters in figures for chapter 4 (cont′d)

| **Symbols** | **Notes** |
|---|---|
| $I_{m1}$ / $I_{m2}$ | Point on sensor plane of camera 1 / camera 2 (see Figure 4.1) |
| $B_{s1}$ / $B_{s2}$ | Intersection point on the air-glass interface (see Figure 4.1) |
| $B_{x1}$ / $B_{x2}$ | Intersection point on the glass-fluid interface (see Figure 4.1) |
| Q | General object point in fluid (see Figure 4.1) |
| $Q'$ | Virtual point obtained without refraction effects (see Figure 4.1) |
| ($X_g$, $Y_g$, $Z_g$) | Grid coordinate system (see Figure 4.1) |
| $O_1'$ / $O_1''$ | Projections of point $O_1$ onto both glass interfaces (see Figure 4.3) |
| $I_{m1}'$ / $I_{m1}''$ | Projections of point $I_{m1}$ onto both interfaces (see Figure 4.3) |
| $O_2'$ / $O_2''$ | Projections of point $O_2$ onto both glass interfaces (see Figure 4.3) |
| $I_{m2}'$ / $I_{m2}''$ | Projections of point $I_{m2}$ onto both in interfaces (see Figure 4.3) |
| $\beta_1$ / $\beta_2$, $\delta_1$ / $\delta_2$, $\alpha_1$ / $\alpha_2$ | Refraction angles (see Figure 4.3) |
| ($x_s^{o\text{-}G}$, $y_s^{o\text{-}G}$) | Coordinates of imaged grid points on sensor plane |
| ($x_s^{mo\text{-}G}$, $y_s^{mo\text{-}G}$) | Coordinates of grid points projected back by the model on the sensor |
| ($x_s^{o}$, $y_s^{o}$) | Coordinates of image points on sensor plane |
| ($x_s^{mo}$, $y_s^{mo}$) | Coordinates of image points optimized by model for reconstruction |
| a, b, d | Unit vector for planar interface of air and glass |
| $S_x^{cam1cam/2}$ | Horizontal scale factor of camera 1and camera 2 (pixels/mm) |
| $S_y^{cam1/cam2}$ | Vertical scale factor of camera 1and camera 2 ( pixels/mm) |
| $f_x^{cam1/cam2}$ | $f_x$=f $S_x^{cam1/2}$ of camera 1 and camera2, f is lens focal length |
| $f_y^{cam1/cam2}$ | $f_y$=f $S_y^{cam1/2}$ of camera 1 and camera 2, f is lens focal length |
| $Skew^{cam1/cam2}$ | Skew factors for camera 1 and camera 2 |
| $k^{cam1/cam2}$ | Lens distortion factors for camera 1 and camera 2 |
| $\theta_x$, $\theta_y$, $\theta_z$ | Transformation (rotation) of camera 2 relative to camera 1 |
| $T_x$, $T_y$, $T_z$ | Transformation (translation) of camera 2 relative to camera 1 |
| $D_x^1$, $D_y^1$, $D_z^1$ | Translation of grid relative to world coordinate system for 1st image |
| $D_x^i$, $D_y^i$, $D_z^i$ | Translation of grid relative to world coordinate system for ith image |
| $\gamma_x^1$ , $\gamma_x^1$ , $\gamma_x^1$ | Rotation angles of grid relative to world coordinate system for 1st image |
| $\gamma_x^i$, $\gamma_x^i$, $\gamma_x^i$ | Rotation angles of grid relative to world coordinate system for ith image |

Figure 4.2 shows an updated flow chart for the calibration process. First, a grid pattern with known grid spacing is employed to calibrate the stereo cameras in air to obtain the intrinsic and extrinsic parameters for the stereo cameras ($f_x^{cam1/2}$, $f_y^{cam1/2}$, $S_x^{cam1/2}$, $S_y^{cam1/2}$,$skew^{cam1/2}$, $k^{cam1/2}$, $\Theta_x$, $\Theta_y$, $\Theta_z$,$T_x$, $T_y$, $T_z$) (Sutton, 2009). Once

they are determined, then the parameters are assumed to be constant until the final step of calibration process.

Second, the same grid or another appropriate calibration grid with known spacing distance is immersed in the fluid and images are acquired by both stereo cameras as they view the grid through the air, glass and fluid media.

Third, by assuming planar glass-air and glass-fluid interfaces, Equation (4-1) is used to define the orientation and position of the air-glass interface.

$$ax + by + (\sqrt{1 - a^2 - b^2})z + d = 0 \tag{4-1}$$

x, y and z are in the world coordinate system. With known intrinsic and extrinsic camera parameters obtained during air calibration, the orientations and positions of interfaces $(a, b, \sqrt{1 - a^2 - b^2}, d)$ are determined by minimizing the error Equation (4-2) using bundle adjustment and a Levenberg-Marquardt (LM) algorithm.

$$\chi^2 = \sum_{k=1}^{2} \sum_{i=1}^{N\ Views} \sum_{j=1}^{M\ Points} [(x_s^{mo-G}{}_{i,j,k} - x_s^{o-G}{}_{i,j,k})^2 + (y_s^{mo-G}{}_{i,j,k} - y_s^{o-G}{}_{i,j,k})^2] \tag{4-2}$$

The Equation (4-2) is built as sum of differences between coordinates of grid points on the sensor plane ($x_s^{\text{o-G}}$ , $y_s^{\text{o-G}}$) and back projection of grid points ($x_s^{\text{mo-G}}$, $y_s^{\text{mo-G}}$) onto the sensor plane by the model for each camera, using each point on the grid and all views of the grid. The unknown orientations and positions of the interface are involved in back projecting coordinates of grid points onto the sensor and determined by minimizing $\chi$ in Equation (4-2). Finally, setting all the known values of parameters as initial guesses, a global optimization process is applied to optimize all the parameters in order to further minimize $\chi$ in Equation (4-2) , including slight updates to the intrinsic and extrinsic camera parameters, orientations, and positions of interfaces and positions of each calibration grid pattern view ($D_x^1$, $D_y^1$ , $D_z^1$, $\gamma_x^1$, $\gamma_y^1$ , $\gamma_z^1$,…, $D_x^i$, $D_y^i$ , $D_z^i$, $\gamma_x^i$, $\gamma_y^i$ , $\gamma_z^i$).

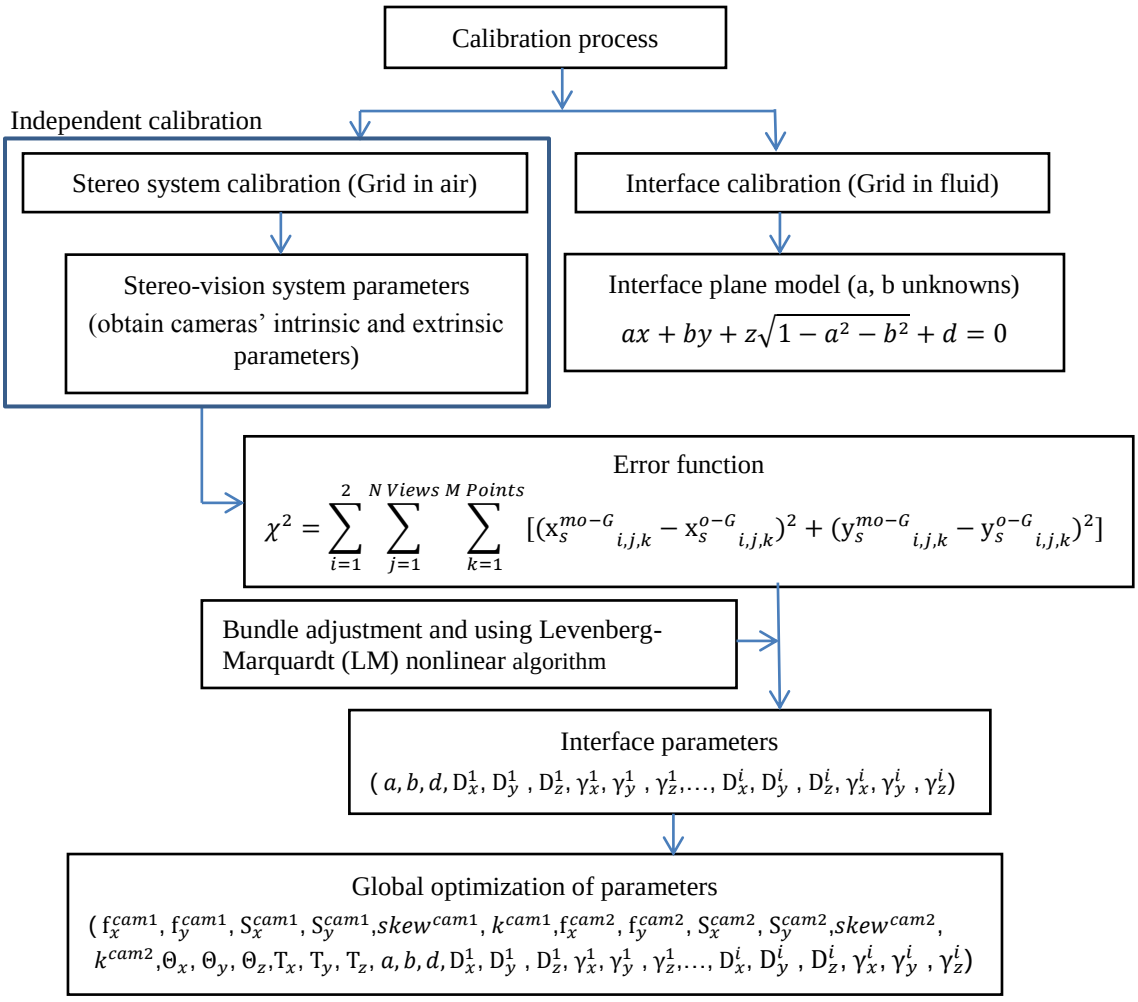


Figure 4.2 Flow chart of calibration process.

### 4.2.2 SPATIAL POSITION RECONSTRUCTION

After completion of the calibration process, experiments can be performed for particle tracking or for digital image correlation, depending upon whether individual particles or a random pattern on a submerged surface are to be observed. To convert image positions in both cameras into true, three-dimensional locations in the fluid, a reconstruction process is applied to the stereo images of the common point (region). Figure 4.3(a) shows the transmitted path in a plane and Figure 4.3(b) shows a flow chart for the reconstruction process. For tracked particles Q(x,y,z) in a fluid, $(x^o_{si}, y^o_{si})$ is the corresponding image point on camera sensor plane. The reconstruction process is performed by minimizing the

error function in Equation (4-3) by optimizing the sensor position $x^{mo}{}_{si}$ and $y^{mo}{}_{si}$ since the optical paths of directly projected imaged points such as $(x^{o}{}_{si}, y^{o}{}_{si})$ into space may not intersect.

$$\chi^2_{rec} = \sum_{i=1}^{2}[\left(x^{o}{}_{s\,i} - x^{mo}{}_{s\,i}\right)^2 + \left(y^{o}{}_{s\,i} - y^{mo}{}_{s\,i}\right)^2 + \lambda_i(\|\overline{Q''O_i''}\| - \|\overline{B_{si}O_i''}\| - \|\overline{B''_{xi}B_{si}}\| - \|\overline{Q''B''_{xi}}\|)] \quad (4\text{-}3)$$

The error function (4-3) is defined as the sum of the differences between reconstructed positions on the sensor plane and measured image positions of tracked particles on the sensor plane for each camera. Here, $\lambda_i$ is a Lagrangian multiplier for a constraint which requires a constant distance from $O''_i$ to $Q''$ for each camera shown in Figure 3.3(a). The projection error is defined for the reconstruction process by equation (4-4) as follows.

$$k = sqrt(\sum_{i=1}^{2}\left[\left(x^{o}{}_{s\,i} - x^{mo}{}_{s\,i}\right)^2 + \left(y^{o}{}_{s\,i} - y^{mo}{}_{s\,i}\right)^2\right]/2) \quad (4\text{-}4)$$

It is important to note that this analysis must be performed for each pair of stereo image points to extract the corresponding 3D positions of the point of interest.

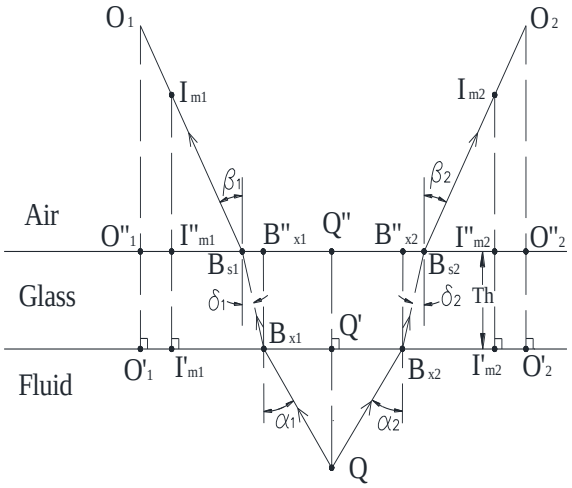


(a)

Figure 4.3 Reconstruction process: (a) transmitted light path in a plane; (b) flow chart of reconstruction.

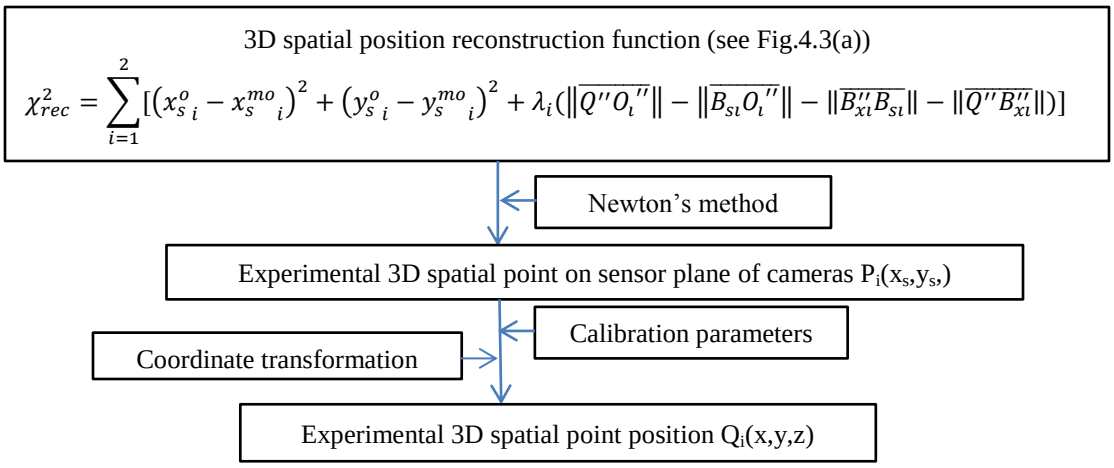


(b)

Figure 4.3 Reconstruction process: (a) transmitted light path in a plane; (b) flow chart of reconstruction (cont′d).

## 4.3 EXPERIMENTAL VALIDATIONS OF DIC MEASUREMENTS IN FLUID

### 4.3.1 EXPERIMENTAL SETUP

Since the process outlined in Section 4.2 has never been experimentally validated, a specially designed experimental set-up was developed for both (a) initial experimental validation studies and (b) fluid extrusion experiments. Figure 4.4 shows photos of the experimental set-up. As shown in Figure 4.4(a), an empty right circular cylindrical chamber that is 38.10mm in diameter and 50.80mm in height is placed inside a 152.40mm×152.40mm×76.20mm clear acrylic block. The block could be connected to a vertical support column shown in Figure 4.4 and leave enough space below the block for locating cameras which view inside of the chamber from the bottom of block. As shown in Figure 4.4(b), the top cap of the chamber is a rotation tool, which is an aluminum disk with 50.80mm diameter and a 3.81mm diameter fluid extrusion hole at the center. The bottom of chamber, a high quality Edmund Scientific optical glass plate with 19.05mm thickness, 76.20mm diameter and surface flatness of $\lambda/4$, is shown in Figure 4.4(c). Transparent liquid could flow into chamber through an inlet pipe which is connected to a

fluid reservoir. Air inside the chamber would be expelled from the center hole of the rotation tool to avoid trapping air in the chamber when fluid flows into the chamber. The rotation tool is driven by the motor and pulley system shown in Figure 4.4(d). The direct output speed of the motor is 3rpm and is reduced to 0.5rpm by pulleys for the tool rotation experiments.

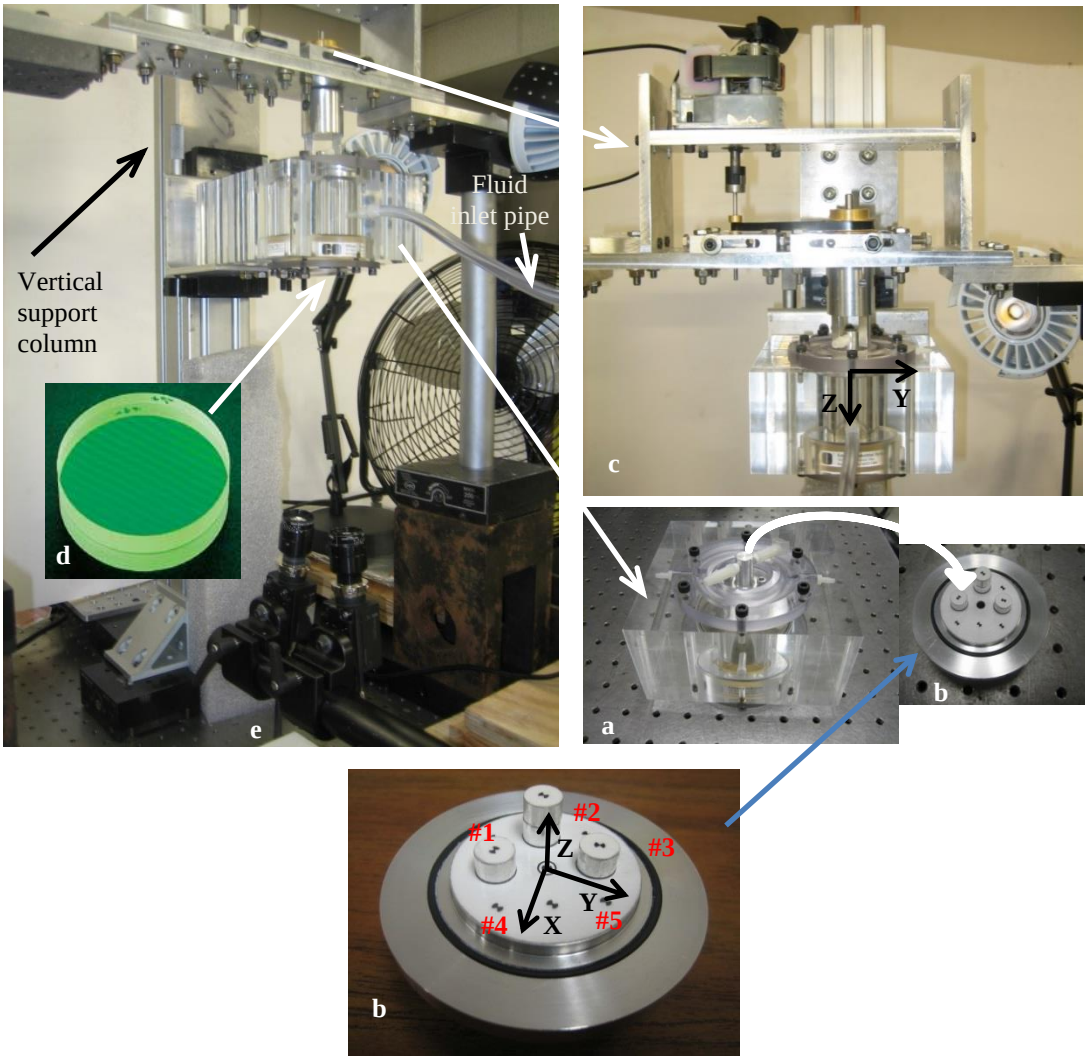


Figure 4.4 Photographs of experimental configuration (a) chamber block; (b) rotation tool with rigid pillars #1, #2, #3 (marker is at the center of each pillar) and markers on tool surface #4 and #5; (c) motor and pulley system (d) optical glass; (e) cameras.

To mitigate measured temperature increases in the fluid inside the chamber during initial experiments using halogen lighting for illumination, the authors construct a

lighting system using cold LED lights for illumination. In addition, three electric fans are isolated and located at the sides of the chamber block to assist in cooling the radiation fins of the LED lights and moving the heated air away from the extrusion chamber. After installing the LED lighting, thermocouple measurements confirmed that temperature increases in the fluid are $< 3^{o}$ Celsius for all experiments.

The stereo cameras shown in Figure 4.4(e) are fixed on an optical bench and rotated to view upwards through the bottom optical glass of the chamber to observe markers in the fluid. The two cameras' optical arrangement used in the experiment has the following overall configuration: Distance from lens to the optical glass ≈ 330mm; Focal length = 50mm; F# = 11; Intensity quantization = 8 bits; Cross-camera synchronization using software trigger to 1μs; Camera frame rate = 1/5 fps; Lighting using multiple LED lamps; Total pan angle between the two cameras' optical axes ≈ 13 °. It is noted that the relatively small pan angle is required because of the small diameter of the chamber and the physical size of the two cameras.

### 4.3.2 EXPERIMENTAL MEASUREMENTS IN SYRUP FLUID

In the first set of validation experiments, the model fluid used is a transparent Karo light corn syrup. After calibration is completed, the cameras observe the motion of three circular pillars and two markers attached rigidly to the upper rotation tool. Figure 4.4(b) shows the pillars and markers on the bottom of the upper rotation tool. During the validation experiments, the upper tool rotated but there is no extrusion of fluid from the chamber. The three pillars attached to the upper rotating tool surface are rigid cylindrical aluminum pillars, as shown in Figure 4.4(b). The length of each pillar below the tool surface and the radial distance of each pillar and the two markers from the rotation center

(the origin of the coordinate system is at the rotation tool center and the X-Y plane is in the upper tool surface plane, with the Z direction along the length of the pillars. The coordinate system is shown in Figure 4.4) is measured independently using a Gauge 2000 coordinate measurement system. The pillar lengths and radial distance from center for three pillars and two markers on the rotation tool surfaces are 5.222mm (#1), 10.378mm (#2), 5.330mm (#3), 0mm (#4), 0mm (#5), and 9.893mm (#1), 10.191mm (#2), 10.075mm (#3), 14.245mm (#4), 14.227mm (#5) respectively.

To measure the length of each pillar using stereo image pairs, tracking markers are drawn on the upper surface of each pillars and numbered as #1, #2 and #3. In addition, two more markers are located on the upper surface of the rotation tool and numbered as #4 and #5. The pillars extend downward into the chamber and are immersed in the fluid. Figures 4.5 and 4.6 show measured height and radius results for the rigid pillars in syrup fluid when using 3D DIC for particle tracking[9]. Since the initial position of all pillars and markers are fixed in advanced, only the position in X-Y plane will change appreciably and should form a circle path during tool rotation. The circular motions are measured for all markers and shown in Figure 4.7. (The coordinate system is shown in Figure 4.4)

Tangential velocity is obtained in the following manner after the spatial positions of tracked markers are obtained. First, a time series of data for $U_z$ at each spatial position is obtained at every 5s interval. Second, using this time sequence, a "moving window least squares quadratic fit" is performed in time using five consecutive data points for

[9] The particle tracking option in the code VIC-3D, www.correlatedsolutions.com, was used to obtain the 3D positions. Due to the relatively small size of the sugar particles used in the experiments (less than 7x7 pixels) and the relatively large displacements between images, initial particle position estimates at many/most time steps were required to be input manually for the particle tracking calculations to converge.

each displacement component. Third, the quadratic fit is differentiated once to obtain the velocity component at the mid-point of the time span. This process is repeated by moving forward in time by one time step until the entire velocity component history is obtained. Then, the same procedure is applied to $U_y$ to obtain velocity component in Y direction. The tangential velocity is the resultant of velocity components in X and Y directions. The vectors shown in Figure 4.7 are the "measured" tangential velocities of tracked markers and the vector length corresponds to the magnitude of velocity. The tangential velocity is converted to angular velocity in order to compare with design value of rotation speed.

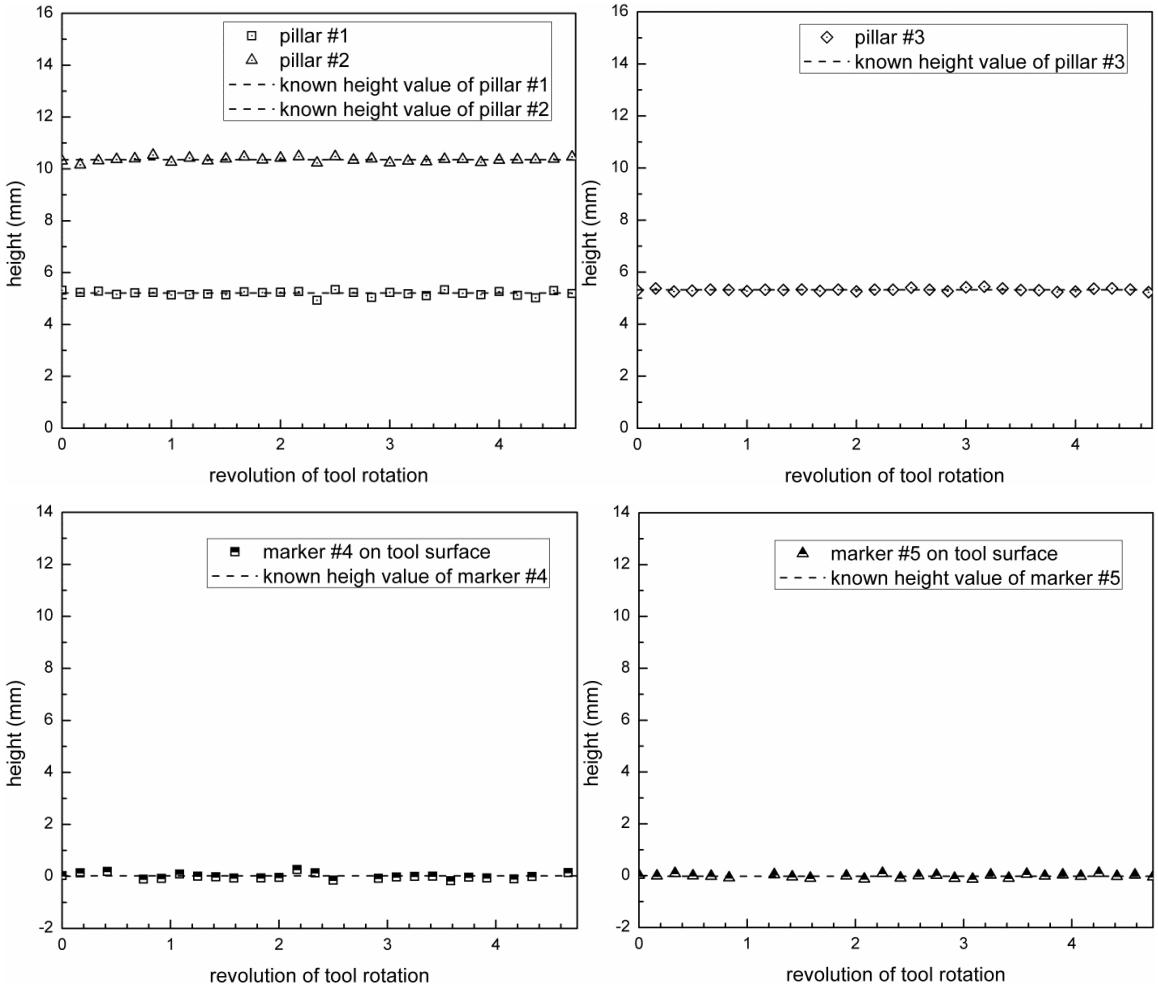


Figure 4.5 Experimental measurements of the heights of pillars (#1-3) and markers (#4-5) in syrup fluid.

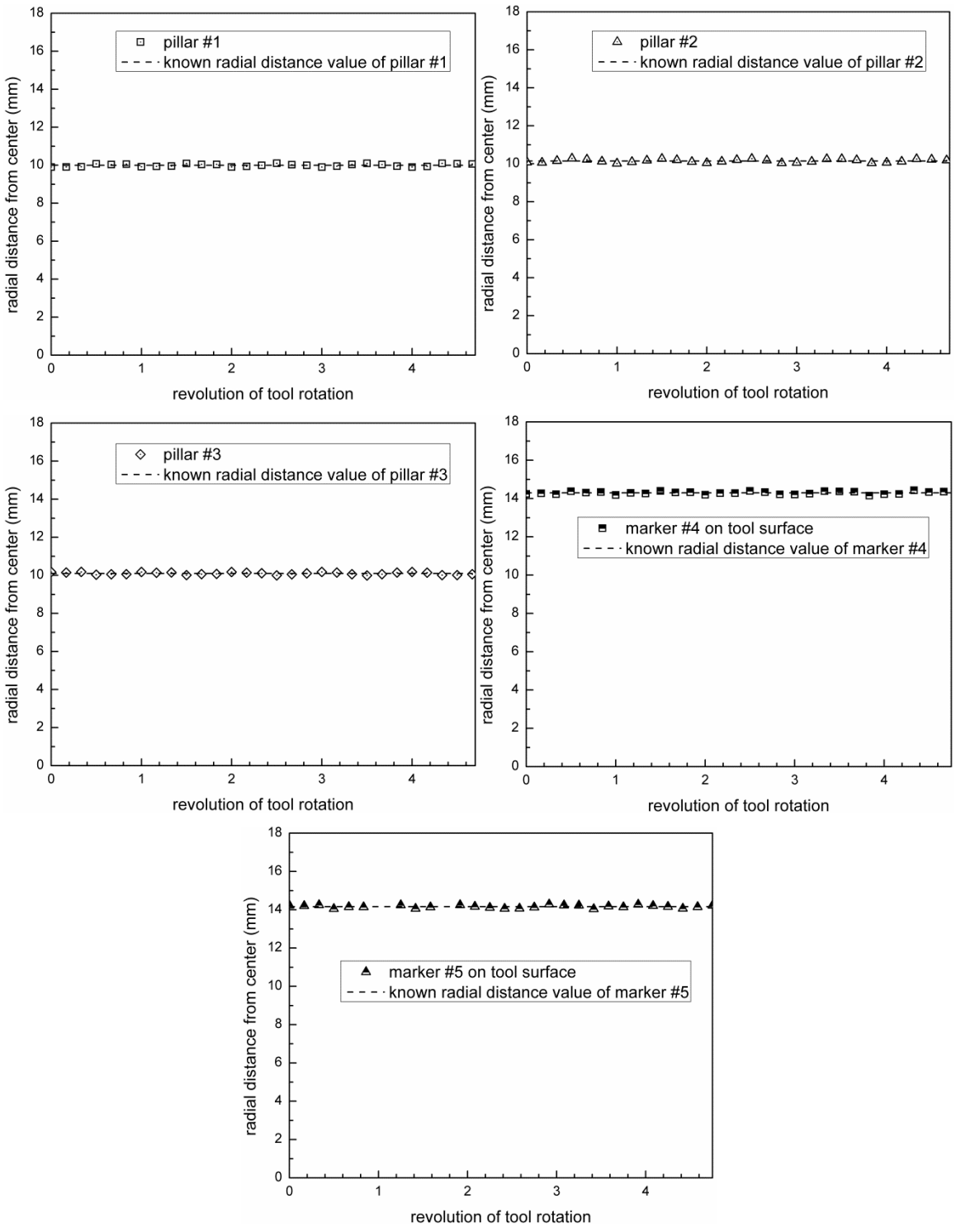


Figure 4.6 Experimental measurements of the radial positions of the pillars (#1-3) and markers (#4-5) in syrup fluid.

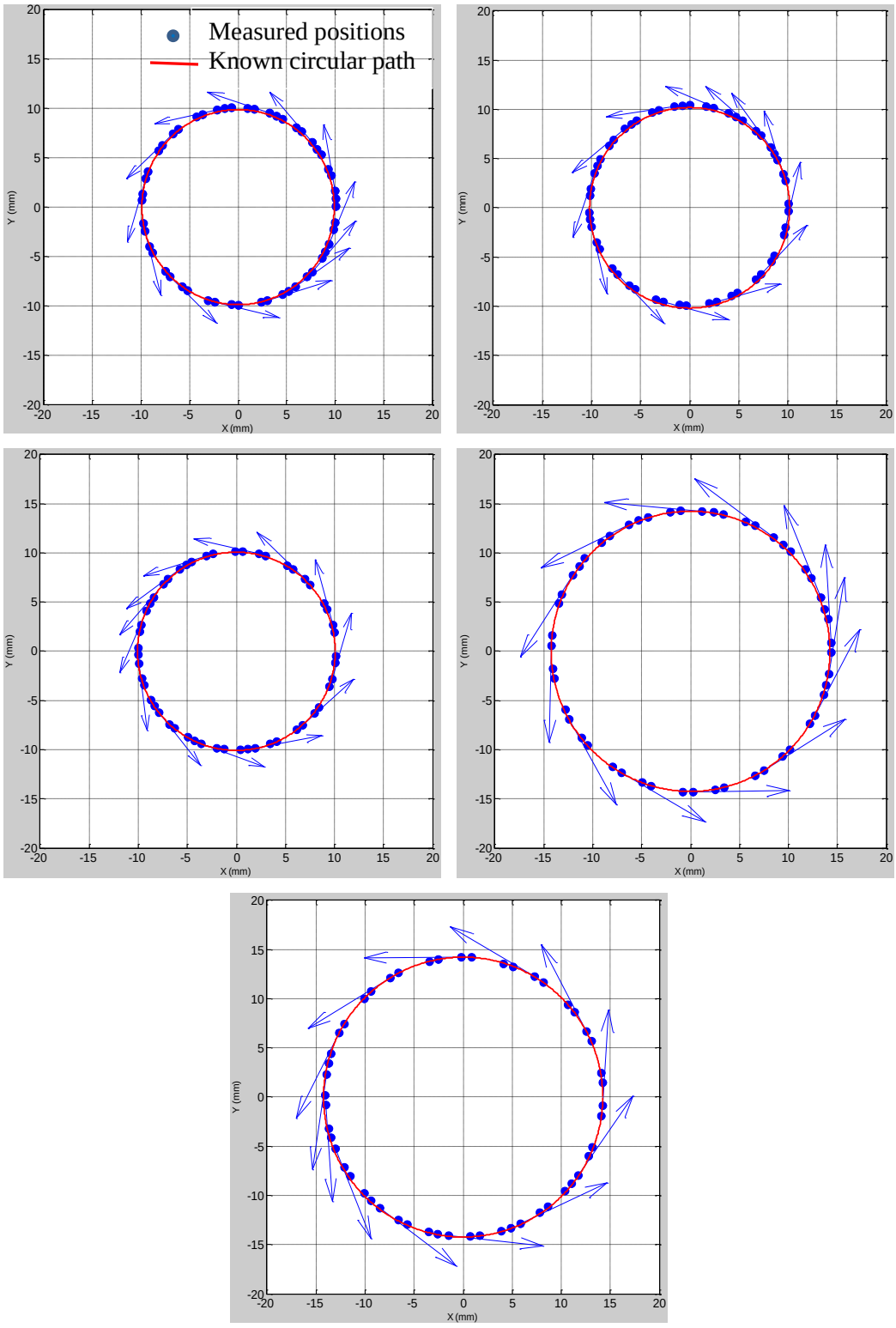


Figure 4.7 Motions of pillars (#1-3) and markers (#4-5) on tool surface. Blue arrows are the local velocity vectors.

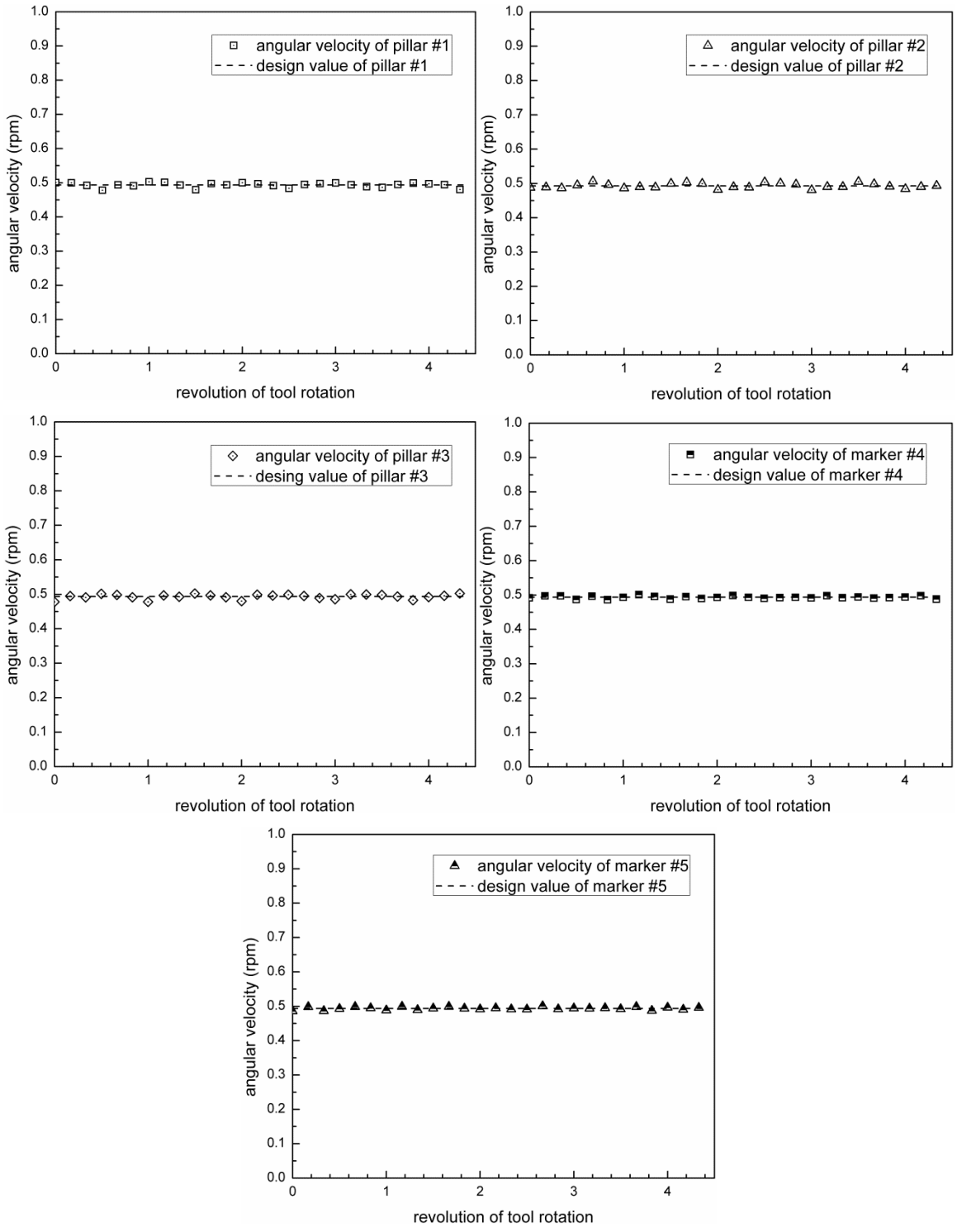


Figure 4.8 Experimentally measured velocities of pillars (#1-3) and markers (#4-5) on tool surface.

The magnitudes of the measured angular velocities are shown in Figure 4.8 when compared to the expected values for the given rotation speed (0.5rpm) and radial position. Table 4.2 shows the comparison of mean value of height, radial distance from center and angular velocities of all the marker lengths and independently measured values.

Table 4.2 comparison of mean values of particle tracking measurements and known independent values

| **Marker number** | | **#1** | **#2** | **#3** | **#4** | **#5** |
|---|---|---|---|---|---|---|
| **Mean value of measurement** | **Height (mm)** | 5.213 | 10.355 | 5.316 | 0.019 | -0.020 |
| | **Radius (mm)** | 9.997 | 10.143 | 10.095 | 14.295 | 14.163 |
| | **Velocity (rpm)** | 0.494 | 0.493 | 0.494 | 0.494 | 0.494 |
| **Known independent value** | **Height (mm)** | 5.222 | 10.378 | 5.330 | 0 | 0 |
| | **Radius (mm)** | 9.893 | 10.191 | 10.075 | 14.245 | 14.227 |
| | **Velocity (rpm)** | 0.497* | 0.497* | 0.497* | 0.497* | 0.497* |
| **Difference** | **Height (mm)** | 0.009 (0.17%) | 0.023 (0.22%) | 0.014 (0.26%) | -0.019 | 0.020 |
| | **Radius (mm)** | -0.104 (1.05%) | 0.048 (0.47%) | -0.020 (0.20%) | -0.050 (0.35%) | 0.064 (0.45%) |
| | **Velocity (rpm)** | 0.003 (0.60%) | 0.003 (0.60%) | 0.003 (0.60%) | 0.003 (0.60%) | 0.003 (0.60%) |

*---measured by photodiodes.

### 4.3.3 EXPERIMENTAL VALIDATION BY DIFFERENT MODEL FLUIDS

An additional series of validation experiments are performed. First a set of experiments are performed using the same general experimental set-up described in Section 4.3.1, replacing the viscous syrup with water. Secondly, an additional set of experiments is performed by removing the fluid and the window so that calibration and the experiments are performed in air without any model fluid or glass window. The comparison of heights, radial distance from center and angular velocities of all tracked markers of experimental measurements in syrup, water and only in air are presented in Figures 4.9, 4.10 and 4.11, respectively.

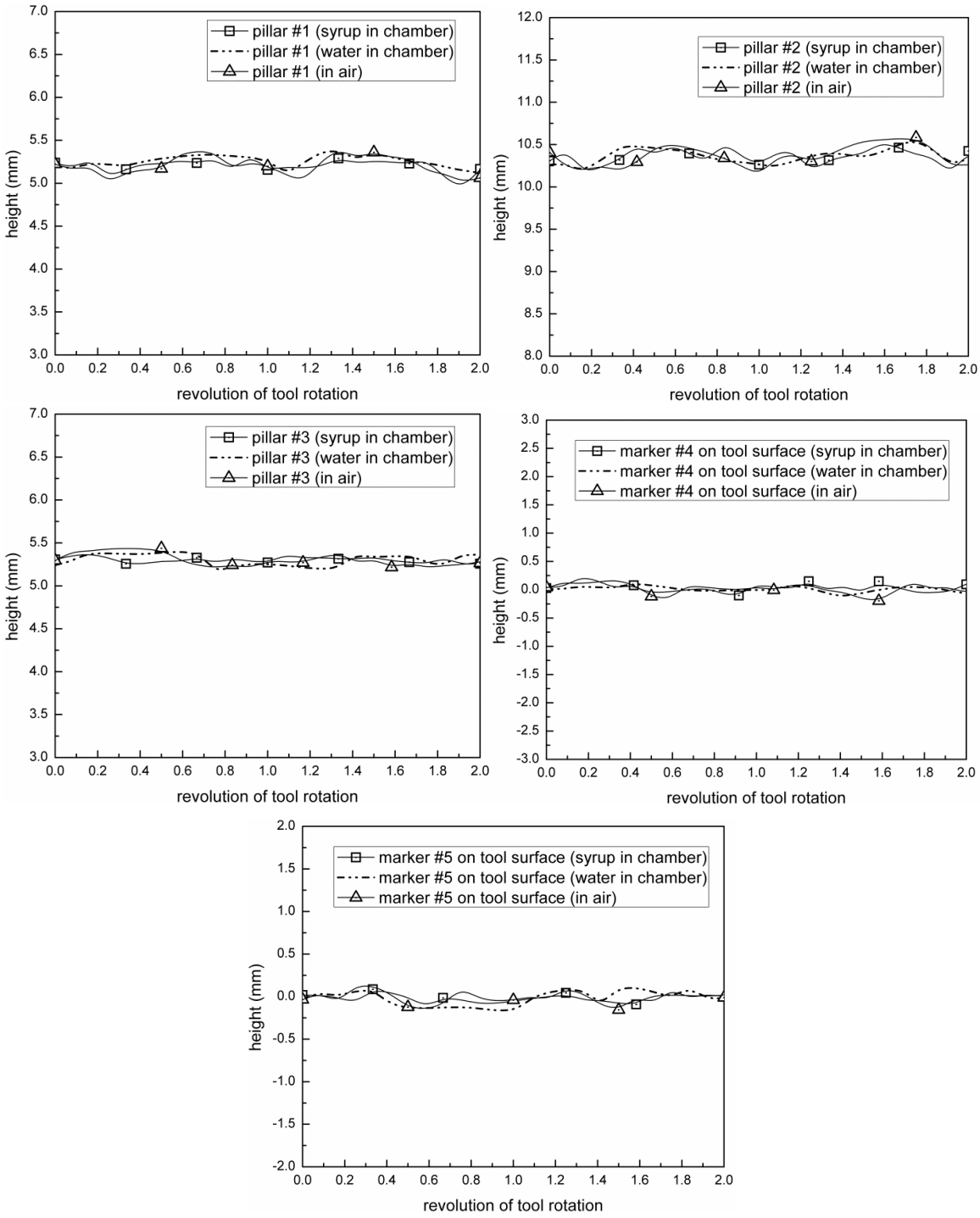


Figure 4.9 Comparison of experimentally measured heights of pillars and markers on tool surface immersed in syrup, water fluid (in chamber) and only in air vs. rotations of tool.

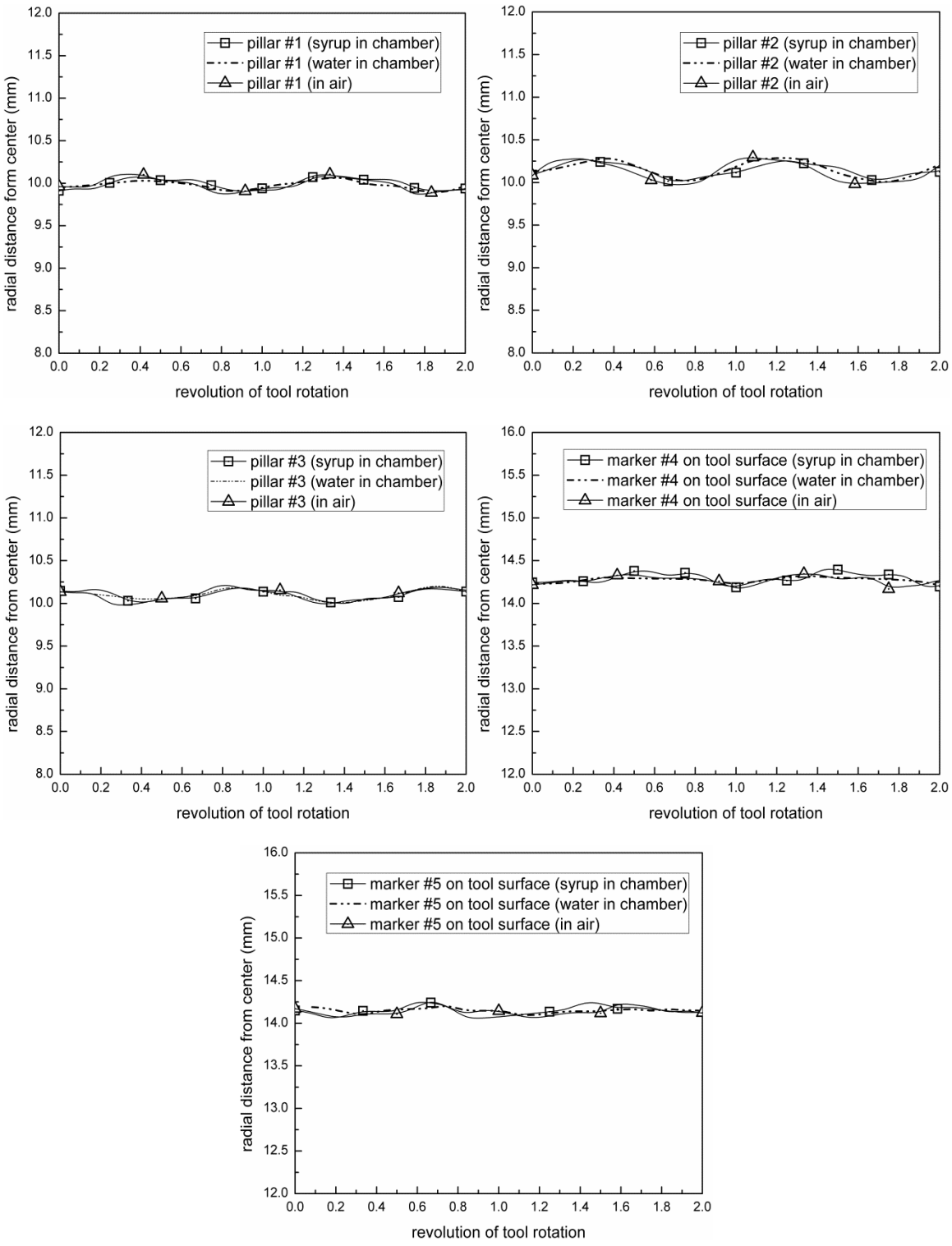


Figure 4.10 Comparison of measured radial positions of the pillars and markers on tool surface immersed in syrup, water fluid (in chamber) and only in air vs. rotations of tool.

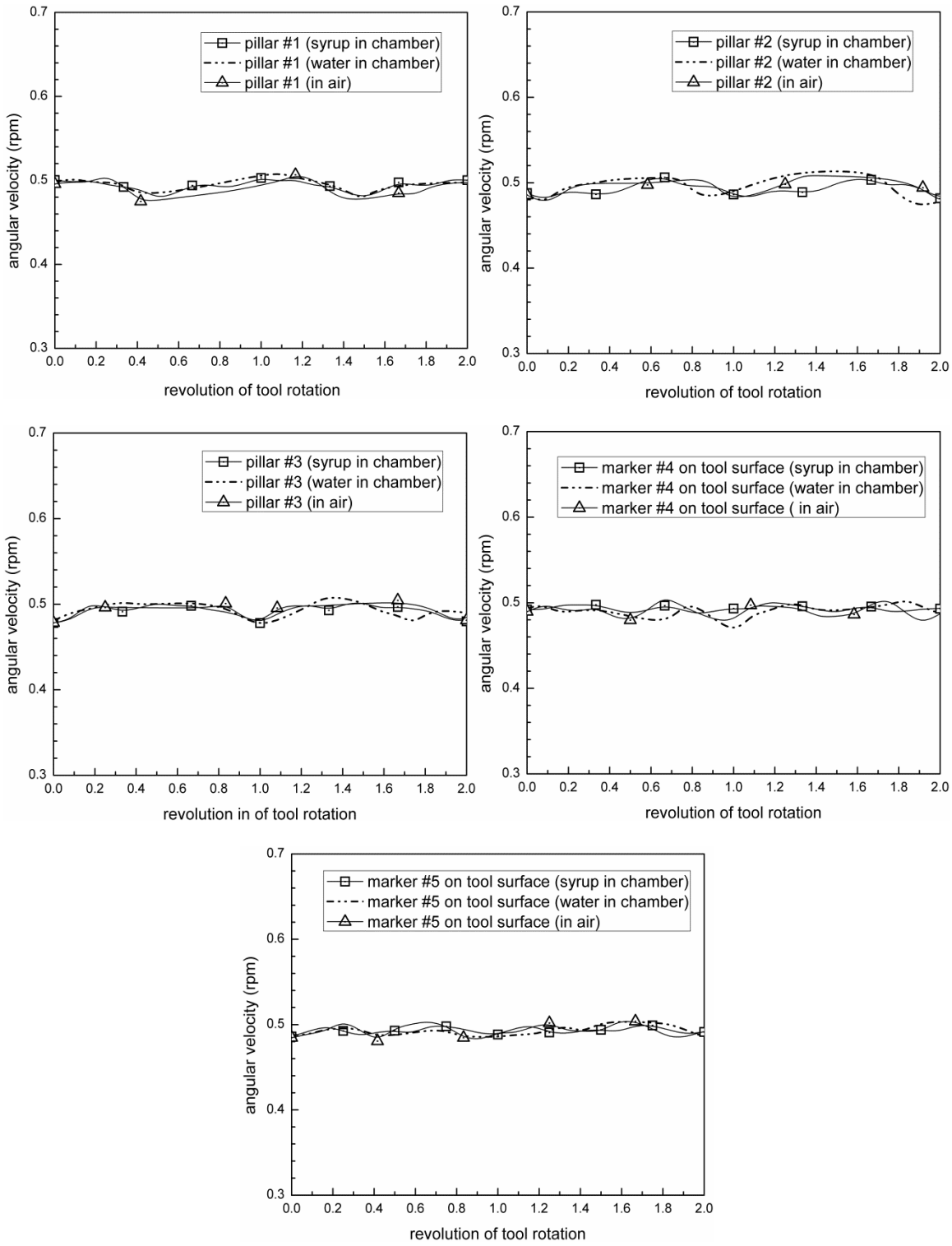


Figure 4.11 Comparison of measured tangential velocities of pillars and markers on tool surface immersed in syrup, water fluid (in chamber) and only in air vs. rotations of tool.

## 4.4 PARTICLE TRACKING MEASUREMENTS FOR FLUID ROTATION AND FLUID EXTRUSION PROCESSES

Friction extrusion was invented and patented at the Welding Institute Cambridge UK (Thomas 1993) in 1993 and subsequently largely ignored until the patent lapsed in 2002. There is limited literature involving the friction extrusion process (Tang 2010). Recently, the friction extrusion process is being developed and refined to demonstrate its potential for helping to decrease the waste that occurs during machining of parts by converting the waste metallic chips into wire product. As shown in Figure 4.12, the friction extrusion process is a friction based process which can produce high quality wire, rod, disk or fully consolidated bulk via consolidation and extrusion of recycling materials such as machining chips and low-cost titanium powder/chips (Zhang 2013). During the extrusion process, the extrusion die rotates about the extrusion axis and is compressed. At first, the billets will be consolidated under high pressure in the chamber. Then severe plastic deformation occurs in the billets and generates a large amount of heat which results in a temperature increase in the material. Significant temperature rises in the billet can be achieved solely by deformation heating rather than by external heating of the billet chamber, although external heating may also be utilized. Under high pressure, the metal will be extruded through the extrusion hole and form a wire or other products. To help extrude the metal, a scroll geometry may be used on the surface of the extrusion die that contacts with the billet charge. The friction extrusion process has the potential to be economical and "green", demonstrating the potential for creating high value products from low value input streams. Unfortunately, to date there has been limited success in extruding long sections of wire, most likely due to a lack of understanding of the transient material deformation processes that are occurring as wire is heated and extruded from the

billet chamber. To achieve high throughput and extrude large amounts of wire, the investigators proposed to develop both a computational extrusion model and perform experimental studies of the extrusion process to validate the simulation platform. Once validated, the extrusion simulations would be used to understand how various parameters in the process affect the extrusion flow fields and the quality of the extrudate.

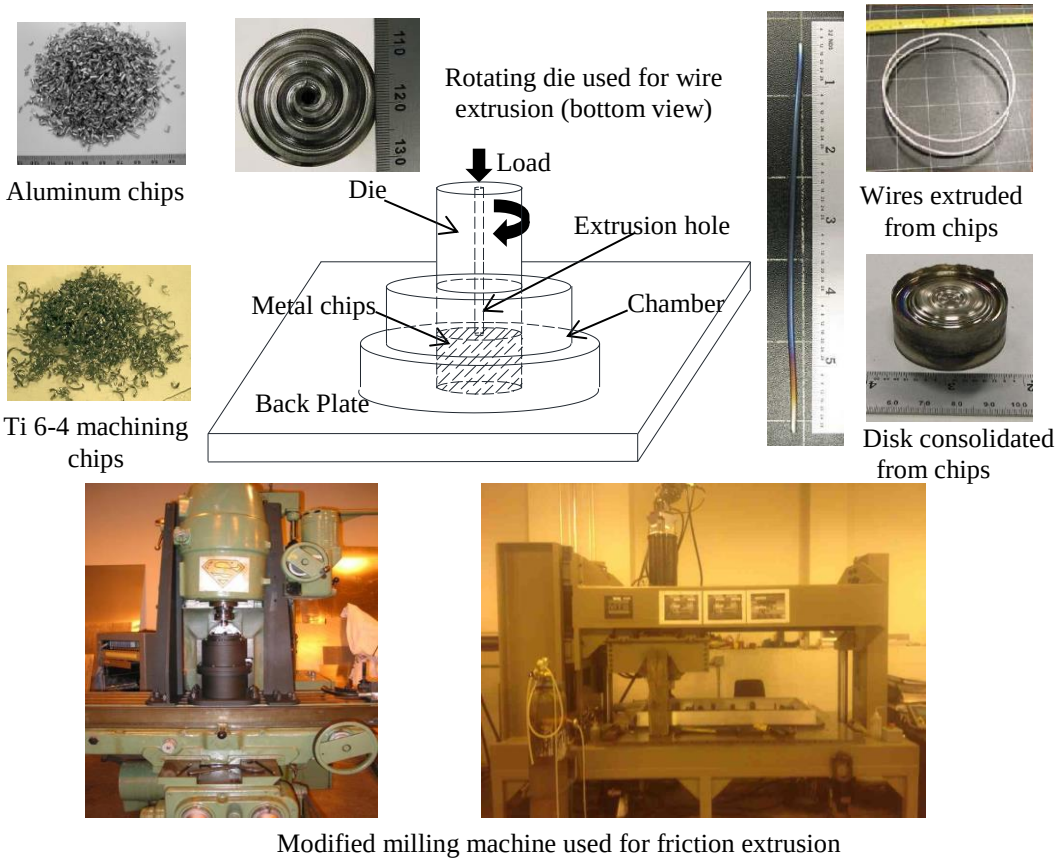


Figure 4.12 Photographs and schematics related to friction extrusion process.

### 4.4.1 LAB MODEL OF FRICTION ROTATION AND FLUID EXTRUSION PROCESS

The lab model described in Section 4.3.1 is further developed to try to experimentally visualize the friction extrusion process. For wire extrusion using aluminum chips (density $\rho$=2700kg/m$^3$), a typical die rotation rate N=250rpm, a chamber diameter of D=25.4mm (shown in Figure 4.12) and an estimated extrudate viscosity range from $\mu=10^5$---$10^7$Pa-s,

an estimate for the range of Reynolds numbers $2.28x10^{-6} < Re < 2.28 \times 10^{-4}$, where the highest value for Re corresponds to the least viscous region (i.e., hottest region) in the material. Since metal chips are initially consolidated, heated rotationally at high pressure and eventually "flowing out" through the extrusion hole, the lab experimental model uses a highly viscous fluid with nominally constant initial viscosity to provide experimental measurements of velocity field.

In this study, a transparent model fluid and a clear chamber are used to allow for observation of fluid motion outside the chamber. The chamber and fluid, shown in Figure 4.4, are the same as used in the validation experiments. Several neutrally buoyant particles are immersed in the fluid, traveling with the fluid as it is driven by rotation of the extrusion tool. The vision system shown at the bottom of Figure 4.4(e) is used to track the particles during the experiment. The investigators found that Karo syrup is a highly viscous clear fluid and candy "Sprinkles" are nearly ideal particles for the fluid extrusion studies. With syrup density $\rho = 1400 kg/m^3$, tool rotation rate N=0.5rpm, chamber diameter D= 38.1mm and room temperature viscosity $\mu$=5.78Pa-s, the nominal $Re = 9 \times 10^{-3}$ which is within one order of magnitude of the estimated viscosity of aluminum in the hottest region.

With regard to the particles used for tracking, "Sprinkle" particles are nearly spherical in shape and made from sugar, which is similar to the make-up of Karo syrup; their mass densities are nearly the same. In this work, the outside surface of sprinkles is painted black to (a) improve visibility when viewed against the white background of the upper rotation tool and (b) eliminate dissolution of the particle in the syrup fluid. By tracking the particles, the velocity distribution of fluid in the chamber could be obtained.

The tracked particles are distributed in syrup via two ways: (a) placing particles directly at the desired position in syrup and (b) adding particles in the reservoir and allowing them to flow into the chamber through a fluid inlet pipe.

### 4.4.2 PARTICLE TRACKING RESULTS: FLUID ROTATION, NO EXTRUSION

Particle motions in the syrup fluid are tracked by the stereo system using a set-up similar to the one shown in Section 4.3.1. A flat surface rotation tool without pillars is used in the fluid rotation experiments. The experimentally measurement for the particles and the comparison between measured velocity results for the particles and corresponding CFD simulations of the fluid motion are compared.

#### 4.4.2.1 PARTICLE TRACKING RESULTS OF FLUID ROTATION

Sprinkle particles are initially placed at multiple locations in the model syrup fluid and then tracked by two digital cameras fixed under the bottom of the acrylic block for stereo imaging while the tool rotates only. Figure 4.13 shows the 3D measured flow paths of several selected particles during fluid rotation. The plots on the left side in Figure 4.13 show the paths of the particles at multiple initial locations during the fluid rotation driven by the tool. The plots on the right side in Figure 4.13 show a top view of particle paths. The path of neutral buoyancy particles should form a circle when fluid rotation without extrusion is performed. The coordinates are the same as defined in Section 4.3.2 (shown in the Figure 4.4).

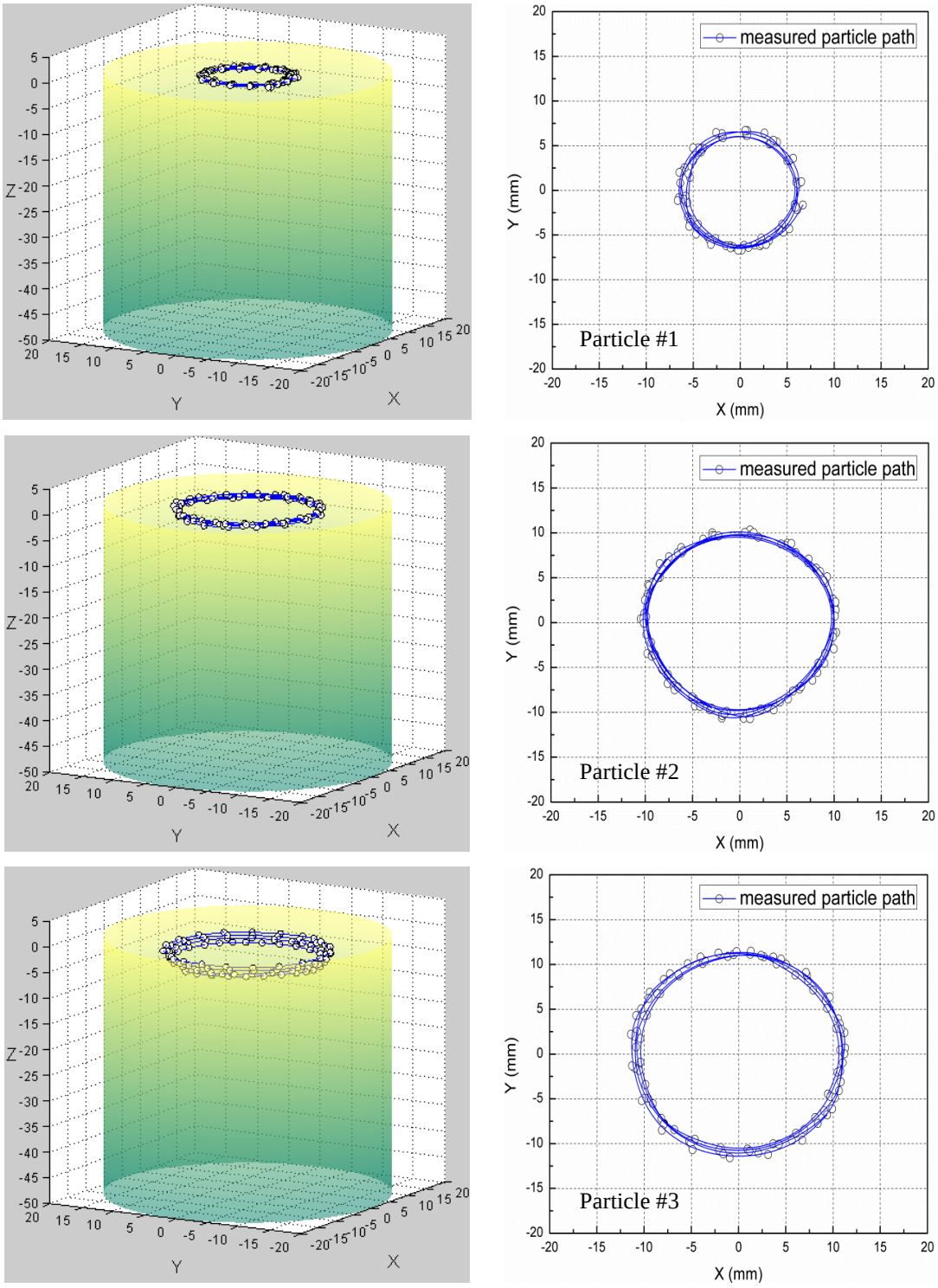


Figure 4.13 Flow paths of particles in fluid rotation (initial position of particles in fluid #1(H=0.889mm, R=5.318mm), #2(1.890mm, 10.493mm), #3(5.241mm, 10.461mm) H stands for height from X-Y plane in Z direction, R stands for radial distance from Z axis, Coordinate system is the same as defined in Section 4.3.2, shown in Figure 4.4).

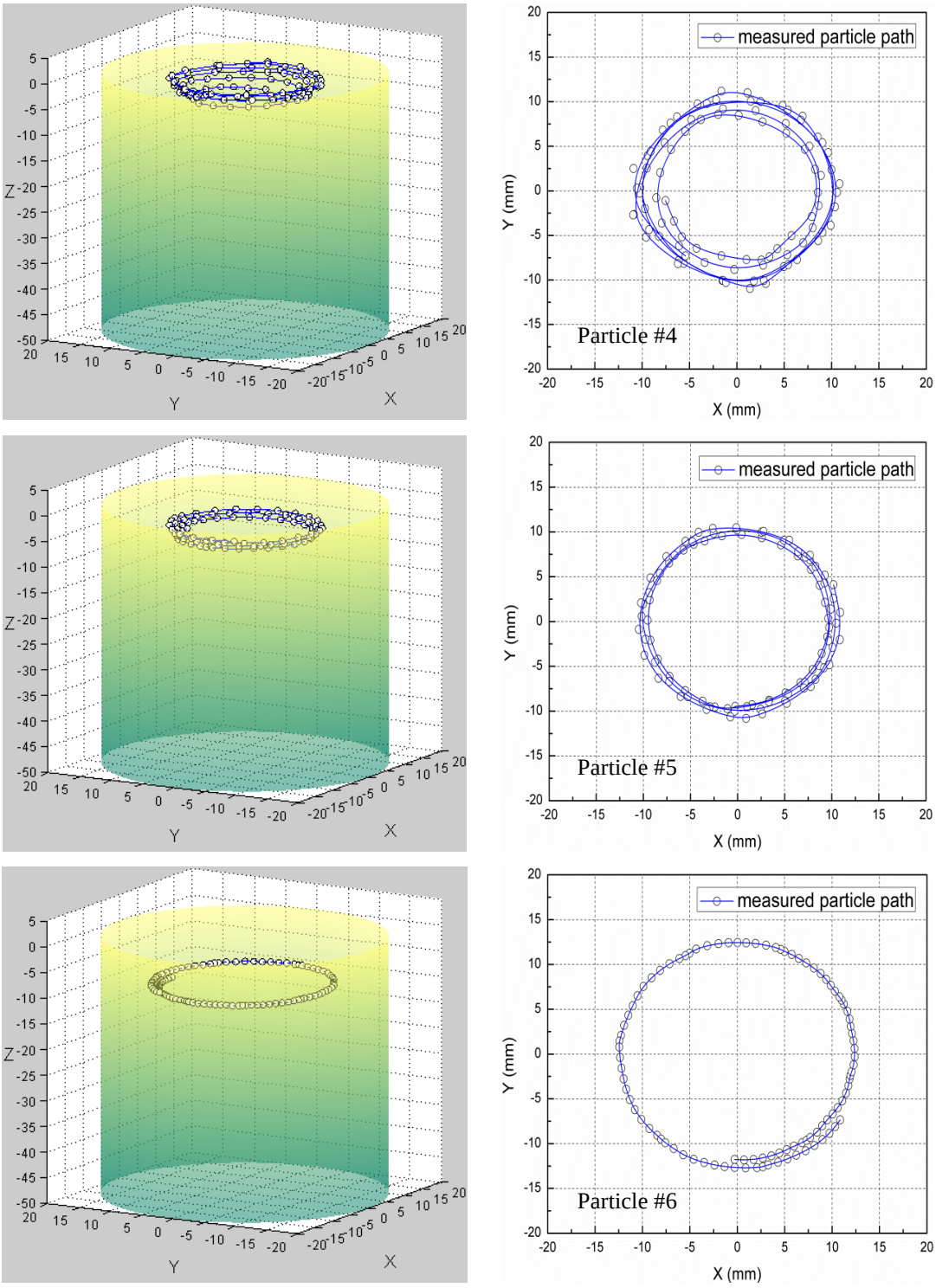


Figure 4.13 Flow paths of particles in fluid rotation (initial position of particles in fluid, #4(5.379mm, 7.617mm), #5(6.140mm, 9.466mm), #6(9.962mm, 11.767mm) H stands for height from X-Y plane in Z direction, R stands for radial distance from Z axis, Coordinate system is the same as defined in Section 4.3.2, shown in Figure 4.4) (cont′d).

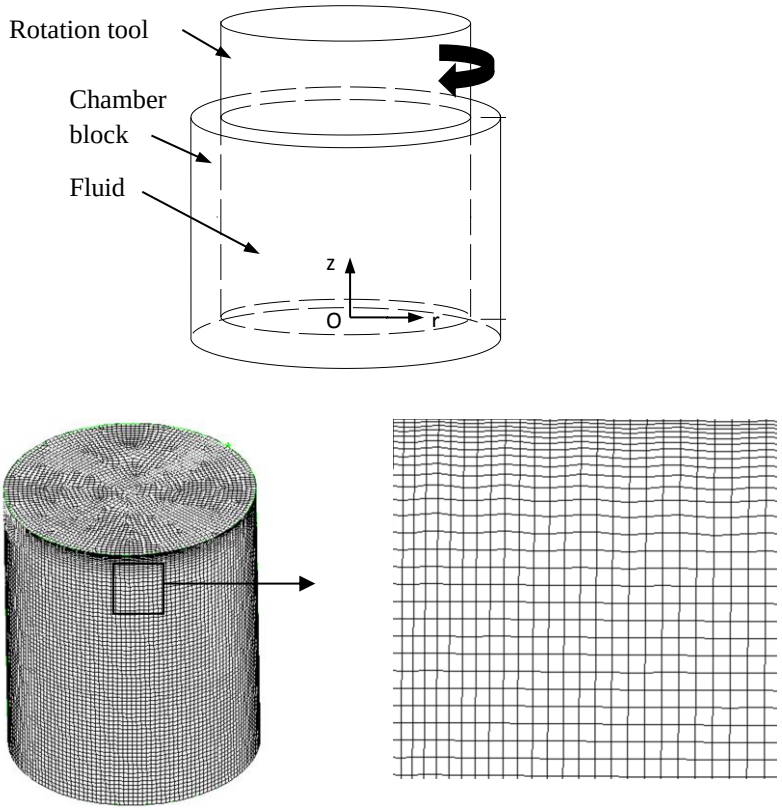


(a) (b)

Figure 4.14 Numerical model (a) grid and (b) details of mesh boundary layer.

#### 4.4.2.2 CFD MODEL OF FLUID ROTATION

Figure 4.14(top) shows a schematic diagram of the rotation only process. A cylindrical chamber is filled with a viscous model fluid. A cylindrical tool comes into contact at the top surface of the fluid. When the tool rotates at an angular speed of ω, the liquid at the contact interface will rotate at the same angular speed due to the viscous nature of the fluid, thus providing a no-slip contact boundary condition for the fluid volume at the contact interface. The numerical model shown in Figure 4.14 only considers the fluid motion due to tool rotation

The model fluid used is an incompressible and highly viscous Newtonian fluid with a constant viscosity μ. More details of the model fluid are described in Section 4.4.1.

Besides the no-slip boundary conditions at the tool fluid interface, the other boundary surfaces (the vertical cylindrical surface and the bottom surface) of the process chamber are also taken to have no-slip boundary conditions. As such, at the tool-fluid interface, the velocity boundary condition is that the velocity vector at a distance of r to the center point has a magnitude of ωr and is along the angular (tangential) direction, consistent with the rotation of the tool. At all other surfaces, all normal and tangential velocity components are zero.

#### 4.4.2.3 CFD SIMULATION PREDICTIONS AND EXPERIMENTAL MEASUREMENTS FOR FLUID ROTATION

The comparisons of CFD simulation predictions (Zhang 2013) and experimental measurements are shown in Figure 4.15. In Figure 4.15, the experimental measurements are from six marker particles (#1~#6 in the figures) that are tracked during the experiment. The positions of the particles are recorded every 5 seconds. The measured velocity varies with time due to the fact that during the experiment the particles oscillate vertically and radially.

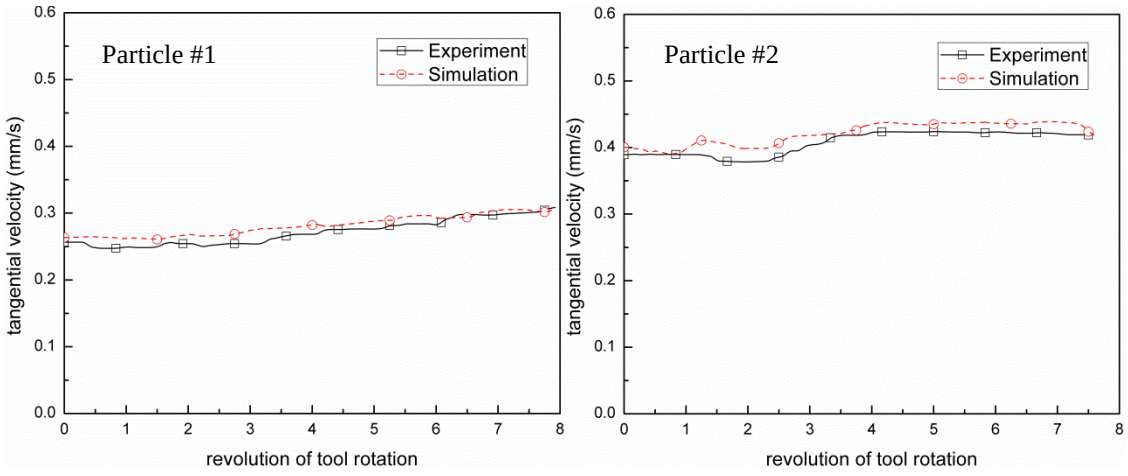


Figure 4.15 Comparison of experimental measurements and simulation results of the tangential velocity variation with revolution of tool rotation.

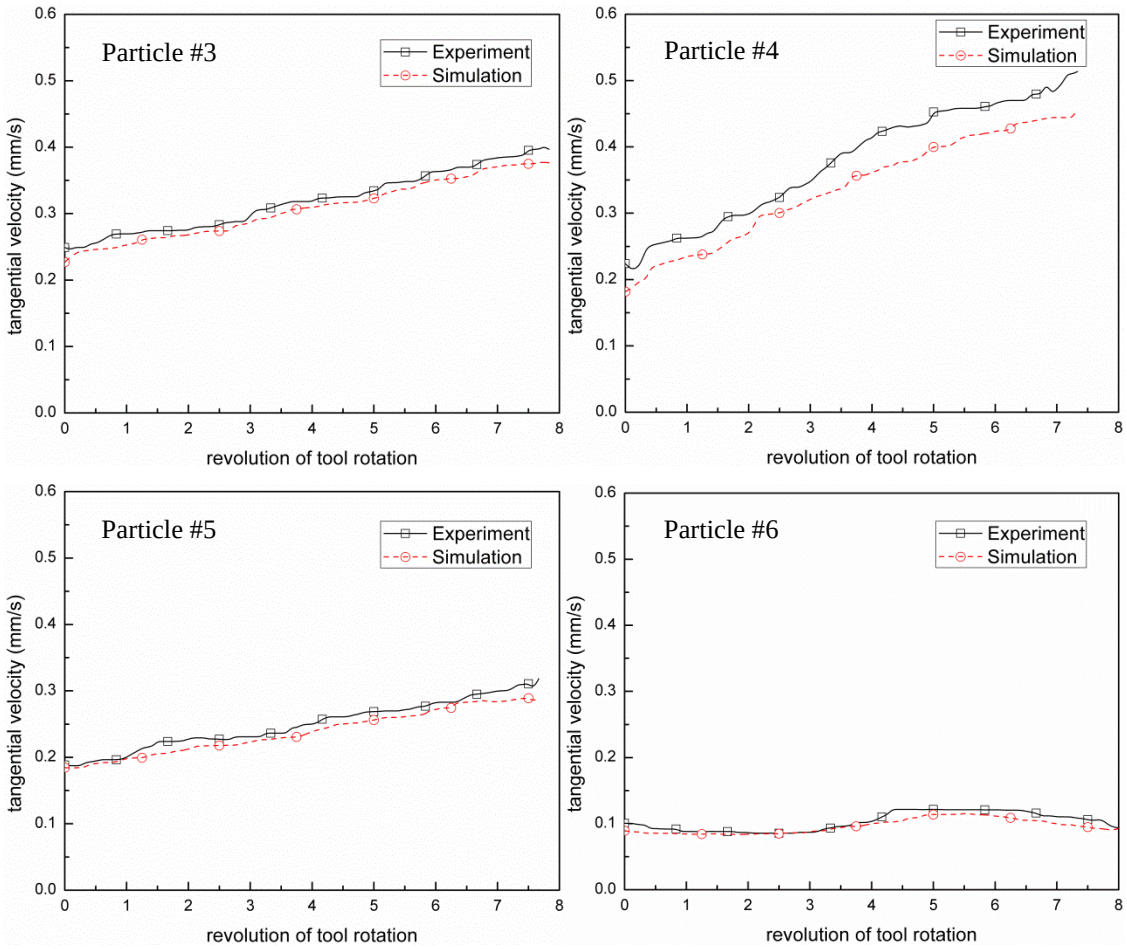


Figure 4.15 Comparison of experimental measurements and simulation results of the tangential velocity variation with revolution of tool rotation (cont′d).

It is seen from Figure 4.15 that the velocity values from the simulation and experimental measurements are very close. The qualitative trends are the same and the quantitative differences are small. Most of the quantitative differences are less than 10% in Figure 4.15. The main factors that may have contributed to the differences during experiments include the wobbling motion of the tool due to slight misalignment of the tool axis with the drive shaft. Nonetheless, the current comparisons between the simulation and experimental measurements show good agreement.

### 4.4.3 PARTICLE TRACKING RESULTS OF FLUID EXTRUSION PROCESS

Particle motions in the syrup fluid extrusion process are tracked by the stereo system

using a set-up similar to the one shown in Section 4.3.1 with some slight improvements. A flat surface rotation tool without pillars is used in the fluid extrusion process experiments. The experimentally measured motion results of particles and the comparison between measured motion results and the CFD simulation prediction for the fluid extrusion process are shown respectively.

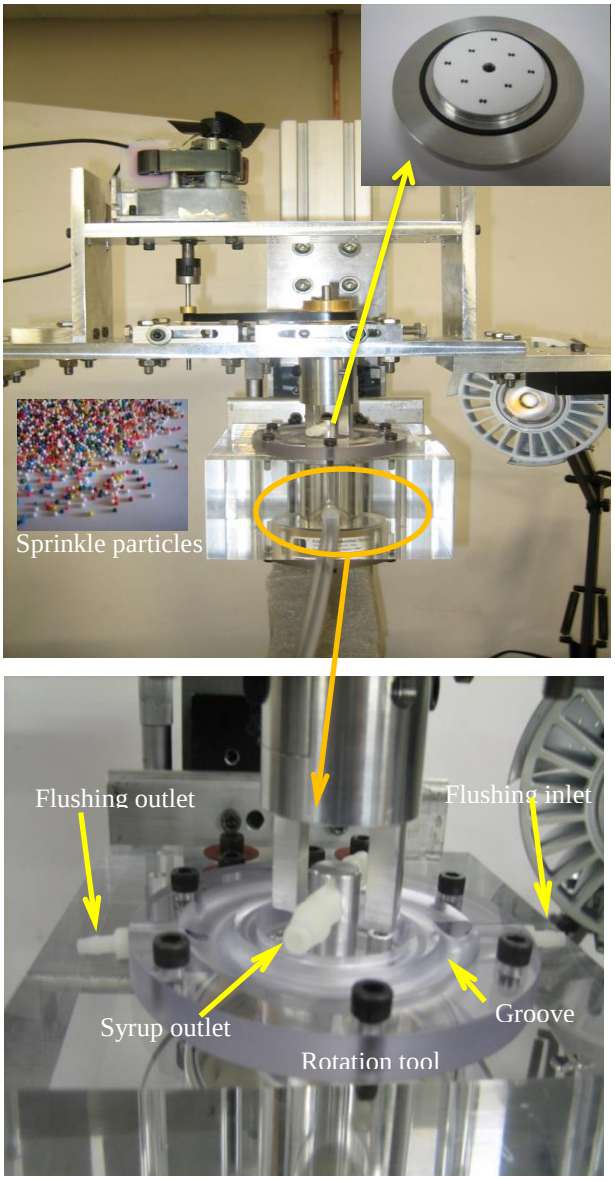


Figure 4.16 Photographs of water flushing configuration of syrup fluid extrusion. (Excess syrup exits through the syrup outlet and is entrained in the groove on the cover. Water is injected via the water inlet, washing the syrup out of the groove via the water outlet).

#### 4.4.3.1 PARTICLE TRACKING RESULTS OF FLUID EXTRUSION PROCESS

During the fluid extrusion process, fluid flows into the chamber through an inlet pipe which is connected to a fluid reservoir. Fluid is then extruded out from the center hole in the rotation tool while the upper tool is rotating. The speed of the fluid extruded out the upper orifice is controlled by maintaining the height of the fluid in the reservoir that is connected to inlet fluid pipe. As shown in Figure 4.16, a water-flushing inlet and outlet are located at the cover of the rotation tool for brushing away extruded syrup fluid.

Figure 4.17 shows the 3D measured flow paths of several arbitrarily selected particles. Particles #1-2 are initially distributed in fluid within the chamber and particles #3-5 enter the chamber via the inlet pipe. The plots on the left side in Figure 4.17 show the paths of the particles at multiple initial locations during the fluid extrusion process. The plots on the right side in Figure 4.17 show a top view of particle paths, where the vectors are the projections of the velocity vectors into the X-Y plane, which is the same coordinate system as defined in Section 4.3.2 and shown in Figure 4.4.

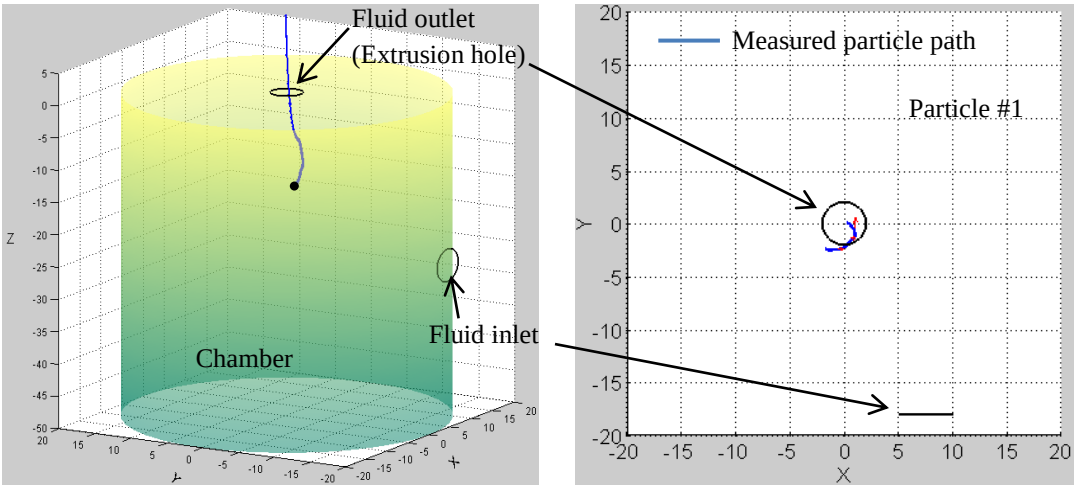


Figure 4.17 Flow paths of particles in fluid extrusion process.(initial position of particles in fluid #1(H=13.378mm, R=2.883mm), H stands for height from X-Y plane, R stands for radial distance to Z axis, Coordinate system is the same as defined in Section 4.3.2). Initial particle position is shown as "•" in photograph.

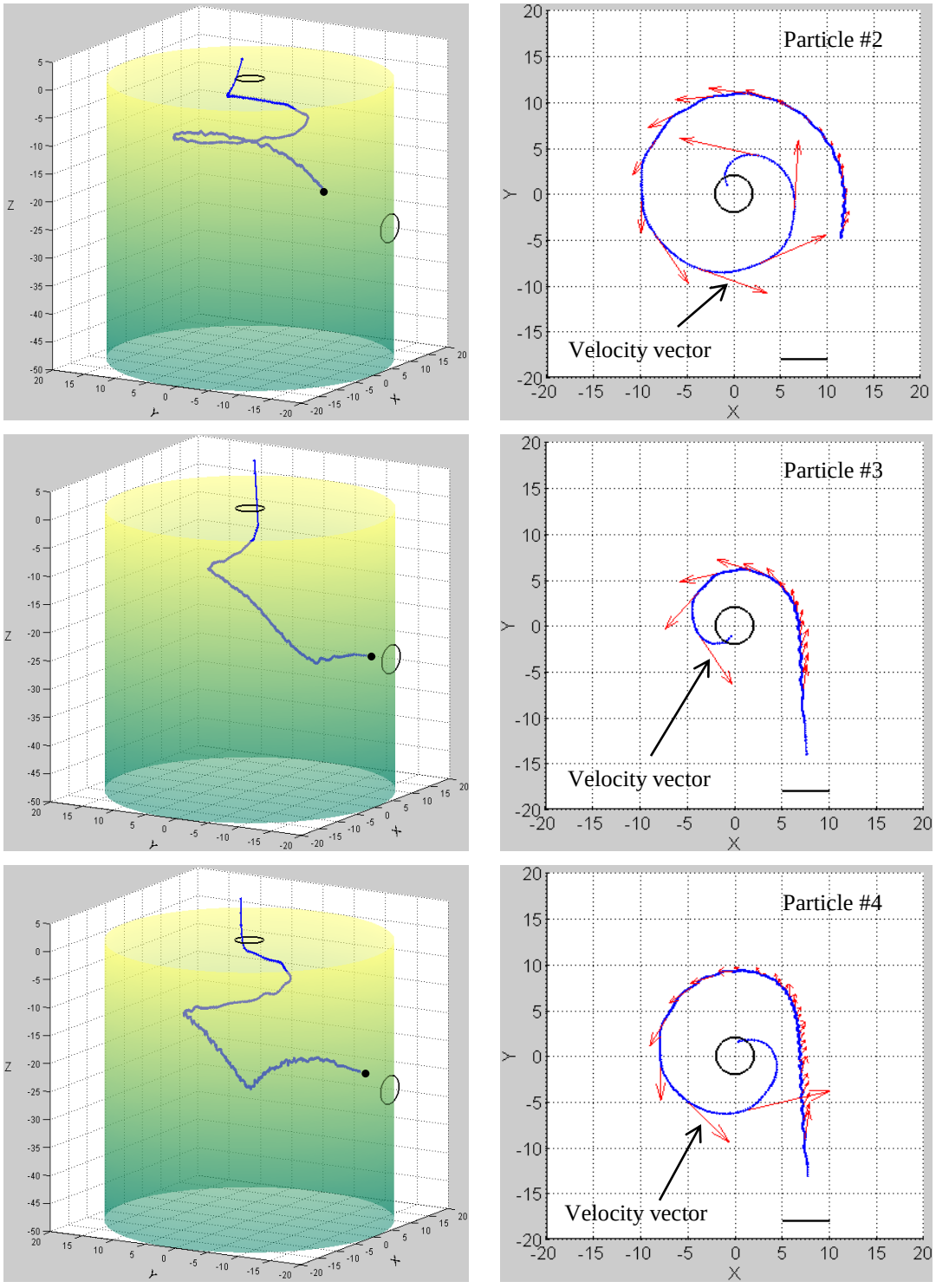


Figure 4.17 Flow paths of particles in fluid extrusion process.(initial position of particles in fluid #2(H=21.847mm, R=12.464mm), #3(H=25.999mm, R=15.940mm), #4(H=23.480mm, R=15.207mm), #5(H=24.726mm, R=14.934mm), H stands for height from X-Y plane, R stands for radial distance to Z axis, Coordinate system is the same as defined in Section 4.3.2). Initial particle position is shown as "•" in photograph (cont′d).

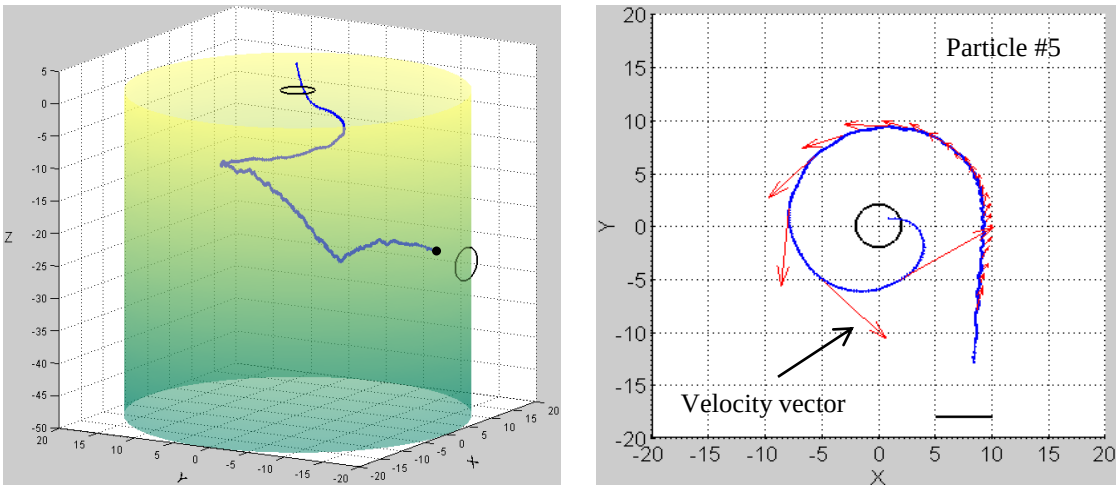


Figure 4.17 Flow paths of particles in fluid extrusion process.(initial position of particles in fluid #1(H=13.378mm, R=2.883mm), #2(H=21.847mm, R=12.464mm), #3(H=25.999mm, R=15.940mm), #4(H=23.480mm, R=15.207mm), #5(H=24.726mm, R=14.934mm), H stands for height from X-Y plane, R stands for radial distance to Z axis, Coordinate system is the same as defined in Section 4.3.2). Initial particle position is shown as "•" in photograph (cont′d).

#### 4.4.3.2 CFD MODEL OF FLUID EXTRUSION PROCESS

The fluid extrusion experiment process described in the previous sections has been simulated numerically using computational fluid dynamics. Particle flow in fluids has been studied widely in recent years, since particle motions are involved in many industrial sectors, such as pharmacy, food, and chemical. There are two categories of fluid flow models that are popular in studying particle fluid flows numerically: Eulerian-Eulerian and Eulerian-Lagrangian (Crowe 2012). The Eulerian-Eulerian approach treats both the particle and fluid as continuous phases which penetrate and interact with each other. The two phases are coupled by solving two sets of conservation equations with heat and momentum transfer. In the Eulerian-Lagrangian model, the fluid is treated as a continuum described by solving continuity and momentum equations, and the particles are treated as mass points and each of them is tracked by using Newton's equations of motion. One well-known model for tracking the particles is the Discrete Element Model

(Cundall 1979), which considers a finite number of particles behaving by means of contact and non-contact forces. The fluid phase and the particle phase are coupled together by heat and momentum transfer. The Eulerian-Lagrangian method has been recognized as an effective numerical tool to study the phenomena of different types of particle fluid flows, such as gas-solid fluidization (Xu 2012) and descending glass beads in water (Kawaguchi 1998).

For particle fluid flow with a very small volume fraction of particles in the fluid, the interaction between particles and the effect of particles on the fluid motion are oftentimes neglected in simulations without leading to significant errors, so that the particle motions are only driven by non-contact forces, such as drag force, virtual mass force, gravitational force, and other forces that are caused when a particle is moving in a fluid. The current work uses this model to investigate particle motion since the volume fraction of particles is negligible and there is no collision between the particles. The commercial code ANSYS FLUENT is used and the corresponding model employed in this paper is called the Discrete Phase Model. Since the temperature did not change much during the experiment, heat transfer is not considered in the model. Convergence analysis has been performed and converged simulation predictions have been obtained. The geometry and converged computational grid are shown in Figure 4.18. In order to capture the boundary layer near the wall, a finer mesh is used near the wall. Due to the geometry of the chamber, mixed cells (including tetrahedral, hexahedral, pyramidal, and wedge types) are used for the part near the inlet pipe, as seen in Figure 4.18 (b) & (c), and hexahedral cells are adopted for the rest. The maximum grid size is 1.0 mm and the minimum size is 0.2 mm. There are 10,5418 mixed cells and 41,566 hexahedral cells.

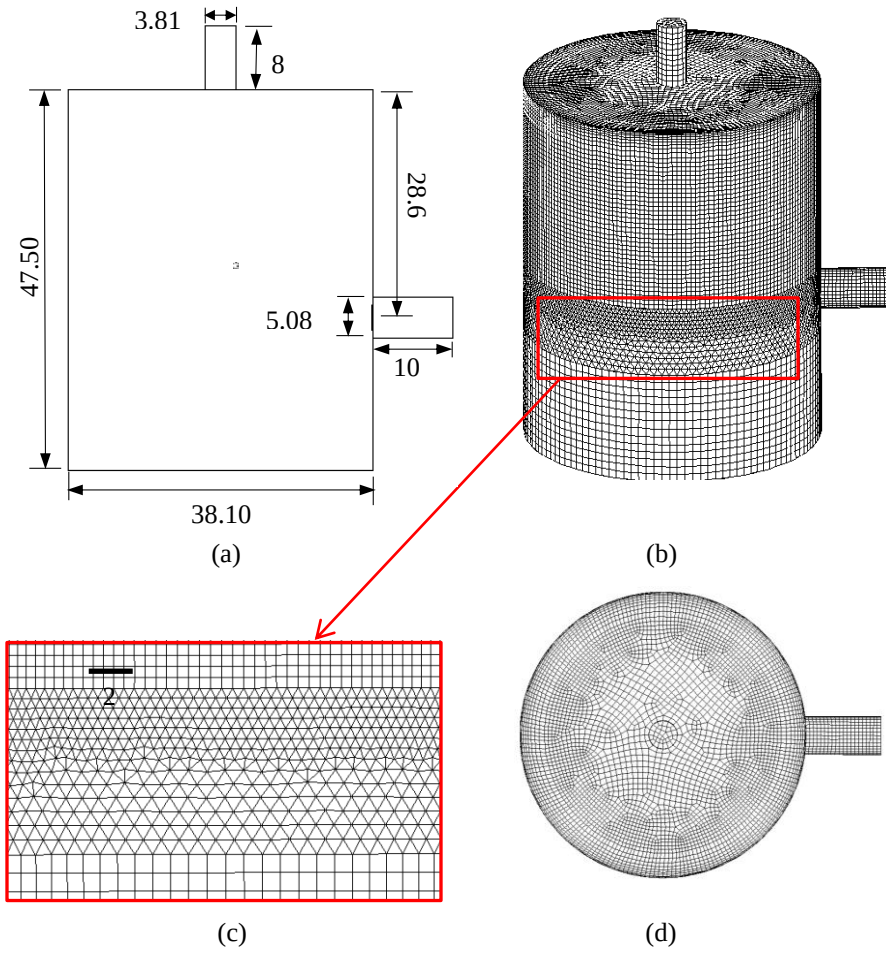


Figure 4.18 Geometry and converged grid of the CFD model: (a) model geometry and dimensions; (b) computational grid (the maximum grid size is 1.0 mm and the minimum size is 0.2 mm); (c) mixed grid volume including tetrahedral, hexahedral, pyramidal, and wedge types, the rest grid of chamber is hexahedral; (d) top view of the grid. Unite mm.

The fluid used in the experiment is syrup, which is assumed to be an incompressible, Newtonian fluid and very viscous compared with water. Since the Reynolds number is small, the flow is assumed to be laminar throughout the experiment. The fluid flow is simulated by solving the continuity equation and the Navier-Stokes equations which are given as follows:

Continuity equation

$$\nabla \cdot \boldsymbol{u} = \mathbf{0} \tag{4-5}$$

Navier - Stokes equations

$$\rho \frac{d\boldsymbol{u}}{dt} = -\nabla P + \mu \nabla^2 \boldsymbol{u} + \boldsymbol{F} \tag{4-6}$$

where $\boldsymbol{u}$ is fluid velocity vector, ρ is the density of the fluid, P is the pressure, μ is the viscosity, and **F** is the body force vector.

The trajectory of individual particles in the fluid is calculated by integrating the force balance on the particle in a Lagrangian reference frame. Ignoring particle collision forces, the force balance on a particle can be written as

$$\frac{d\boldsymbol{u_p}}{dt} = \boldsymbol{F_d} + \frac{\boldsymbol{g}(\rho_p - \rho)}{\rho_p} + \frac{\rho}{2\rho_p}\frac{d(\boldsymbol{u} - \boldsymbol{u_p})}{dt} + \frac{1}{\rho_p}\nabla(-P) \tag{4-7}$$

where $\boldsymbol{u_p}$ is particle velocity, $\boldsymbol{F_d}$ is drag force, $\boldsymbol{g}$ is gravitational acceleration, and $\rho_p$ is particle density. The second term on the right hand side is the gravitational force, the third one is designated the "virtual mass force", and the last one is the pressure force (Crowe 2012). Other forces, such as Saffman's lift force, Magus force, and Besset force, are considered negligible and thus are not included in the modeling. The drag force expression is given as (Ansys Mannual)

$$\boldsymbol{F_d} = \frac{18\mu}{\rho_p d_p^2}\frac{C_d R_e}{24}(\boldsymbol{u} - \boldsymbol{u}_p) \tag{4-8}$$

where $d_p$ is the particle diameter, and $R_e$ is the relative Reynolds number given by

$$R_e = \frac{\rho d_p}{\mu}\left|\boldsymbol{u} - \boldsymbol{u}_p\right| \tag{4-9}$$

$C_d$ is the drag coefficient. Since the particles used are spherical, the Spherical Drag Law is employed and the drag coefficient is taken by referring to reference (Morsi 1972). The "virtual mass force" term in Fluent accounts for entrainment of a small amount of fluid with the particle.

As noted previously, the viscosity and density of the fluid (syrup) are 5.78Pa-s (http://www.geology.um.maine.edu, Department of Earth Science, University of Maine)

and 1400kg/m$^3$, and are assumed to be constant throughout the experiment. The mass flow rate at the inlet is ~ 23.3g/s, according to experimental measurements. The contact between the fluid and the chamber walls is assumed to be modeled as a no-slip condition. After calculating the fluid flow for several minutes, the fluid flow has reached steady state and the particles with average 0.8 mm diameter and 1560kg/m$^3$ density are inserted into the fluid with initial velocity conditions obtained from experimental measurements for particles at the same position.

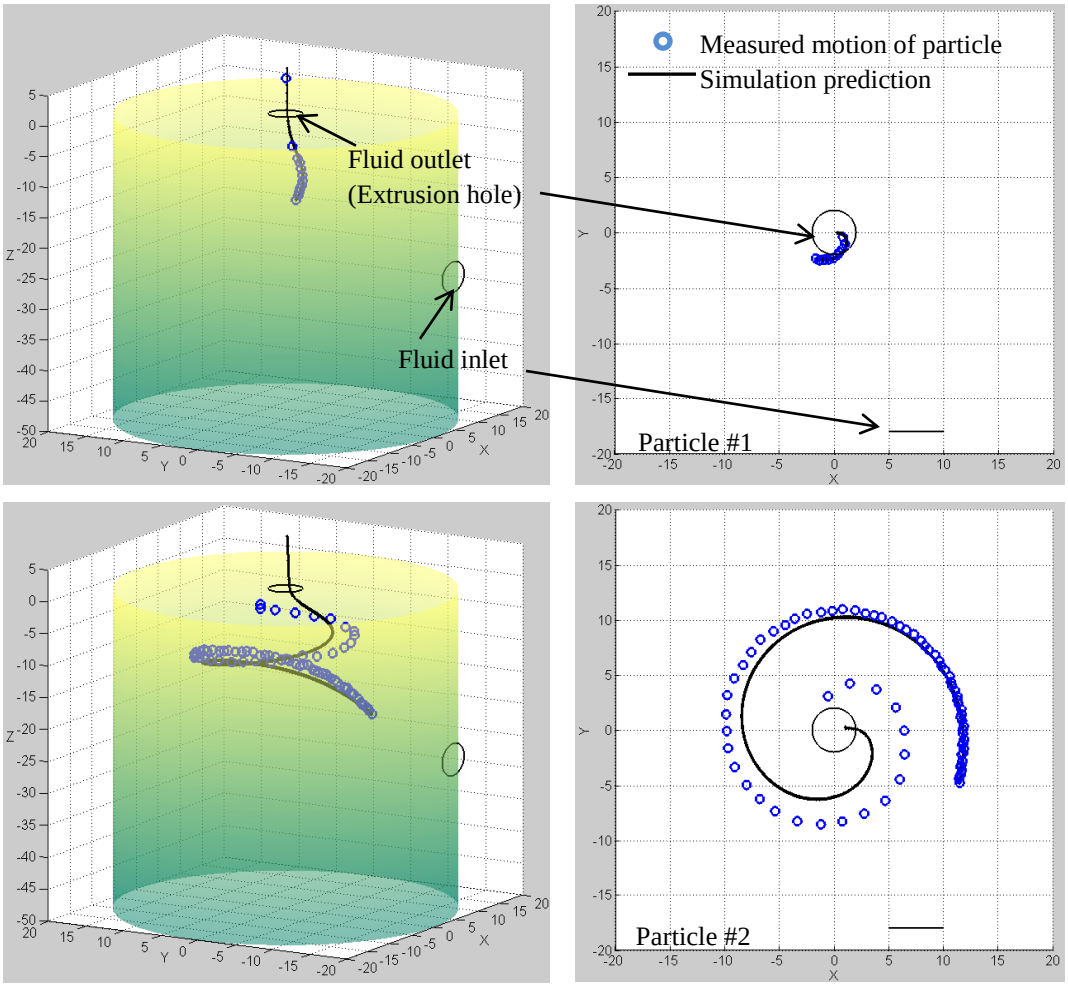


Figure 4.19 Comparisons of flow paths of particles measured in experiment of fluid extrusion process and predicted by CFD simulations. The initial 3D positions of the particles in fluid are #1(1.66, 2.35, 13.36), #2(-11.50, 4.79, 21.54), where the coordinate system is the same as defined in Section 4.3.2). All units on graph are in mm.

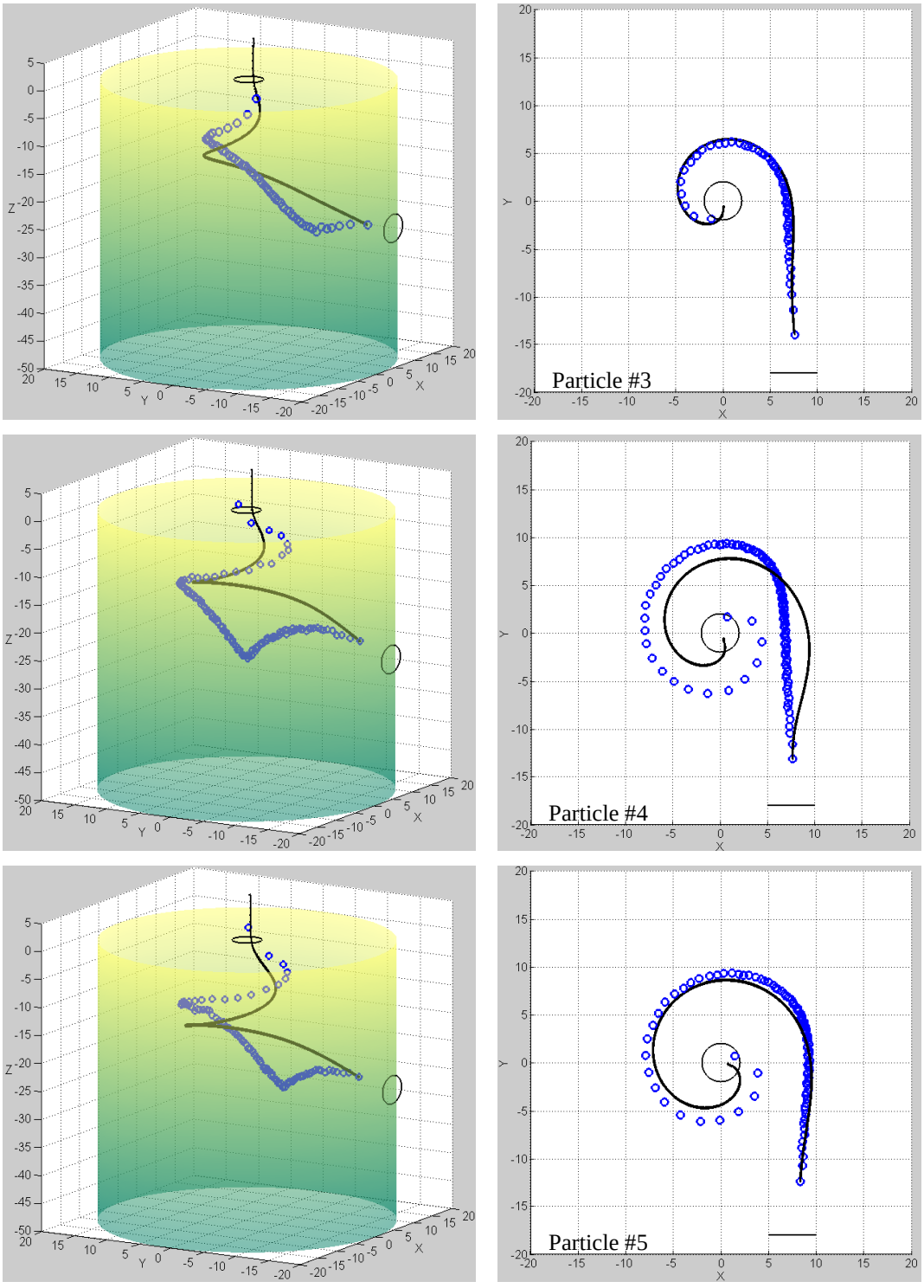


Figure 4.19 Comparisons of flow paths of particles measured in experiment of fluid extrusion process and predicted by CFD simulations. The initial 3D positions of the particles in fluid are #1(1.66, 2.35, 13.36), #2(-11.50, 4.79, 21.54), #3(-7.63, 13.99, 26.0), #4(-7.67, 12.13, 23.48) and #5(-7.29, 14.09, 25.49), where the coordinate system is the same as defined in Section 4.3.2). All units on graph are in mm (cont′d).

#### 4.4.3.3 CFD SIMULATION PREDICTIONS AND EXPERIMENTAL MEASUREMENTS FOR FLUID EXTRUSION PROCESS

The CFD simulations (Zhang 2013) and experimental measurements of particle tracking in fluid are shown in Figure 4.19. Initial positions of tracked particles are given in Figure 4.19 in the coordinate system defined in Section 4.3.2.

## 4.5 DISCUSSIONS

Careful examinations of Figures 4.5-4.8 and comparisons in Figures 4.9-4.11 show that, with every revolution of tool rotation, small oscillations occur periodically around the corresponding known value. These small oscillations are attributed to vibrations and non-coaxality of the motor and speed- reducing pulley system which drives the rotation tool. This effect is confirmed by using gauge dials mounted against the side of the rotation tool while it is rotating. Thus, the measurements are sufficiently accurate to quantify these small periodic oscillations. As shown in Figures 4.9-4.11, the small oscillations do not alter the excellent agreement between the independent measurements of the experimental results.

Figures 4.5-4.8 show excellent agreement between measurements in a fluid and its known value during tool rotation for the positions of all tracked markers. Table 4.2 indicates that the differences between measured mean values using the vision-based system and independent measurements are less than 1.05%.

Figure 4.9-4.11 shows the consistency of measurements in different model fluids. The measurements in water, syrup and air match very well with each other. The projection error defined by Equation (4) indicates that is the errors are less than 0.15 pixels in syrup and 0.08 pixels in water, confirming the capability to accurately measure motions of objects immersed in a fluid.

The numerical results shown in Figure 4.19 agree reasonably well with experimental measurements. The difference between numerical predictions and experimental measurements occurs during the early stage when particles come into the chamber from the fluid inlet pipe. The difference is attributed to the lack of data for accurate properties (viscosity and density depends on temperature gradient, velocity gradient, dehydration etc.) of the syrup fluid, and possibly the lack of "steady state" conditions throughout the volume, any one of which could lead to differences between the simulated flow field and the experimental measurements near the fluid inlet where the flow field is more complex.

## 4.6 CONCLUSIONS

The method proposed by Ke (Ke 2008) to correct for the effects of multiple refractions has been experimentally verified through a series of controlled baseline experiments. The results show that the proposed method is viable for accurate measurement of particle tracking in fluids using stereo vision systems. The validated approach has been used to measure the flow fields in a laboratory model of the friction extrusion process. Results from the experiments are found to be in good agreement with numerical simulations of the extrusion process, with the primary differences occurring near the particle inlet nozzle region where effects such as the presence of unsteady flow in the experiment or variations in viscosity are likely causes for the discrepancies.

Finally, the results confirm the viability of using such systems to make measurements in other important applications including (a) quantifying fluid motions on a large scale using multiple camera systems to expand measurement volume by increasing field of view and/or depth of field, (b) determining the deformations of

submerged objects subjected to blast or shock loading and (c) improving understanding of complex fluid-structure interactions through careful analysis of the deformations that occur in controlled fluid-structure environments.

## 4.7 SUMMARY

Optical refraction at interfaces is a common issue when viewing a submerged specimen through a transparent window. The distortions that are introduced during such imaging must be minimized when employing stereo-vision systems to make quantitative displacement and velocity measurements in fluids. In this study, an optical model with refraction at multiple media interfaces that was developed previously for digital image correlation measurements is employed for particle tracking in fluids. Consistent with the model, for the first time calibration and reconstruction processes are developed and demonstrated experimentally to be effective in removing distortions. To improve understanding of extrusion processes, a transparent small scale lab model extruder using a highly viscous fluid is designed and constructed for use with stereo-vision measurement systems. Through sparse seeding of the fluid with neutrally buoyant spherical particles, the 3D motions of the particles are measured during the extrusion process. Results confirm that the calibration-stereo imaging approach is viable for accurate particle tracking in fluids.

# CHAPTER 5

# FUTURE RESEARCH RECOMMENDATIONS

## 5.1 SAND BLAST STUDY

The following topics are recommended for future research:

(a) Investigate the effect of sand blast loading on the shape of the charge (cylindrical, sphere etc..), DoB, SoD, sand/soil properties etc. by using FEA to understand physical principles that are activated during sand blast loading, which would be helpful to improve scaling and acceleration mitigation design of vehicle structures. Furthermore, to validate numerical models, particle tracking of sand during the blast process would be a challenge for stereo-vision experiment techniques, such as DIC.

(b) Simulation of blast events attracts lots of interests from researchers. However, the dynamic responses of structures under blast loading are still under study, since there remains lack of sufficient information regarding material properties under high strain rate. In this regards, consider the Johnson-Cook model (Johnson and Cook 1983, Spranghers 2013). The key model parameters of material model and failure model are still not available for strain rate sensitive material subjected to explosive detonation.

(c) Perform experiments with this concept of polyurea applied directly to floorboard or frames with the goal of optimizing the thickness to minimize weight and

maximize mitigation effects on accelerations. As an example, such as tube compression with a thin outside coating of polyurea might be considered.

## 5.2 PARTICLE TRACKING AND APPLICATIONS TO FRICTION EXTRUSION

The following topics are recommended for future research:

(a) Development of a large scale measurement system for particle tracking by increasing the depth of field and/or angle of view and/or using multiple camera systems.

(b) Apply external heating scaled down from a real friction extrusion experiment to lab models for the fluid extrusion process to understand how heating of fluid affect flow process.

(c) For extensions of the friction stir based process, (e.g. friction consolidation, friction alloy wire extrusion/consolidation), additional experimental investigations are required to understand the fundamental processing issues and improve physics-based approaches for the optimization of the process.

# REFERENCES


Adrian, R.J. 1991. Particle imaging techniques for experimental fluid-mechanics, Annual Review of Fluid Mechanics 23:261-304.

Alves, M, Oshiro, R.E. 2006. Scaling the impact of a mass on a structure. Int. J Impact Eng. 32:1158-73.

ANSYS Inc., ANSYS FLUENT theory guide (release 13.0), SAS IP Inc., 2010.

Arizaga, R., Cap, N., Rabal, H., Trivi, M. 2010. Image distortion due to refraction by planar surfaces. European Journal of Physics. 31:115-127.

Bao, X.L., Li, M.G. 2011. Defocus and binocular vision based stereo particle pairing method for 3D particle tracking velocimetry, Optics and Laser in Engineering 19:623-631.

Benedetti, R. 2008. Mitigation of explosive blast effects on vehicle floorboard. MSc Thesis. University of Maryland. USA.

Beyer, H.A. 1992. Accurate calibration of CCD-cameras. Proceedings of the International Conference on Computer Vision and Pattern Recognition (CVPR'92) in Urbana-Champaign IL in June 96-101.

Bodner, S.R. and Symonds P.S. 1979. Experiments on visco-plastic response of circular plates to impulsive loading. J. Mech. Phys. Solids 27: 91-113.

Bridgman, P.W. 1949. *Dimensional analysis*. Yale University Press. New Haven, Connecticut.

Brodrick, T. 2010. Mitigation of Frame Acceleration Induced by a Buried Charge. MSc thesis, University of Maryland, USA.

Brown, J.L., Lechner, M. 1956. Acceleration and Human Performance; A Survey of Research. J. Aviat. Med. 27 (1): 32-49.

Budwig, R. 2004. Refraction index matching methods for liquid flow investigations, Exp. Fluid 17:350-355.

Chabai, AJ. 1926. Scaling dimensions of craters produced by buried explosives. J. Geophysical Res 70(20):5075-98.

Chabai, A.J. 1965. Scaling dimensions of craters produced by buried explosives. J. Geophysical Res 70 (20): 5075-5098.

Corkidi, G., Voinson, T., Taboada, B.I., Cordova M.S., Galindo E. 2008. Accurate determination of embedded particles within dispersed elements in multiphase dispersions, using a 3D micro-stereoscopic vision system. Chemical Engineering Science, 63:317-329.

Correlated Solution, Inc. 121 Dutchman Blvd, Columbia SC 29063.

Coz, J.L., Hauet, A., Pierrefeu, G., Dramais, G., Camenen, B. 2010. Performance of image-based velocimetry (LSPIV) applied to flash-flood discharge measurements in Mediterranean river, Journal of hydrology, 394(1-2):42-52.

Cranz, C., Lehrbuch der Ballistik. 1926. *Textbook of ballistics*. Springer Verlag, Berlin.

Crowe, C., Schwarzkopf, J., Sommerfeld, M., Tsuji, Y., Multiphase Flows with Droplets and Particles (second edition), CRC Press, 2012

Cundall, P.A., Strack O.D.L., A discrete numerical model for granular assemblies, Geotechnique 29:47–65, 1979

Department of Defense 1998. Crew Systems Crash Protection Handbook (JSSG-2010-7). Washington D.C.

Dramais, G., Coz, J.L., Camenen, B., Hauet, A. 2011. Advantages of a mobile LSPIV method for measuring flood discharges and improving stage-discharge curves, Journal of Hydro-environment Research, 5(4):301-312.

Duane, T. 1953. Preliminary investigation into the study of the fundus oculi of human subjects under positive acceleration. (Report No. NADC-MA-5303) Johnsville, PA: Naval Air Development Center.

Durst, F., Melling, A., Whitelaw, J.H. 1976. *Principles and practice of laser-Doppler anemometry*. London: Academic Press Inc.

Eiband, M. 1959. Human tolerance to rapidly applied accelerations: a summary of the literature. Cleveland, OH: Lewis Research Center.

Eppinger, et al, 1999. Development of improved injury criteria for the assessment of advanced automotive restraint systems-II. NHTSA, Nov.

Eppinger, et al, 2000. Supplement: Development of Improved Injury Criteria for the Assessment of Advanced Automotive Restraint Systems-II. NHTSA, March.

Florence, A.L. 1966. Clamped circular rigid-plastic plates under central blast loading. Int. J. Solids Structures 2: 319-335.

Fourney, W.L., Leiste, U., Bonenberger, R, Goodings, D. 2005. Mechanism of loading on plates due to detonation. Int. J. Blasting and Fragmentation 9(4): 205-217.

Fourney, W.L., Leiste, U., Bonenberger, R, Goodings, D 2006. Explosive impulse on plates. Int. J. Blasting and Fragmentation 9(1): 1-17.

Fourney, W.L., Leiste, U., Taylor, L. 2008. Pressures acting on targets subjected to explosive loading. Int. J. Blasting and Fragmentation 2: 167-187.

Fourney, W.L., Leiste, H.U., Hauck, A., Jung, D. 2010. Distribution of specific impulse on vehicles subjected to IED's. Proceedings of SEM Fall Conference, IMPLAST 2010 held in Providence RI.

Fox, D.M., Huang, X., Jung, D., Fourney, W.L., Leiste, U. and Lee, J.S. 2011. The Response of small scale rigid targets to shallow buried explosive detonations. Int. J. Impact Engineering 38: 882-891.

Fujita, I., Muste, M., Kruger, A. 1998. Large-scale particle image velocimetry for flow analysis in hydraulic engineering applications, Journal of Hydraulic Research, 36(3):397-414.

Ganapathisubramani, B., Longmire, E.K., Marusic, I., Pothos, S. 2005. Dual-plane PIV technique to determine the complete velocity gradient tensor in a turbulent boundary layer, Exp. Fluids, 39:222-231.

Gaydon, M., Raffel, M., Willert, C. 1997. Rosengarten M., Kompenhans J., Hybrid stereoscopic particle image velocimetry, Exp. Fluids 23(4):331-334.

Genson, K. 2006. Vehicle shaping for mine blast damage reduction. MSc Thesis, University of Maryland, USA.

Gibbings, J.C. 1982. A logic of dimensional analysis. Journal of Physics A: Mathematical and General. 15:1991-2002.

Gibbings, J.C. 1986. *The systematic experiments*. Cambridge University Press, Cambridge.

Goldsmith, W 1979. Some aspects of head and neck injury and protection. Progress in Biomechanics. 333-377.

Gupta, N.K., Nagesh 2007. Deformation and tearing of circular plates with varying support conditions under uniform impulsive loads. Int. J. Impact Engineering 34: 42-59.

Gurdjian, E. S., Lissner, H. R., Latimer, F. R., Haddad, B. F., Webster, J. E. 1953 Quantitative determination of acceleration and inter-cranial pressure in experimental head inury. Neurology, 3: 417-423.

Gurdjian, E. S., Roberts, V. L., Thomas, L. M. 1964, Tolerance curves of acceleration and inter-cranial pressure and protective index in experimental head injury. Journal of Trauma: 6: 600-604.

Gurdjian, E. S., Hodgson, V. R., Hardy, W. G., Patrick, L. M., Lissner, H. R. 1964, Evaluation of the protective characteristics of helmets in sports. Journal of Trauma, 4: 309-324.

Hargather, M.J., Settles, GS 2007. Optical measurement and scaling of blasts from gram-range explosive charges. Shock Waves 17: 215-223.

Head, H., 1920. The sense of stability and balance in the air. The Medical Problems of Flying. Oxford.

Heikkil, J. 2000. Geometric camera calibration using circular control points. Pattern Analysis and Machine Intelligence 22(10):1066-1077.

Helm, J.D., McNeil, S.R., Sutton, M.A. 1996. Improved 3D image correlation for surface displacement measurement, Optical Engineering 35: 1911-1920.

Hobson, P.R., Watson, J. 1999. Accurate three-dimensional metrology of underwater objects using replayed real images from in-line and off-axis holograms. Meas. Sci. Technol., 10:1153-1161.

Hopkinson, B. 1915. British Ordonance Board Minutes 13565.

Hopkins, L.M., Kelly, J.T., Wexler, A.S. 2000. Particle image velocimetry measurement in complex geometries. Experiments in Fluids. 29: 91-95.

http://www.geology.um.maine.edu/,Ultra high pressure metamorphic terrance development an analog modeling study, Charles Rodda, Department of Earth Science, University of Maine.

Hu, H., Saga, T., Kobatashi, T., Taniguchi, N., Yasuki M. 2001. Dual-plane stereoscopic particle image velocimetry: system set-up and its application on a lobed jet mixing flow, Exp. Fluids 31: 277-293.

Hudson, G.E. 1950. A theory of the dynamic plastic deformation of a thin disphragm. Journal of Applied Physics 22(1):1-11.

Hurley, R., 2011. Mitigating acceleration of vehicle structures impacted by explosive detonation, Msc Thesis, University of Maryland.

Hutchinson, J., Kaiser, M. J., Lankarani, H. M. 1998. The Head Injury Crtiterion (HIC) functional. Applied Mathematics and Computation 96:1-16.

Jacob, N., Chung, K.Y.S., Nurick, G.N., Bonorchis, D., Desai, S.A., Tait, D. 2004. Scaling aspect of quadrangular plates subjected to localized blast loads-experiments and prediction Int. J. Impact Eng. 30:1179-1208.

Jacob, N., Nurick, G.N., Langdon G.S. 2007. The effect of stand-off distance on the failure of fully clamped circular mild steel plate subjected to blast loads. Engineering Structures. 29: 2723-2736.

Johnson W. 1972. *Impact strength of materials*. Edward Arnold.

Johnston, W., Dybbs A. Edwards, 1975. Measurement of fluid velocimetry inside porous media with a laser anemometer, Phys Fluids 18(7): 913-914.

Johnson, G.R., Cook, W.H., 1983. A constitutive model and data for metals subjected to large strains, high strain rates and high temperatures. Proceedings of the Seventh International Symposium on Ballistics. 541-547, The Hague, Netherlands.

Jones, N. 1989. *Structural impact*. Cambridge University Press. New York.

Kantoush, S.A., Anton, J.S., Tetsuya, Sumi, Mitsuhiro, Murasaki, 2011. LSPIV implementation for environmental flow in various laboratory and field cases. Journal of Hydro-environment Research, 5(4):263-276.

Kähler, C.J., Kompenhans, J. 2000. Fundamentals of multiple plane stereo particle image velocimetry, Exp. Fluids, Suppl. pp. S70-S77.

Kawaguchi, T., Tanaka T., Tsuji Y. 1998. Numerical simulation of two-dimensional fiuidized beds using the discrete element method (comparison between the two- and three-dimensional models), Powder Technology 96: 129-138.

Ke, X., Sutton, M.A., Lessener, S. and Schreier, H.W. 2008. Robust stereovision and calibration methodology for accurate 3D digital image correlation measurements on submerged objects, J. Strain Anal. Eng. Des. 43: 689-704.

Kempinski, B., Murphy, C. 2012. Technical challenges of the US Army's Ground Combat Vehicle Programe. Congressional Budget Office, Washington D.C.

Kim, H., Lee, S. 2002. Performance improvement of two-frame particle tracking velocimetry using a hybrid adaptive scheme. Measurement Science and Technology, 13(4):519-534.

Kim, Y. 2006, Uncertainty analysis for non-intrusive measurement of river duscharge using image velocimetry. Ph.D. Thesis, The University of Iowa, Iowa, United States.

Kwon, Y.H. 1999. Object plane deformation due to refraction in two-dimensional underwater motion analysis. Journal of Applied Biomechanics, 15:396-403.

Kyme, A., Meikle, S., Baldock, C., Fulton, R. 2012 Refraction-compensated motion tracking of unrestrained small animals in positron emission tomography, Medical Image Analysis, 16:1317-1328.

Larmore, L. 1965. *Introduction to photographic principles*. New York: Dover Publications, Inc.

Lawrence, R.W. 1944. Mechanism of detonation in explosives. J. General and Applied Geophysics 9: 1-18.

Li, D.X., Zhong, Q., Yu, M.Z., Wang, X.K. 2008. Large-scale particle tracking velocimetry with multi-channel CCD cameras, International Journal of Sediment Research, 28:103-110.

Lobutova, E., Resagk, C., Putze, T. 2010. Investigation of large-scale circulations in room air flows using three-dimensional particle tracking velocimetry, Nuilding and Environment, 45:1653-1662.

Luo, P.F., Chao, YJ, Sutton, M. A., Peters, W.H. III 1993. Accurate measurement of three-dimensional deformations in deformable and rigid bodies using computer vision. Experimental Mechanics 33: 123-133.

Maas, H-G, Gruen, A., Papantomiou, D. 1993. Particle tracking velocimetry in three-dimensinal flows. Part I, Exp. Fluid 15:133-146.

Malik, N.A., Dracos, T., Papantomiou, D. 1993. Particle tracking velocimetry in three-dimensional flows Part II., Exp. Fluid 15:279-297.

Marjoux, D., Baumgartner, D., Deck, C., Willinger, R. Head injury prediction capability of the HIC, HIP, SIMon and ULP Criteria. Accident Analysis and Prevention. 40:1135-1148.

IED protected Vehicles Design Principles. Defense Update, 2007. http://www.defense-update.com/features/du-3-04/vehicle-protectiondesign.htm.

Moore, K.D. 2001. Intercalibration method for underwater three-dimensional mapping laser line scan systems. Applied Optics, 40(33):5991-6004.

Morsi, S.A., Alexander A.J. 1972. An Investigation of Particle Trajectories in Two-Phase Flow Systems, J. Fluid Mech. 55: 193–208.

Muste, M., Ho, H-C., Kim, D. 2011. Considerations on direct stream flow measurements using video imagery: Outlook and research needs. Journal of Hydro-environment Research, 5(4):289-300.

Muste, M., Xiong, Z., Schone, J., Li, Z. 2004. Flow diagnostic in hydraulic modeling using image velocimetry. Journal of Hydraulic Engineering, 130(3):175-185.

Neuberger, A, Peles, S, Rittel, D. 2007. Scaling the response of circular plates subjected to large and close-range spherical explosions Part I: Air-blast loading. Int J Impact Eng 34:859–73.

Neuberger, A, Peles, S, Rittel, D. 2007. Scaling the response of circular plates subjected to large and close-range spherical explosions Part II: Buried charges. Int J Impact Eng 34:874-82.

Neuberger, A, Peles, S, Rittel, D 2009. Springback of circular clamped armor steel plates subjected to spherical air-blast loading. Int. J. Impact Engineering 36: 53-60.

Nurick, GN, Shave, GC. 1995. The deformation and tearing of thin square plates subjected to impulsive loads-an experimental study. Int J. Impact Eng 18(1):99-116.

Nurick, GN, Martin, JB. 1989. Deformation of thin plates subjected to impulsive loading-a review. Part II: experimental studies. Int J Impact Eng 8(2):171–86.

Nurick, GN, Shave, GC 1995. The deformation and tearing of thin square plates subjected to impulsive loads-an experimental study. Int. J. Impact Engineering 18(1): 99-116.

Nurick, GN, Martin, JB 1989. Deformation of thin plates subjected to impulsive loading-a review. Part II: experimental studies. Int. J Impact Engineering 8(2):171–86.

Olson, M.D., Nurick G.N. and Fagnan J.R. 1993. Deformation and rupture of blast loaded square plates-predictions and experiments. Int. J. Impact Engineering 13(2): 279-291.

Peters, W. H., Ranson, W. F. 1981. Digital imaging techniques in experimental stress analysis. Opt. Eng. 21: 427-31.

Plakas, K., Trucco, E., Fusiello, A. 1998. Uncalibrated vision for 3D underwater applications. Oceans' 98 Conference Proceedings, 28(1):272-276.

Prasad, A.k., Adrian, RJ. 1993. Stereoscopic particle image velocimetry applied to liquid flows. Exp. Fluids 15:49-60.

Raffel, M., Willert, C., Werely, S., Kompenhans, J. 2007. *Particle image velocimetry: a practical guide*. Berlin, Heidelberg, New York: Springer.

Raffel, M., Kost, F. 1998. Investigation of aerodynamic effects of coolant ejection at the trailing edge of a turbine blade model by PIV and pressure measurements, Experiments in Fluids, 24:447-461.

Rimoli, J.J., Talamini B., Wetzel J.J., Dharmasena K.P., Radovitzky R. and Wadley HNG 2011. Wet-sand impulse loading of metallic plates and corrugated core sandwich panels. Int. J. Impact Engineering 38: 837-848.

Schleyer, G.K., Hsu S.S., White M.D., Birch R.S. 2003. Pulse pressure loading of clamped mild steel plates. Int. J. Impact Engineering 28: 223-247.

Schleyer, GK, Lowak, MJ, Poleyn, MA, Langdon, GS 2007. Experimental investigation of blast wall panels under shock pressure loading Int. J. Impact Engineering 34:1095-1118.

Snyman, I.M. 2010. Impulsive loading events and similarity scaling. Engineering Structures 32: 886-896.

Soloff, S. M., Adrian, R. J., and Liu, Z. C. 1997. Distortion compensation for generalized stereoscopic particle imaging velocoimetry. Measurement of Science and Technology 8:1441–1454.

Spranghers, K., Vasilakos I., Lecompte D., Sol H., Vantomme J., 2013. Numeical simulation and experimental validation of the dynamic response of aluminum plates under free air explosions. International Journal of Impact Engineerin 54: 83-95.

Stoll, A. 1956. Human tolerance to positive G as determined by the physiological end points. J. Aviat. Med. 27 (4): 356-67.

Stech, E., Payne, P. 1969. Dynamics of the human body (AD701383). Englewood CO: Froster Engineering Development Corporation.

Sutton, M. A., Bruck, H. A., McNeil, S. R. 1989. Determination of deformations using digital correlation with the Newton-Raphson method for partial differential corrections. Exp. Mech. 29: 261-267.

Sutton, M.A., Cheng, M, Peters, W.H., Chao, YJ, McNeil, S.R. 1986. Application of an optimized digital correlation method to planar deformation analysis. Image and Vision Computing 4(3):143-50.

Sutton, M.A., McNeil, S.R., Helm, J.D., Schreier, W.H., Chao, YJ. 2000. Advances in 2D and 3D computer vision for shape and deformation measurement. P. K. Rastogi, ed. Topics in Applied physics. Springer Verlag 77:323-372.

Sutton, M.A., Orteu, J-J, Schreier, H.W. 2009. *Image correlation for shape, motion and deformation measurements: basic concepts, Theory and Applications*. ISBN 978-0-387-78746-6 Springer.

Sutton, M.A., Orteu, J., Schreier, H. 2009 *Image correlation for shape, motion and deformation measurements.* Springer Science+Business Media, LLC, New York, NY.

Sutton, M.A., McFadden, C. 2000. Development of a methodology for non-contacting strain measurements in fluid environments using computer vision. Optics and Lasers in Engineering, 32:367-377.

Taboada, B., Larralde, P., Brito-Albavera T., Vega, L., Diaz, R., Galindo, E., Corkidi, G. 2003. Images acquisition of multiphase dispersion in fermentation processes. Journal of Applied Research and Technology, 1:78-84.

Tang, W., Reynolds, A.P. 2010. Production of wire via friction extrusion of aluminum alloy machining chips, Journal of Materials Processing Technology, 2231-2237.

Tang, H.W., Chen, C., Huang, J.T. 2008. An improved PTV system for large-scale physical river model, Journal of Hydrodynamics, 20(6):669-678.

Taylor, L., Szymczak W.G. 2007. Platform loading from explosion in saturated sand using a visco-plastic model. Fragblast Int. J. Blasting and Fragmentation 1: 51-68.

Thomas, W.M., Nicholas, E.D., Jones, S.B., 1993. US Patent # 5,262,123.

Tiwari, V, Sutton, M.A., McNeill, S.R., Xu, S.W., Deng, X.M. 2009. Application of 3D image correlation for full-field transient plate deformation measurements during blast loading. Int. J. Impact Eng. 36:862-74.

Tiwari, V, Williams, S, Sutton, M.A., McNeil, S.R. 2005 Application of digital image correlation in impact testing. SEM Annu. Conf. 2005:413.

Tiwari, V, Sutton, M.A., McNeil, S.R., Kwon, O.H., Fourney, W.L., Bretall, D. 2007. Studying on improvised explosive devices using digital image correlation. SEM Annu. Conf. 414-416.

Tiwari, V, Sutton, M.A., McNeill, S.R. 2007. Assessment of high speed imaging systems for 2D and 3D deformation measurements: methodology development and validation. Experimental Mechanics 47(4):561-579.

Tropea, C., Yarin, A., Foss, J. 2007. *Handbook of experimental fluid mechanics*. Berlin Heidelberg: Springer.

U.S. Army Aviation Systems Command 1989.

Verse, J. 1971. A review of the Severity Index. SAE Paper 710881. Proc. 15th Stapp Crash Conf.: 771-795.

Wang, A.J. and Hopkins H.G. 1954. Study on the plastic deformation of built-in circular plates under impulsive load. J. Mech. Phys. Solids 8: 22-87.

Wenzel, A., Hennessey, J. 1973. Analysis and measurements of the response of armor plates to land mine attacks. Army Symposium on Solid Mechanics, 114-128.

Xu, M., Chen F., Liu X., Ge W., Li J., Discrete particle simulation of gas–solid two-phase flows with multi-scale CPU–GPU hybrid computation, Chemical Engineering Journal 207-208: 746-757, 2012

Yankelevsky, D.Z., Feldgun V.R. and Karinski Y.S. 2008 Underground explosion of a cylindrical charge near a buried wall. Int. J. Impact Engineering 35: 905-919.

Yu, T.X., Chen F.L. 1992. The large deflection dynamics plastic response of rectangular plates. Int. J. Impact Eng 12(4):603-616.

Zaera, R., Arias A., Navarro C 2002. Analytical modeling of metallic circular plates subjected to impulsive loads. Int. J. Solids Structures 39: 659-672.

Zakrisson, B., Wikman B. and Häggblad H. 2011. Numerical simulations of blast loads and structure deformation from near-field explosions in Air. Int. J. Impact Engineering 38: 597-612.

Zhang, H., Zhao, X., Deng, X., Sutton, M.A., Reynolds, A.P., McNeil, S.R. Investigation of material flow during friction extrusion process. Journal of Mechanical Sciences.

Zhu, L. 1995. Transient deformation modes of square plates subjected to explosive kiadings. Int. J. Solids Structures 33(3):301-314.

# APPENDIX A – INPUT-SCALED DISPLACEMENT HISTORIES FOR BLAST LOADING EXPERIMENTS

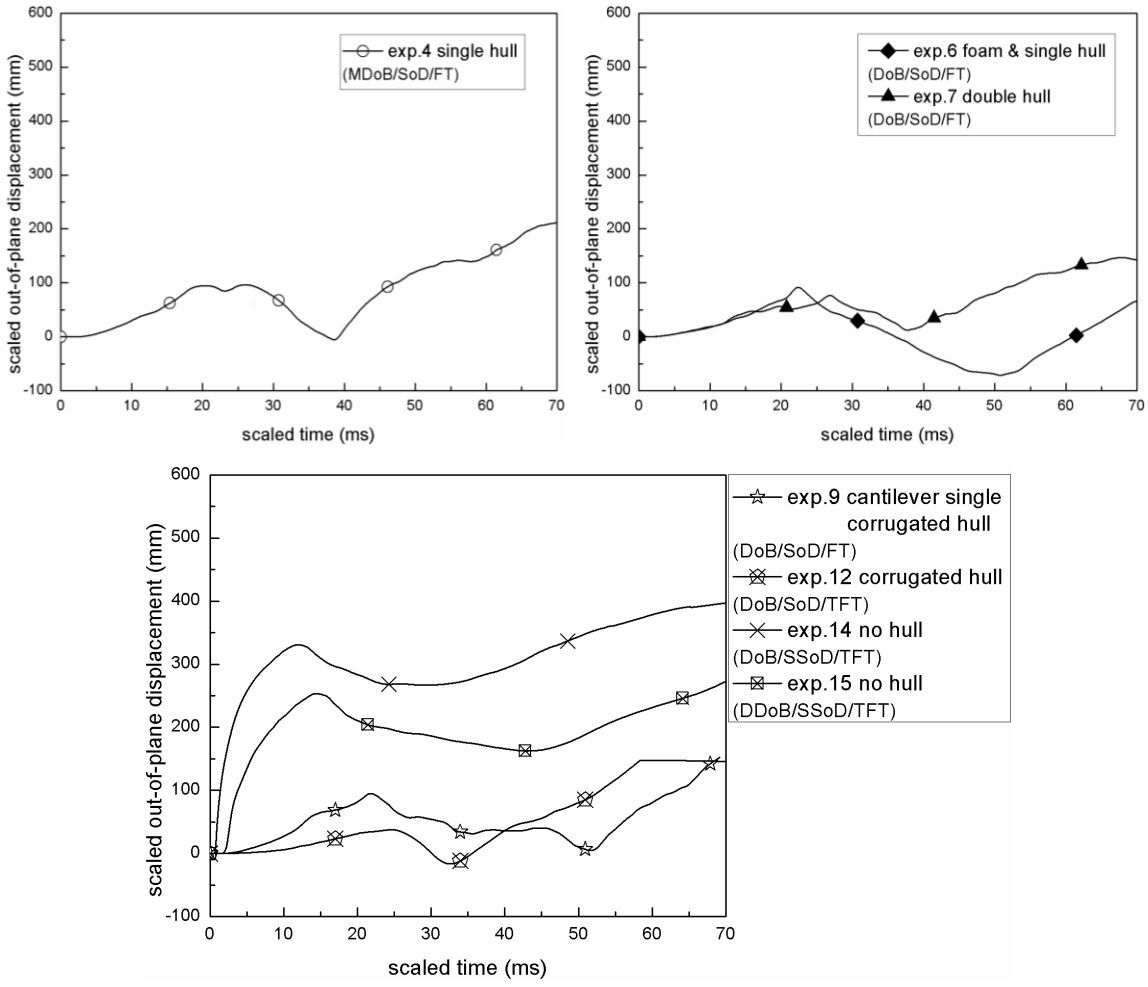


Figure A.1 Input-scaled displacement history for experiments 4, 6, 7, 9, 12 and 14-15 at approximate floorboard center location. (DoB-7.62mm, MDoB-12.7mm, DDoB-25.4mm, SoD-81mm, SSoD-31mm, FT-0.51mm floorboard, TFT-1.60mm floorboard).

# APPENDIX B – INPUT-SCALED OUT-OF-PLANE ACCELERATION HISTORIES FOR BLAST LOADING EXPERIMENTS #1-15

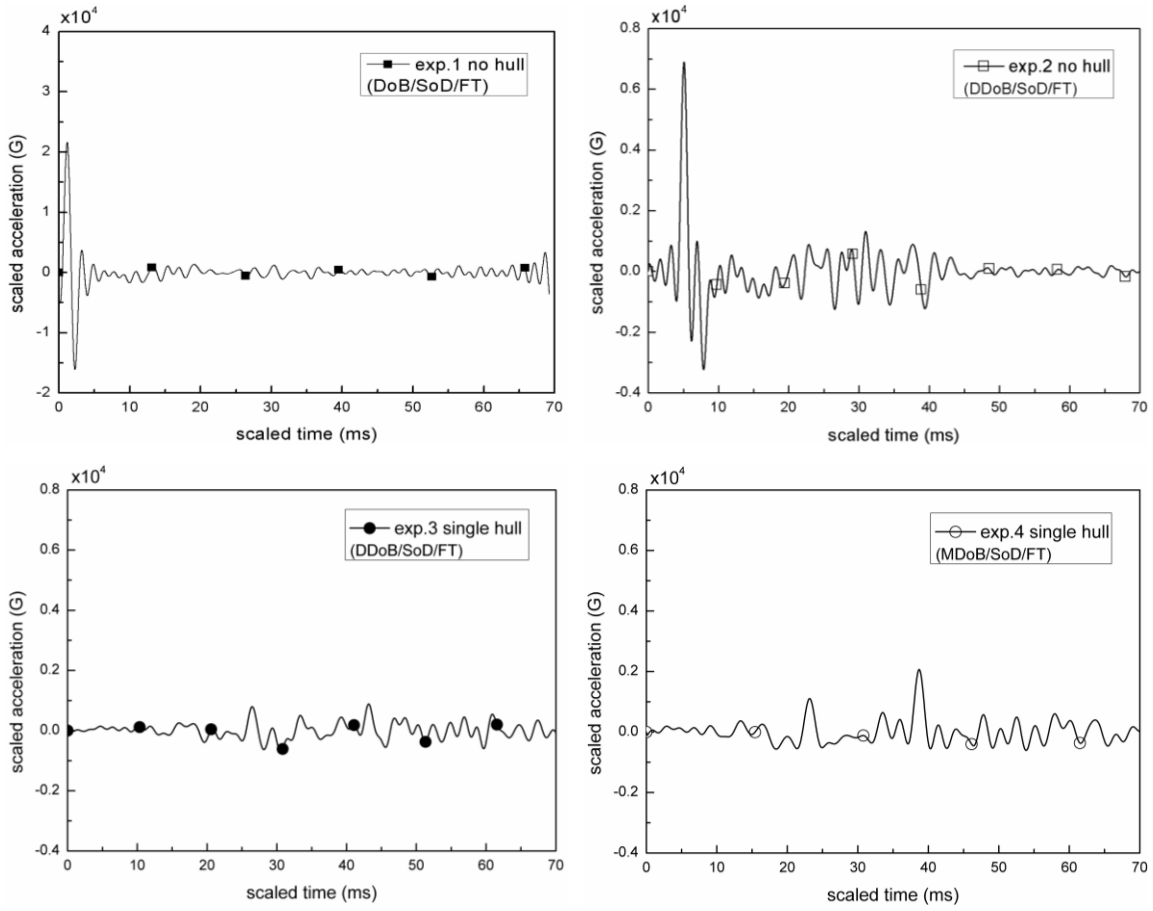


Figure B.1 Input-scaled out-of-plane acceleration histories of experiments 1-15 at approximate floorboard center location. (DoB-7.62mm, MDoB-12.7mm, DDoB-25.4mm, SoD-81mm, SSoD-31mm, FT-0.51mm floorboard, TFT-1.60mm floorboard). All units in G′s, where G is the acceleration of gravity (9.81m/s$^2$).

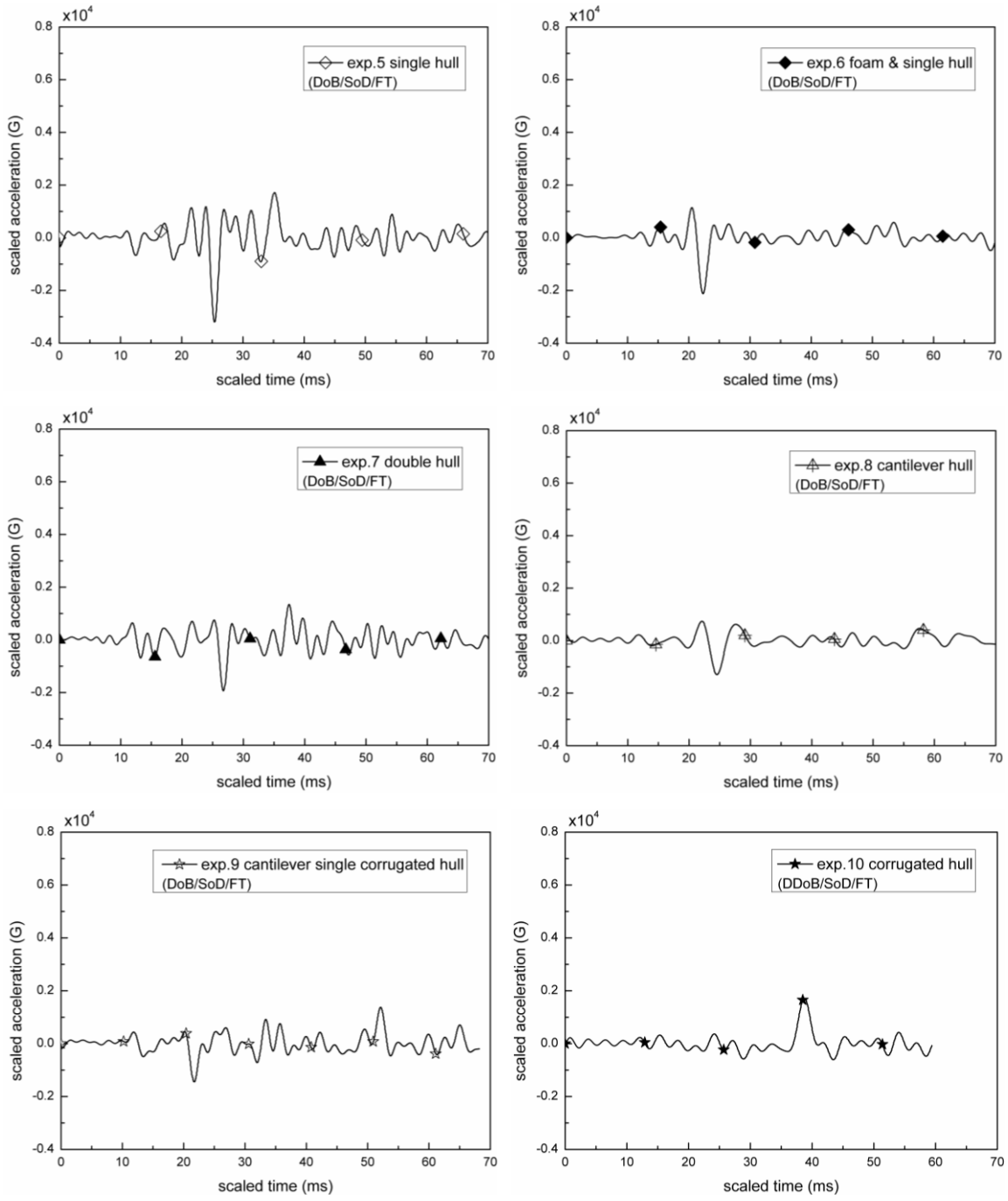


Figure B.1 Input-scaled out-of-plane acceleration histories of experiments 1-15 at approximate floorboard center location. (DoB-7.62mm, MDoB-12.7mm, DDoB-25.4mm, SoD-81mm, SSoD-31mm, FT-0.51mm floorboard, TFT-1.60mm floorboard). All units in G′s, where G is the acceleration of gravity (9.81m/s$^2$) (cont′d).

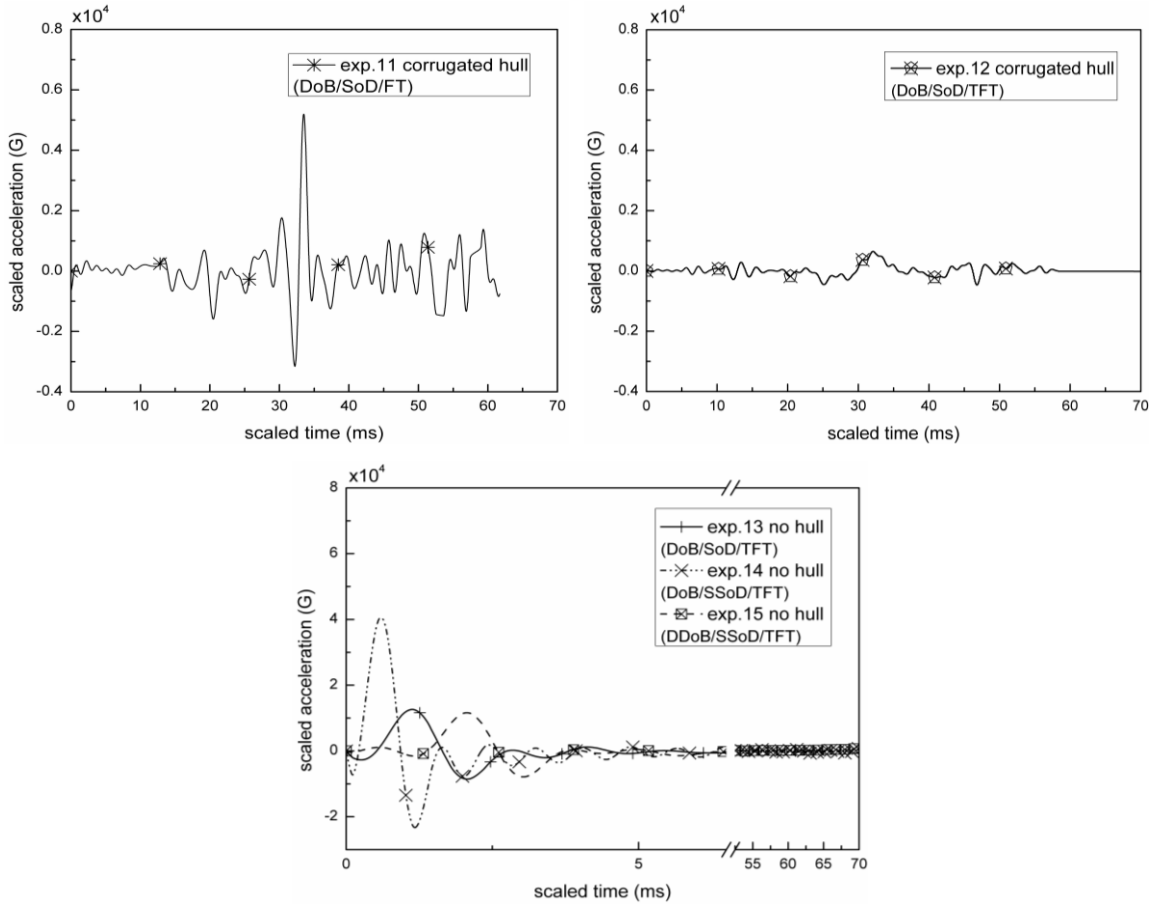


Figure B.1 Input-scaled out-of-plane acceleration histories of experiments 1-15 at approximate floorboard center location. (DoB-7.62mm, MDoB-12.7mm, DDoB-25.4mm, SoD-81mm, SSoD-31mm, FT-0.51mm floorboard, TFT-1.60mm floorboard). All units in G′s, where G is the acceleration of gravity (9.81m/s$^2$) (cont′d).

# APPENDIX C – SCALED HIC DATA FOR BLAST LOADING EXPERIMENTS

## PROCEDURE TO DETERMINE $HIC_{15}$

Consistent with Eq. (3-1), the input-scaled acceleration versus time experimental data that has been frequency filtered using procedures described in Section 3.5.1 is the primary data used for each location of interest.

Next, the experimental data is interpolated on discrete intervals by a quadratic polynomial function. Beginning at t=0s, the integrand in Eq. (3-1) is integrated for the appropriate time interval 0.000 →0.015s using Simpson's rule. The initial time is incremented by Δt, which is the time interval between data points, to obtain $HIC_{15}$. This process is repeated by integrating from Δt→ (Δt + .015s) to obtain $HIC_{15}(\Delta t)$. The process is repeated throughout the measured time history to obtain $HIC_{15}(t)$. The maximum $HIC_{15}$ is obtained from the resulting data.

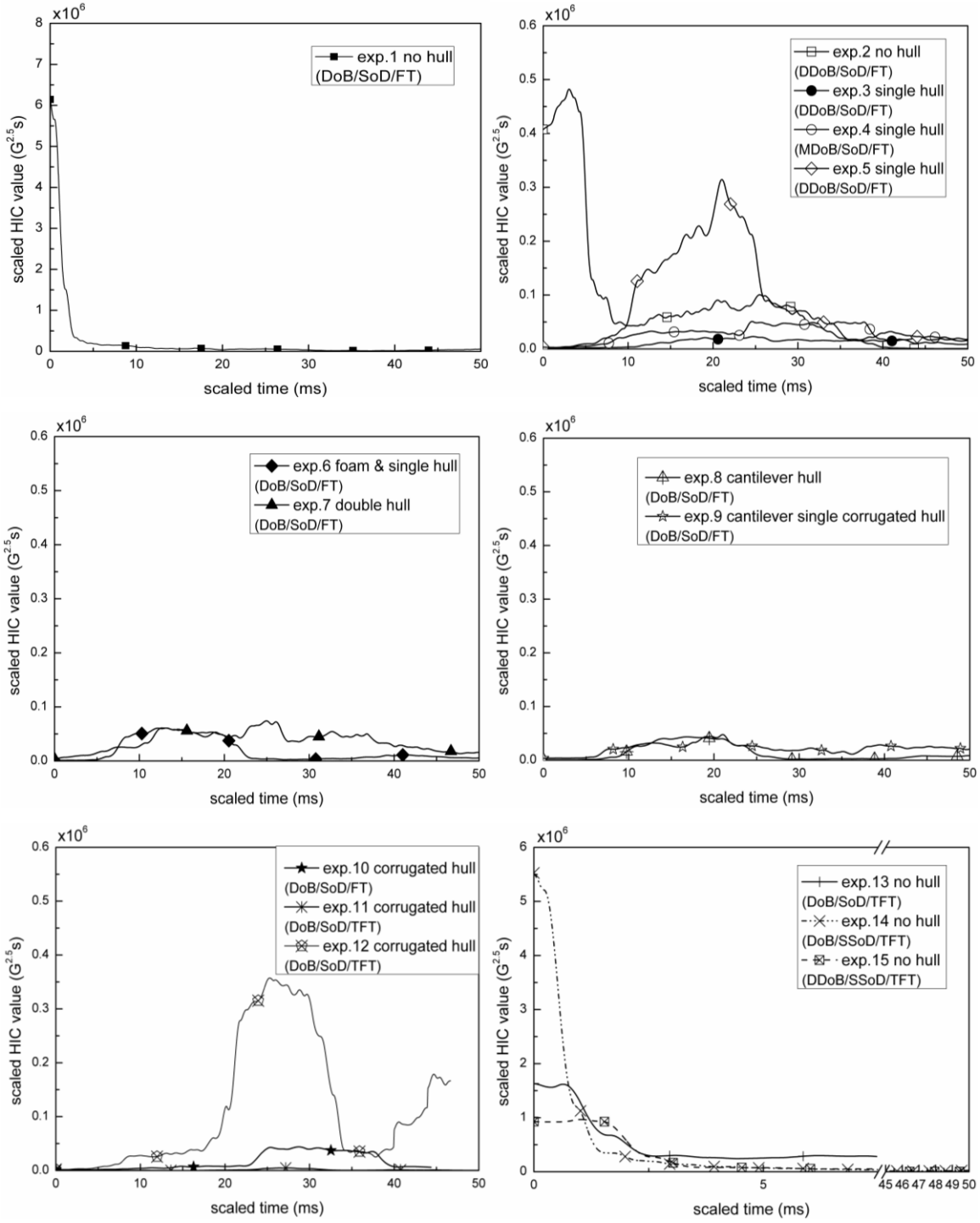


Figure C.1 Scaled $HIC_{15}(t)$ Data for Experiments 1-15. (DoB-7.62mm, MDoB-12.7mm, DDoB-25.4mm, SoD-81mm, SSoD-31mm, FT-0.51mm floorboard, TFT-1.60mm floorboard). G is the acceleration of gravity ($9.81 m/s^2$).

# APPENDIX D – INPUT-SCALED ACCELEROMETER DATA FOR BLAST LOADING EXPERIMENTS #18-26

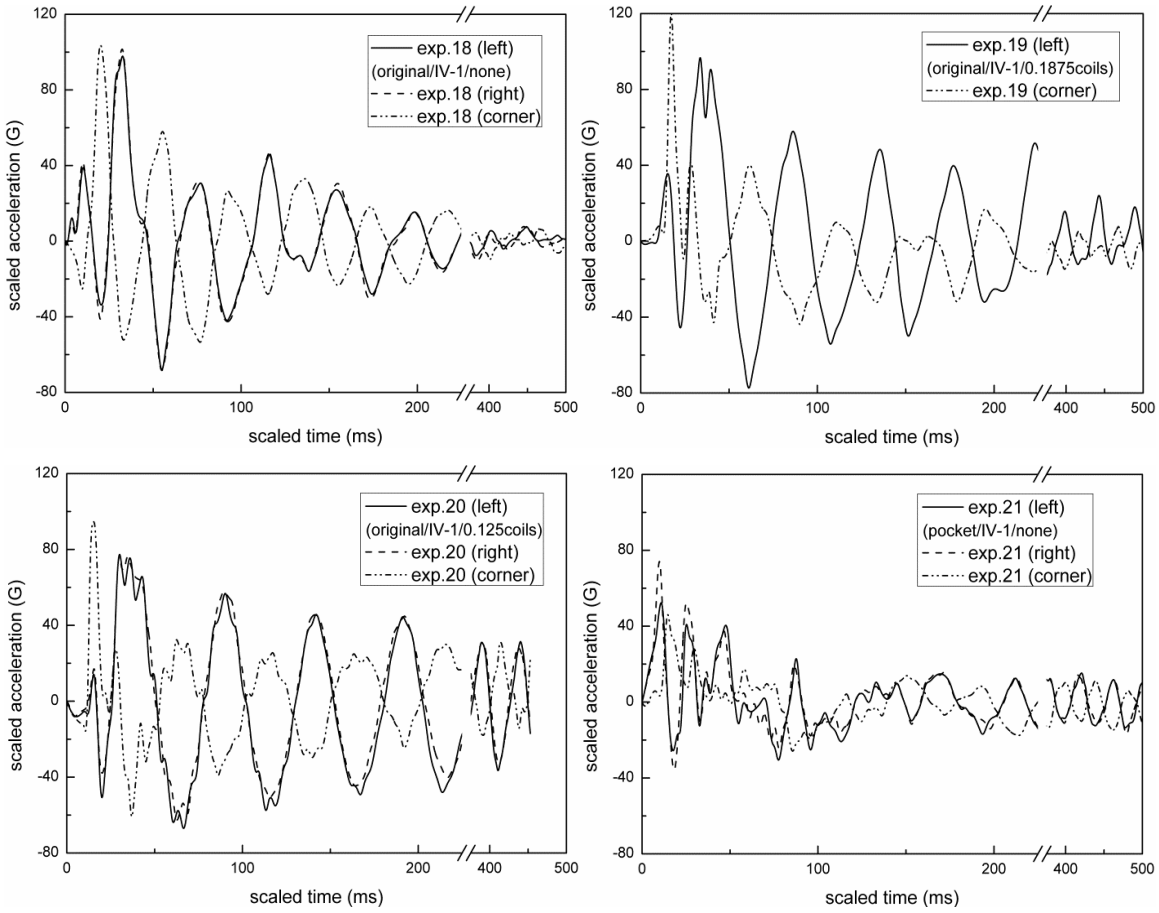


Figure D.1 Input-scaled accelerometer data for experiments 18-26 at center of left long edge span, center of right long edge span and corner of the frame. (exp. #18-26: DoB=9.91 mm, SoD to hull=25.40mm). G is the acceleration of gravity (9.81m/s$^2$).

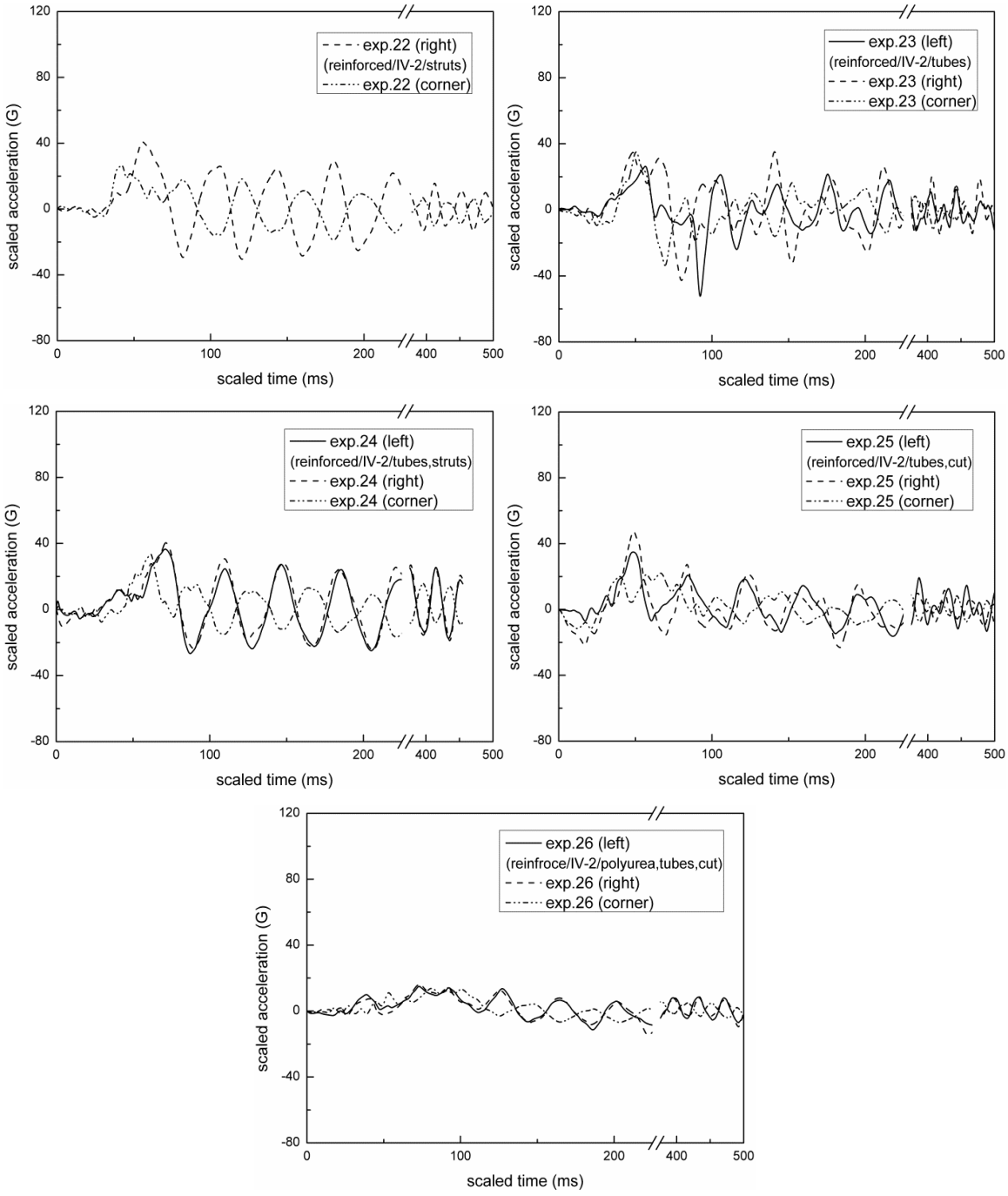


Figure D.1 Input-scaled accelerometer data for experiments 18-26 at center of left long edge span, center of right long edge span and corner of the frame. (exp. #18-26: DoB=9.91 mm, SoD to hull=25.40mm). G is the acceleration of gravity (9.81m/s$^2$) (cont′d).

# APPENDIX E – INPUT-SCALED HIC DATA FOR BLAST LOADING EXPERIMENTS #18-26

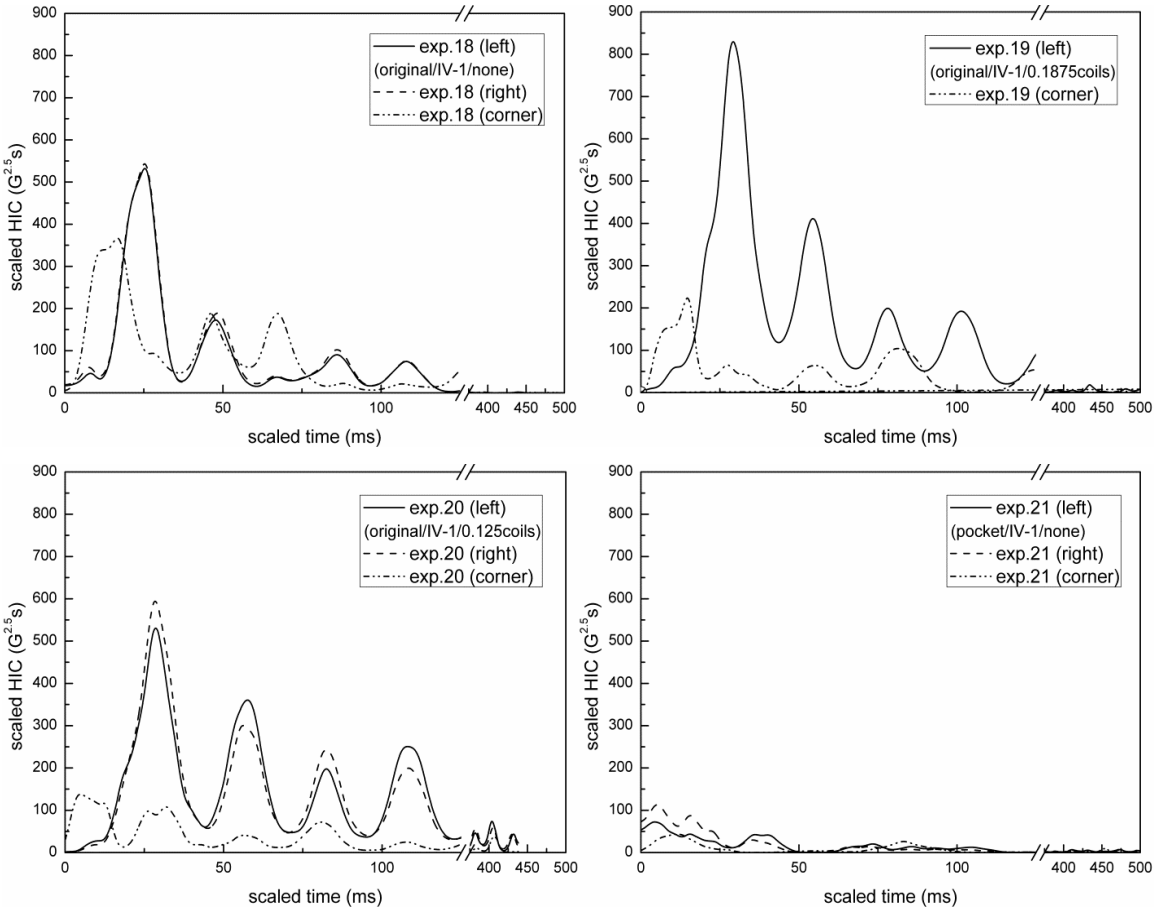


Figure E.1 Input-scaled HIC data of experiments 18-26 at center of left long edge span, center of right long edge span and corner of the frame. (exp. 18-26: DoB = 9.91mm, SoD to hull = 25.40mm). G is the acceleration of gravity (9.81m/s$^2$).

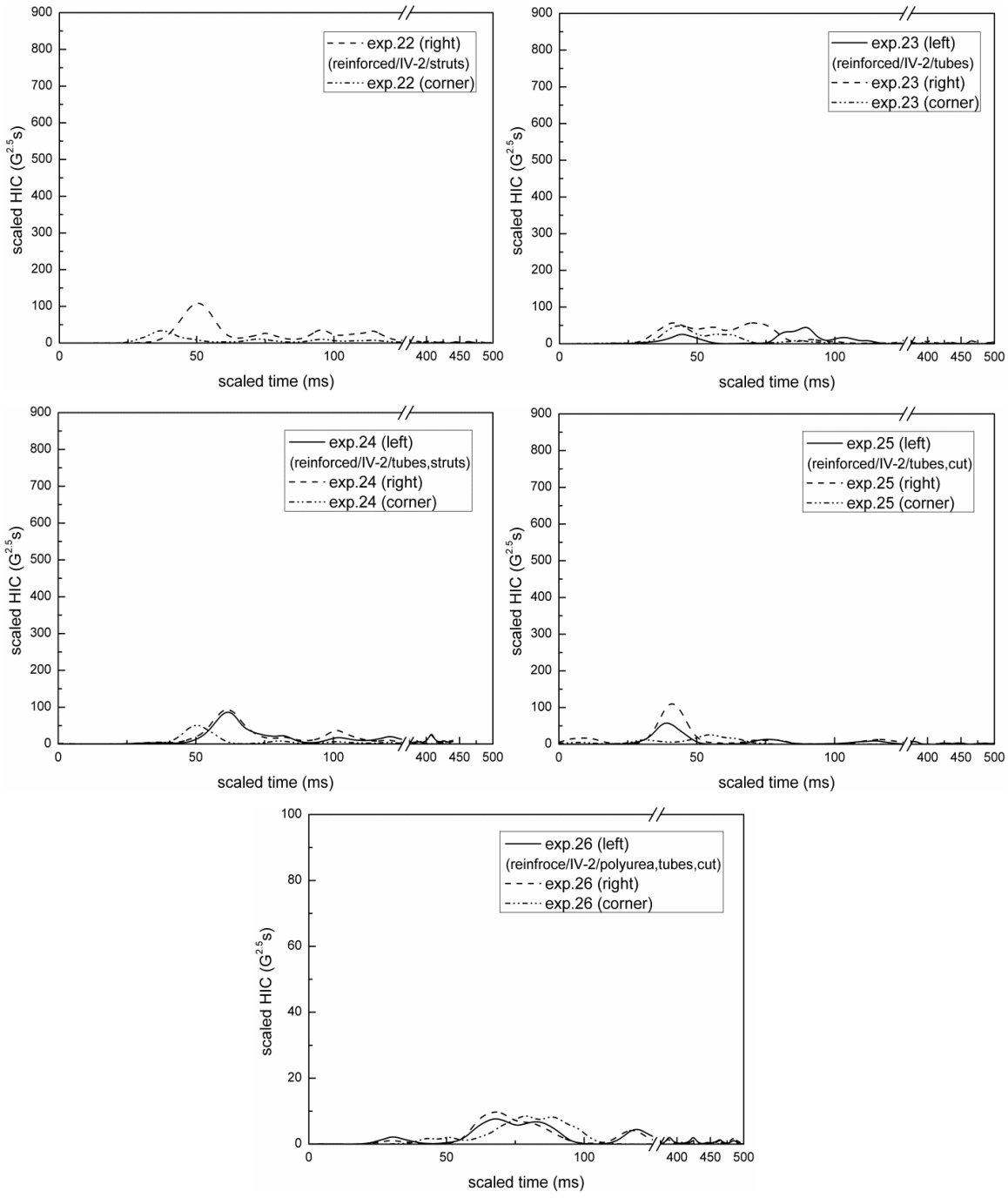


Figure E.1 Input-scaled HIC data of experiments 18-26 at center of left long edge span, center of right long edge span and corner of the frame. (exp. 18-26: DoB = 9.91mm, SoD to hull = 25.40mm). G is the acceleration of gravity (9.81m/s$^2$) (cont′d).